MECHANICAL PROPERTIES, THERMAL STABILITY AND RADIATION DAMAGE OF FERRITIC STEELS PROCESSED BY THERMAL MECHANICAL TREATMENTS

A Dissertation

by

MIAO SONG

Submitted to the Office of Graduate and Professional Studies of
Texas A&M University
in partial fulfillment of the requirements for the degree of

DOCTOR OF PHILOSOPHY

Chair of Committee,	Karl Ted Hartwig
Co-chair,	Xinghang Zhang
Committee Members,	Lin Shao
	Haiyan Wang
Head of Department,	Ibrahim Karaman

August 2014

Major Subject: Materials Science and Engineering

ABSTRACT

The dramatically increasing demand for energy stimulates scientists all over the world to consider the possible ways to meet future energy needs. The application of atomic energy has been demonstrated to be a reliable, economic, and environmental friendly choice by the reactors operating today for half century. Lessons have been learned during the operation of generation I-III reactors. To avoid an unanticipated failure, high performance structural materials still represent a crucial component for extending the operation life of current reactors and the design of generation IV nuclear reactors and future fusion reactors. Due to their superior radiation tolerance, ferrite steels are currently the primary candidate under examination for generation IV or future fusion reactors.

Whereas considerable data have been published on modification of the chemical composition of ferrite steels and evaluation of their overall performance, few attempts have been tried to process the existing ferrite steels by plastic deformation and evaluate the performance and properties improvements. The deformation technique introduced here is equal channel angular extrusion (ECAE). During ECAE, severe shear strain (on the order of several hundred percent) is introduced into a material by extrusion through a channel of constant cross section that contains an abrupt angle.

The work presented in this dissertation is an attempt to apply ECAE to reactor steels of interest-namely T91 and 12Cr ODS. T91 (modified 9Cr-1Mo steel) is widely used and a commercialized material. 12Cr ODS is an oxide dispersion strengthened

ferrite steel developed based on the reduce activation concept and targeted for cladding at elevated temperature. The pros and cons for such an approach were evaluated based on the influence of such a plastic deformation on mechanical performance, thermal stability and radiation damage or tolerance.

In general, ECAE processed materials show improved strength and radiation tolerance. However, thermostability and ductility are sacrificed. The latter is not a potential problem because during service at elevated temperatures, the ECAE processed materials can regain ductility within a short period. Attention should be paid to the degeneration of thermostability after ECAE deformation.

DEDICATION

To my family

ACKNOWLEDGEMENTS

I would like to express my sincere thanks and gratitude to both of my advisors Dr. Karl T. Hartwig and Dr. Xinghang Zhang for their guidance, enthusiasm, patience and support through the whole PH.D study. They recruited me four years ago and brought me into the field of material deformation processing and radiation, which enabled my efforts. Their profound knowledge, strict attitude and great personality benefited me a lot, and will have long lasting impact on my future. I would also like to thank other members in my defense committee, Dr. Haiyan Wang and Dr. Lin Shao for their precious suggestions to improve the quality of my work.

I express my gratitude to Mr. Robert Barber for technical assistance on ECAE processing, Drs. Zhiping Luo and Hansoo Kim for TEM training, Mrs. Xuemei Wang for assistance with heavy ion irradiation experiments, Dr. Jinsung Jang at the Korea Atomic Energy Institute (South Korea) for providing the ODS specimens, Yuedong Wu and Dr. Yong Yang at University of Florida for FIB experiments. Their technical support and collaboration are greatly appreciated. I thank Ms. Jan Gerston for helping me with every administration step toward graduation.

In addition, many thanks go to my colleagues and friends, Shreyas Balachandran, Zach S. Levin, David C. Foley, Dr. Daniel Bufford, Steven Rios, Byoungsoo Ham, Zhe Fan, Sichuang Xue, Jin Li, Jie Jan, Wenrui Zhang, Dr. Aiping Chen, Dr. Li Chen, Dr. Ji Chen, Dr. Tao He, Dr. Qing Su, Dr. Kaiyuan Yu, Dr. Yue Liu, Dr. Cheng Sun, Jianfeng Wen, Di Chen, Jing Wang, Liang Jiao, Longfei Zhang, Peng Li, Huaping Xiao, Huili

Gao, Youxing Chen, Dr. Xingliang He, Dr. Ruixian Zhu, Dr. Yan Zhou, and Dr. Youwei Jiang. Thanks for all the help and happy distraction provided during my graduate study.

I sincerely acknowledge the financial support of DOE-NEUP under contract no. DE-AC07-05ID14517-00088120. The TA position provided by Dr. Ibrahim Karaman during the last two semesters is also acknowledged.

I am greatly indebted to my parents and wife for their complete, continued, and undoubted support. I would not have made it to where I am today without their encouragement, help and understanding.

NOMENCLATURE

Acronyms

AA	As Annealed
AC	Air Cooling
AR	As Received
AISI	American Iron and Steel Institute
ASTM	American Society of Mechanical Engineers
ASME	American Society for Testing Materials
bcc or BCC	Body Centered Cubic
CG	Coarse Grain
CNB	Chromium-Nickel Balance
DBTT	Ductile to Brittle Transition Temperature
DD	Dislocation Dynamic
dpa	Displacement per Atom
ECAE	Equal Channel Angular Extrusion
ECAP	Equal Channel Angular Pressing
EDM	Electro Discharge Machining
ELS	Elongated Lamella Structure
EELS	Electron Energy Loss Spectroscopy
FIM	Field Ion Microscopy
fcc or FCC	Face Centered Cubic

FFTF	Fast Flux Test Facility
FIB	Focused Ion Beam
F/M	Ferritic/Martensitic
GB	Grain Boundary
GFR	Gas Fast Reactors
GNB	Geometry Necessary Boundary
HFIR	High Flux Isotope Reactor
HIP	Hot Isostatic Pressing
HT	Heat Treatment
IAC	Irradiation Accelerated Corrosion
IASCC	Irradiation Assisted Stress Corrosion Cracking
IDB	Incidental Dislocation Boundary
IF	Interstitial Free
INCO	International Nickel Company
MA	Mechanical Alloying
MSR	Molten Salt Reactor
Na-LMR	Liquid Metal Cooled Sodium Fast Reactor
NC	Nanocrystalline
VDZ	Void(s) Denuded Zone
ODS	Oxide Dispersion Strengthened
PAGB	Prior Austenite Grain Boundaries
Pb-LMR	Liquid Metal Cooled Lead Fast Reactor

RAFM	Reduced Activation Ferritic Martensitic
RIS	Radiation Induced Segregation
RT	Room Temperature
SAZ	Surface Affected Zone
SCC	Stress Corrosion Cracking
SCWR	Super Critical Water Reactors
SEM	Scanning Electron Microscopy
SFT	Stacking Fault Tetrahedra
SPD	Severe Plastic Deformation
SS	Stainless Steel
SRIM	Stopping Range of Ions in Matter
STEM	Scanning Transmission Electron Microscopy
T91	modified 9Cr-1Mo steel
TB	Two Beam Condition
TEM	Transmission Electron Microscopy
TMT	Thermo-mechanical Treatment
TTT	Time Temperature Transformation
UFG	Ultrafine Grain
UTS	Ultimate Tensile Strength
UHP	Ultrahigh purity
WBDF	Weak Beam Dark Field
WQ	Water Quenching

XRD	X-ray Diffraction
Symbols	
Ms	Martensite Start Temperature
α_P	Polygonal Ferrite
α_A	Allotriomorphic Ferrite or Grain Boundary Ferrite
α'_M	Martensite
α'_T	Tempered Martensite
α'_{AT}	Auto-tempered Martensite
α_B	Bainitic Ferrite
M/A	Martensite/Austenite Constituent
γ	Retained Austenite
ε-C	Epsilon Carbide
θ	Cementite
σy/ $\sigma_{0.2}$	Yield Strength
σ_{UTS}	Ultimate Tensile Strength
G	Shear Modulus or dose rate
b	Burgers Vector
f	Volume Fraction
τ	Shear Stress for Dislocation Bypass of An Obstacle
L	Interparticle Distance on the Slip Plane
M	Taylor Factor
$\rho_0$or $\rho_{dis.}$	Initial Dislocation Density

θ_{dis}	GB Misorientation Angle
σ_0	Lattice Friction Strength
β	Dislocation Detachment Parameter
k	Grain Boundary Strength
ν	Poisson's Ratio
S_{ii}	Compliance Factors
H	Hardness
k^2	Sink Strength
Zd	Defects Capture Site
l	Thickness
k	Boltzmann's Cosntant

TABLE OF CONTENTS

Page

LIST OF FIGURES

Page

LIST OF TABLES

Page

CHAPTER I

INTRODUCTION AND LITRATURE REVIEW

This chapter provides background to understand the research work of this thesis, including the development of ferritic/martensitic steels and oxide dispersion strengthening (ODS) steels, equal channel angular extrusion (ECAE), and radiation damage in structural materials. The strategy for design of radiation tolerant material is also addressed.

1.1 Ferritic/martensitic steels

Chromium bearing Ferritic-Martensitic (F/M) steels, which were originally designed for conventional fossil power plants, were examined for high temperature structural application in the core of faster reactors in developed countries in the 1970s [1]. These F/M steels, especially containing 9-12 wt.% Cr, exhibit excellent mechanical properties, thermal properties, irradiation tolerance, corrosion, and oxidation resistance [2]. These superior properties make the high Cr F/M steels excellent candidates for Gen IV reactors with several concepts proposed including gas fast reactors (GFR), water cooled super critical water reactors (SCWR), molten salt reactors (MSR), liquid metal cooled sodium fast reactors (Na-LMR) and lead fast reactors (Pb-LMR) [1, 3]. In the following section, the design criteria, and different generations of these F/M steels will be briefly discussed, and the typical microstructure of an important F/M steel, T91 and one of the focus in this thesis, will be addressed.

1.1.1 Design criteria of 9-12wt.% Cr ferritic-martensitic (F/M) steels

To understand the design criteria of F/M steels, it is necessary to introduce the stabilizer concept. In general, the iron binary phase diagrams can be separated into four major categories: open and close γ-field, and expanded or contracted γ-field. Thus, alloying elements can influence the iron binary phase diagram in two ways, either encouraging the formation of γ-phase or encouraging the formation of α-phase. Elements expanding the γ-field and promoting the formation of the γ-phase over wider compositional ranges, are defined as γ-stabilizers (austenite stabilizers). In contrast, elements contracting the γ-field and promoting the formation of the α-phase over wider compositional limits, are defined as α-stabilizers (ferrite stabilizers). The typical phase diagrams are shown in Fig.1.1. The typical α-and γ-stabilizing elements are listed in Table 1.1. The most important γ-stabilizers include C, N, Ni, Mn. Commonly used α-stabilizers include Cr, Al, Mo, V and the carbide forming elements Ta and Nb. Usually, α-stabilizers can cancel the effect of adding γ-stabilizers under appropriate conditions. However, abnormal behavior can occur in any particular situation. For example, adding Cr, a typical α-stabilizer, to nickel at around 18wt% can help to stabilize the γ-phase in 18Cr-8Ni wt% austenitic steels. Less Cr will promote the formation of martensite in this case and reduce the stability of the γ-phase.

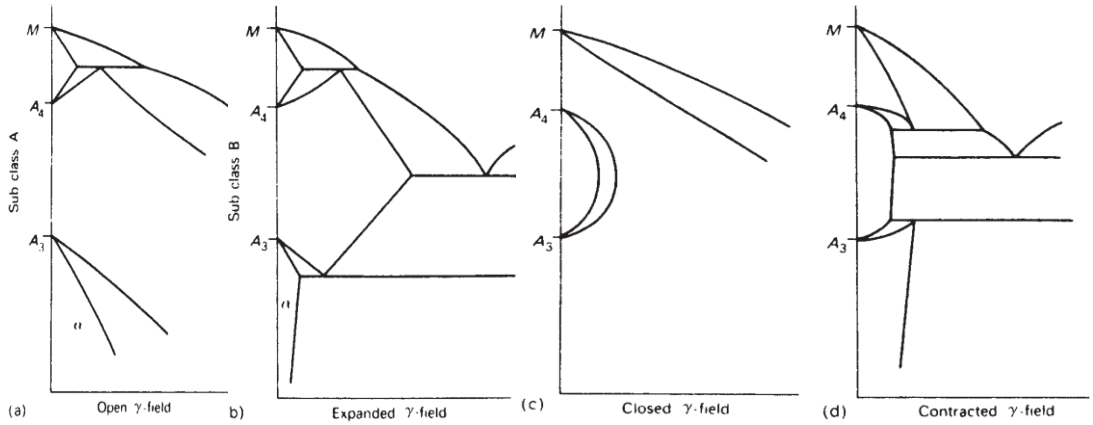

Figure 1.1 Iron binary phase diagrams: (a) open γ-field; (b) expanded γ-field; (c) closed γ-field; (d) contracted γ-field [4].

Table 1.1 Typical α and γ stabilizers for iron binary systems[4].

Stabilizers		Alloying elements adding in to Fe
γ stabilizers	Open γ-field	Ni, Mn, Co, Ru, Rh, Pd, Os, Ir, Pt
	Expanding γ-field	C, N, Cu, Zn, Au
α stabilizers	Close γ-field	Si, Al, Be, P, Ti, V, Mo, Cr
	Contracted γ-field	B, Ta, Nb, Zr

The family of F/M steels shares a common design criterion: the austenite (γ-phase) and ferrite (α-phase) stabilizers are balanced according to a Chromium-Nickel balance (CNB) empirical formula. The balancing of γ and α stabilizers is actually an approximation method for the multiple element phase diagram, which simplifies the problem into a binary phase diagram (the Fe-Cr phase diagram in current case).The effects of other elements are considered as a kind of perturbation to the boundaries of the binary phase diagram. Thus, the F/M steels are desired to be fully austenite during

austenitization, and transformed completely to martensitic during the sequent air cooling or watering quenching after austenizing [1]. The equation is written as following [5]:

$$CNB = Cr + 6Si + 4Mo + 1.5W + 11V + 5Nb + 9Ti + 12Al \\ -40C - 30N - 4Ni - 2Mn - Cu \quad \text{Eq.1.1}$$

where the elements amount in weight percent. If CNB is smaller than 10, delta ferrite will not form. Delta ferrite is to be avoided in the design F/M steels. For CNB greater than 12, large quantities of delta ferrite will be inevitable. For a CNB value in between 10-12, the amount of delta ferrite is hard to predict. The chemical composition and the CNB factors for various commercialized steels are listed in Table 1.2. The CNB factors for some commercialized F/M steels are located at 10-12, where experiments are needed to evaluate the formation of delta ferrite. Carefully controlled heat treatments are needed to avoid delta ferrite in these steels.

Table 1.2 The nominal chemical composition of commercial and experimental F/M or RAF steels [1, 6, 7] with CNB values.

Steels	C	Si	Mn	Cr	Mo	W	V	Nb	B	N	Ni	Ti	Co	Cu	Ta	Nd	CNB
A533 Grade B	0.25	0.2	1.3		0.5												
2.25Cr-1Mo(T22)	0.15	0.3	0.45	2.25	1												
2.25Cr-1.6WVNb(T23)	0.06	0.2	0.45	2.25	0.1	1.6	0.25	0.05	0.003								5.95
2.25Cr-1MoVTi(T24)	0.08	0.3	0.5	2.25	1		0.25		0.004	0.03		0.07					6.33
ORNL 3Cr-3WV	0.1	0.14	0.5	3		3	0.25										6.09
ORNL 3Cr-3WVTa	0.1	0.14	0.5	3		3	0.25								0.1		6.09
9Cr-1Mo(T9)	0.12	0.6	0.45	9	1												10.9
Mod 9Cr-1Mo(T91)	0.1	0.4	0.4	9	1		0.2	0.08		0.05							11.7
E911	0.11	0.4	0.4	9	1	1	0.2	0.08		0.07							12.2
NF616(T92)	0.07	0.06	0.45	9	0.5	1.8	0.2	0.05	0.004	0.06							11.01
12Cr-1MoV	0.2	0.3	0.5	12	1		0.25				0.7						8.75
12Cr-1MoV(HT91)	0.2	0.4	0.6	12	1		0.25				0.5						9.95
12Cr-1MoWV(HT9)	0.2	0.4	0.6	12	1	0.5	0.25				0.5						10.7
HCM12	0.1	0.3	0.55	12	1	1	0.25	0.05		0.03							16.3
TB12	0.1	0.06	0.5	12	0.5	1.8	0.2	0.05	0.004	0.06	0.1						12.31
TB12M	0.13	0.25	0.5	11	0.5	1.8	0.2	0.06		0.06	1						7.7
HCM12A(T122)	0.11	0.1	0.6	12	0.4	2	0.25	0.05	0.003	0.06	0.3			1			10.6
NF12	0.08	0.2	0.5	11	0.2	2.6	0.2	0.07	0.004	0.05			2.5				13.75
SAVE12	0.1	0.3	0.2	11		3	0.2	0.07		0.04			3		0.07	0.04	14.25
F82H	0.1	0.2	0.5	8		2	0.2		0.003						0.04		9.4
EUROFER	0.11	0.05	0.5	8.5		1	0.25		0.005						0.08		7.65
ORNL 9Cr-2WVTa	0.1	0.3	0.4	9		2	0.25			0.025					0.07		11
F17	0.06	0.35	0.4	17.3							0.09						15.84
EM12	0.09	0.37	0.9	9.6	1.91		0.28	0.41			0.12						18.71
FV448	0.11	0.28	1	9.7	0.69	0.17	0.18	0.28			0.69						8.615
1.4914	0.17	0.31	0.7	10.5	0.56		0.25	0.2			0.87						6.67
EM10	0.11	0.37	0.5	8.8	1.05						0.18						9.1
LA12Ta	0.16	0.03	0.8	9.8		3	0.25			0.045					0.1		7.88
CETA	0.18	0.07	1.4	9.6		0.8	0.6		0.008	0.015					0.5		7.37
Mod.9Cr-1W	0.1			9		1	0.2		0.005	0.003					0.1		8.61
Mod.9Cr-3W	0.15			9		3	0.2		0.007	0.003					0.1		9.61
JLF-4	0.1	0.5	0.05	2.25		2	0.2			0.005					0.07		6.2
L5	0.1	0.3	0.5	9		1				0.002							7.24
L7	0.1	0.3	0.5	9		1				0.002							7.24
GA3X	0.17			7.7		2	0.02										4.12

1.1.2 The evolution of F/M steels

Different generations of F/M steels are characterized by the creep strength at 600°C up to 10^5 h, which is an important property for practical applications. The creep strength of the zero generation F/M steel is below 40MPa, and the maximum application temperature is below 540°C. The creep strengths of Gen I, II, III, IV F/M steels are 60,100,140,180MPa at 600°C for 10^5 h and the upper bound applicable temperatures are 565, 592, 620 and 650°C, respectively.

Modification is a common method to enhance the performance of earlier generation materials. For example, T9 steel is the zero generation of heat resistance steels with the nominal composition of Fe-9Cr-1Mo-0.45Mn-0.6Si-0.12C. A special amount of carbide is used to balance the Cr in order to suppress the formation of δ-ferrite. The high weight percent of Cr is used to increase the corrosion resistance of the steel. The alloying elements also have other functions, e.g. Si to achieve deoxidation and retard the formation of cementite; Mn to combine with the impurity of sulfur; Mo to enhance hardenability [4]. T91 steel, a commercialized F/M steel, is modified from T9 (9Cr-1Mo) steel by addition of V, Nb and N to form carbides or nitrides to enhance the creep strength at elevated temperature [8]. As a representative Gen II structural material, T91 has already been widely used [3]. Some derivatives of T91, such as NF616 (grade 92) and E911, are considered candidates for new generation nuclear reactors or fossil power generators due to their enhanced creep resistance. By adding W and Co into earlier generations of the F/M steels, the SAVE12 or NF12 alloys (Gen IV) exhibit a 10^5 h creep rupture strength of ~180MPa at 600ºC, nearly twice of that of the T91 alloy, due

to solid solution hardening [1]. Details of heat resistant steels are given in Table.1.2, including 0-IV generation steels, most of which are F/M or ferritic steels.

Since the early 1980s, the concepts of low activation and reduced activation have been widely accepted for future fusion reactors, with regard to the safety and environmental concerns [9]. The materials satisfying this design concept need to exhibit fast induced radioactivity decay, which, allows the shallow land burial or even recycling after an acceptable period of storage [1, 10]. High purity Si-C is found to be the only true low activation material. For steels, true low activation is impossible because of the occurrence of transmutation reactions of iron atoms. Thus, the reduced activation design of the steels are realized by using elements of higher decay rate of W, Ta, Cr, V instead of slow-decaying elements including Nb, Mo and Ni [11, 12]. This design criteria rules out the possibility of using γ based stainless steels which need substantial amounts of Ni as a balance to the Cr to keep the fcc structure. Also, there are some other reasons which will be discussed later. On the other hand, Mo and Nb limit most of the F/M steels such as T9, T91, T92, T122, HT9, HT91 et al for the fusion application. The F/M martensitic steels are named reduced activation ferritic martensitic (RAFM) steels if they meet the design criteria. The typical alloys are EUROFER and F82H designed by Europe and the IEA respectively [13-16]. Most of the ODS steels are also designed in this way, in which the elements Mo, Ni and Nb elements rarely appear [17]. Table 1.2 also gives the chemical composition of several RAF/M steels.

1.1.3 T91 (Modified 9Cr-1Mo) steel and basic microstructure

T91 (modified 9Cr-1Mo steel) was designed as a structural material for steam generators in nuclear reactors in the 1970s [5]. The ASTM/ASME standard specified T91 according to the manufactured forms: **T**91 (Seamless **T**ube); **P**91 (Seamless **P**ipe); **FP**91 (**F**orged **P**ipe); **F**91 (**F**orging); **C**12A (**C**asting). It is also called Grade 91 steel. The name for modified 9Cr-1Mo in Europe is X10CrMoVNb9-1[18]. As tubing or piping is the most common application, thus the name T91 is popular and was selected for the nomenclature used in this thesis work.

Table 1.3 Long term creep strength for T91 steel assessed by ECCC[18].

Temperature (°C)	Values of new assessment (MPa)			Values according to EN10216-2(MPa)		
	10^4h	10^5h	2×10^5h	10^4h	10^5h	2×10^5h
500	289	255	245[a]	289	258	246[a]
550	200	164	153	199	166	154[a]
600	122	90	81	123	94	86[a]
650	68	48	43[a]	70	49	42[a]

[a] Extended time extrapolation

Excellent mechanical, physical and chemical properties combined with a low production cost for T91 steel make it attractive for applications in pressure vessels and piping systems in the fossil power and petrochemical industries [5, 19]. The latest creep data from the European Creep Collaborative Committee (ECCC) is shown in Table.1.3. T91 and similar alloys have also been considered as candidates for the fusion reactor first wall and coolant loop pipes in advanced reactors [20-23]. Various studies on T91

alloys have focused on radiation induced swelling and creep [21], post radiation mechanical properties [20, 24], corrosion resistance in supercritical water or liquid metal cooled reactor [22, 23], and the microstructure response to various types of radiation [25, 26]. T91 steels exhibit low thermal expansion, high thermal conductivity, excellent swelling resistance, and corrosion resistance to liquid metal coolants [2, 21, 23].

T91 steel is often used after a two-step heat treatment, which includes normalizing and tempering. The as-received T91 steel is typically heat-treated by a standard normalization (1038°C for 0.5 hour with air cooling) and tempering process (760°C for 0.5 hour and air cooling) [27]. The normalization or austenitization temperature 1038°C is selected because at this temperature all of the alloying carbides are supposed to dissolve and no significant coarsening of austenite grains should occur. The typical microstructure (revealed by optical microscopy) after the two step heat treatment is shown in Fig.1.2. It shows a tempered martensitic structure frequently observed in various F/M steels after tempering.

Due to the CNB value of around 11.7, δ-ferrite appears after water quenching and normalization above 1230°C for as short as 0.5 h [28, 29]. The morphology of the δ-ferrite is irregular shape and commonly precipitated at the prior austenite grain boundaries. Few precipitates are observed within δ-ferrite. Additional normalization at 1050°C for 0.5 h can remove all the residual δ-ferrite after the two-step heat treatment[30]. Preexisting δ-ferrite can lower the creep strength of T91 steels.

Water quenchedT91after normalization at 1045°C for 1 h is generally free from precipitates [31, 32]. Fe-rich $(Fe, Cr)_3C$ are observed after air cooling at the same temperature. The sequence of carbides precipitation is proposed as following [32]:

$$MATRIX \rightarrow (Fe,Cr)_3C \rightarrow Cr_7C_3 \rightarrow Cr_{23}C_6 \qquad \text{Eq.1.2}$$

The high temperature and long duration of tempering favor the formation of the $Cr_{23}C_6$ phase. Detailed microstructural studies reveal a more complicated process of carbide precipitation. For example, at the early stage of tempering T91 at 760°C, $(Cr, Fe)_2C$, VC and $(Cr, Fe, Mo)_{23}C_6$ coexist; after 0.5 hour, $(Cr,Fe)_2C$ disappears; Coarsening of VC and $(Cr, Fe, Mo)_{23}C_6$ occur after 1h tempering. The carbide precipitates at different types of boundaries were also investigated [33]. After the standard heat treatment, MC and $M_{23}C_6$ type carbides are favorable for precipitation at the prior austenite grain boundaries (PAGB), while M_2C precipitates preferentially form at the martensitic lath boundaries, where M is a mixture of alloying elements Cr, V and Mo. The Z-phase Cr(V,Nb)N and laves phase $(Fe,Cr)_2Mo$ are reported to form during long term creep testing for ~13000 h [34].

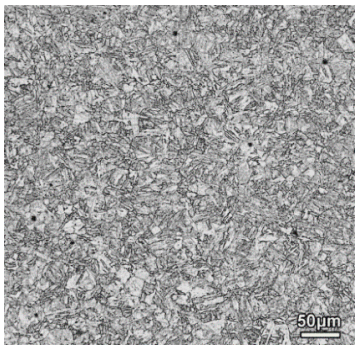

Figure 1.2 Typical optical micrograph of T91 steel after normalizing and tempering. The sample was etched using a 5g $FeCl_3$, 20ml HCl and 100 ml water solution.

1.2 ODS (oxide dispersion strengthening) steel

Reduced activation ferritic-martensitic (RAFM) steels exhibit satisfactory properties such as low thermal expansion coefficient, high thermal conductivity, and excellent swelling resistance [13-16]. However, the upper bound operation temperature of these materials is limited to ~ 550 °C because of degradation of their mechanical properties at higher temperatures [35-37]. RAFM oxide dispersion-strengthened (ODS) steels have thus been developed as structural materials for applications at 650°C or higher temperatures[38, 39]. The principal of ODS steels is that by introducing nano-scaled oxide particles (typically yttrium or yttrium-titanium complicated oxides), the high temperature mechanical properties can be significantly improved compared to those of their non-ODS counterparts. This is because the oxide particles can pin the mobile dislocations as well as the grain boundaries at elevated temperatures. Thus, the ODS steels exhibit a remarkable high temperature performance and are extremely reluctant to recrystallization. The particle-matrix interfaces can also serve as sinks for irradiation induced defects and facilitate the recombination of vacancies and interstitials, enhancing the radiation tolerance [40].The following section will discuss the development of ODS steels and the characterization of oxide particles, which is a primary interest of these steels.

1.2.1 Development of ODS steels

Early development of ODS alloys began in the 1960s. A number of pure metals as well as engineering alloys were attempted to be strengthened by oxides particles [41].

ODS steel appeared in 1970 made by Wilde et al [42]. The strengthening effect was affected by the distribution and initial size of TiO_2. However, these materials were quickly abandoned in the 1970s as a possible fuel cladding material for fast reactor, because the powder metallurgy method involved can make the products exhibit anisotropic mechanical properties. The strength is commonly higher in the rolling or extruded direction than that in the perpendicular direction. International Nickel patented a technique for producing several ODS products including MA956 and MA957 in 1978[43]. Commercial ODS steel then became available. During late 1980s, ODS steels were reconsidered for cladding applications by Japanese Atomic Energy Agency [9]. From then on, Japanese material scientists were active in this field [35, 44-47], and made several important contributions. Several easily oxidized metallic powders including Ti, Al, Nb were bended to increase the performance of ODS steels [35, 48]. The Ti with addition of excess oxygen can give the best combination mechanical properties, and later became the most popular formula. With special emphasis on the working-recrystallization process, the Japanese were also able to produce plate and tubing with better isotropic performance.

The manufacture of ODS steel is a complicated process and each step needs to be well controlled. Only a few countries including Japan, Europe and United States can make high quality ODS steel. The fabrication of ODS steel is a typical powder metallurgy process as shown in Fig.1.3. The steps start with atomizing of master alloy. Direct blending metallic powders with oxide particles can also be applied to produce the ODS alloys. However, ODS steels made through this route commonly show a less

homogenous microstructure and a relatively poor distribution oxide particles. The final heat treatment is different depending on the Cr% content. For 9wt.% Cr alloy, a normalization and tempering process is applied. For 12 wt.% Cr alloy, a recrystallization is performed before use[35].

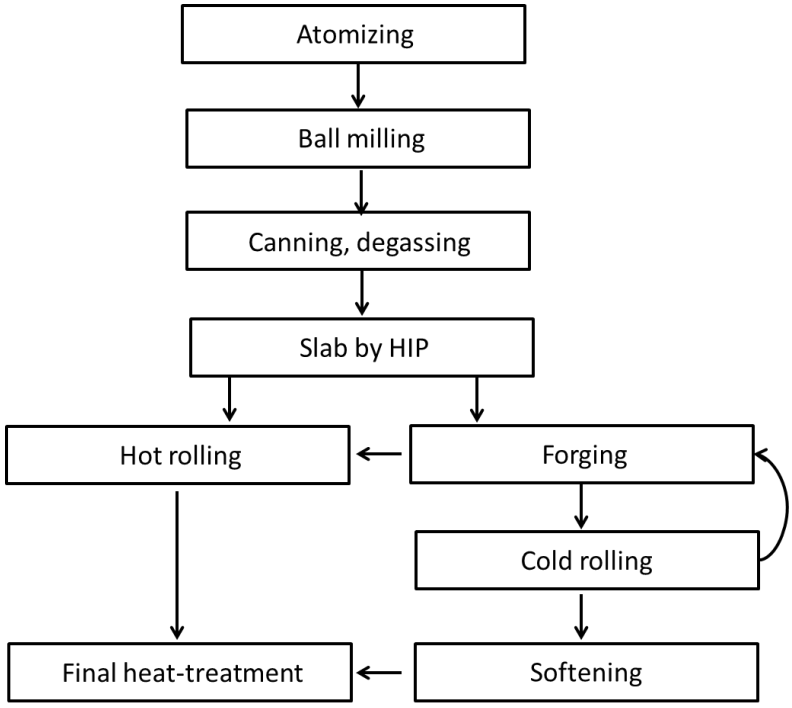

Figure 1.3 Typical process for producing ODS steels [35]

1.2.2 The microstructure and chemistry of oxide nanoparticles

The configuration of oxide particles including their chemical composition, size, morphology, spatial density and distribution is extremely important for revealing the underlying mechanism of mechanical strength and irradiation performance. Chemical

composition, crystalline structure and size of the ODS particles are changed with different alloying elements including Ti, Al, V, Zr and Nb [35, 48]. A small amount of Ti can significantly reduce the size of oxide particles to 3nm or below, because the yttrium and oxygen atom decomposed from Y_2O_3 during MA can bond with Ti and thus Y-Ti-O nanoparticles can precipitate during subsequent cooling [48]. This Y-Ti-O precipitation distribution with ultrahigh density ($10^{24}m^{-3}$) exhibits superior thermal stability, as confirmed by atom probe tomography (APT) studies [49, 50]. The Y-Ti-O enriched particles are also recognized as nanofeatures (NFs) or nanoclusters (NC), which are responsible for the excellent properties as high tensile, creep and fatigue strength [40]. The crystalline structure of the Y-Ti-O particles varies with particle size and the Y/Ti ratio. The larger Y-Ti-O particles with a Y/Ti ratio ≥1 take the formula of $Y_2Ti_2O_7$ or Y_2TiO_5, while smaller particles with a Y/Ti ratio around 0.1-0.6 are reported recently to have a defective NaCl structure [51]. For the ODS alloys without Ti, single phase of $Y_2O_3$is presented as confirmed by transmission electron microscope (TEM) [52]. However, detailed studies by field ion microscopy (FIM) or electron energy loss spectrum (EELS) revealed that the particles had core-shell structures with Y, O and Mn in the cores and V, Cr and Ta rich shells dependent on the chemical composition [53, 54], which is complicated as expected.

Minor additional elements such as V and Mn may play a similar important role as Ti. The nature of core-shell structures of the oxide particles, although explained mainly through two alternative mechanisms, remains an open question. The first argument considers the shell as a means of segregation of elements to the particle/matrix

interface during the cooling after particles were formed [54, 55]. The second mechanism explains the presence of the shell as necessary to decrease the interfacial energy in order to help stabilize Y_2O_3 against nucleation energy [53]. More information related to ODS steels is given in a review article written by Odette et al[40].

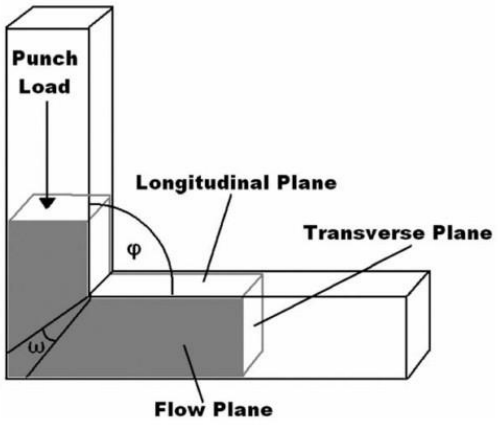

Figure 1.4 Schematic of ECAE with a die angle φ [51]

1.3 Brief introduction to the equal channel angular extrusion(ECAE) technique

Equal channel angular extrusion or pressing (ECAE or ECAP) was originally designed as a deformation method by simple shear, and later became popular as a severe plastic deformation (SPD) technique widely adopted to produce ultrafine grained (UFG) materials [56-61]. This technique was first developed in the former Soviet Union by Segal in 1972 and patented in 1977 [62], and introduced into the United States in the early 1990s. Fig.1.4 illustrates the ECAE process. Three planes (flow plane, longitudinal plane and transverse plane) are shown on the illustration. A high punch load is applied to force the billet through a channel of constant cross section that contains an abrupt angle.

Severe shear strain is introduced into the work piece at the shear plane (channel intersection). Each extrusion pass imparts a plastic strain of 1.15 for a 90° tool. Because the existing billets has similar dimension to the input billet, multi pass extrusions can be applied to achieve a high total strain levels. The following will briefly introduce the basic information about ECAE routes, refining effects, and mechanical performance which is of primary interest for ECAE processed materials.

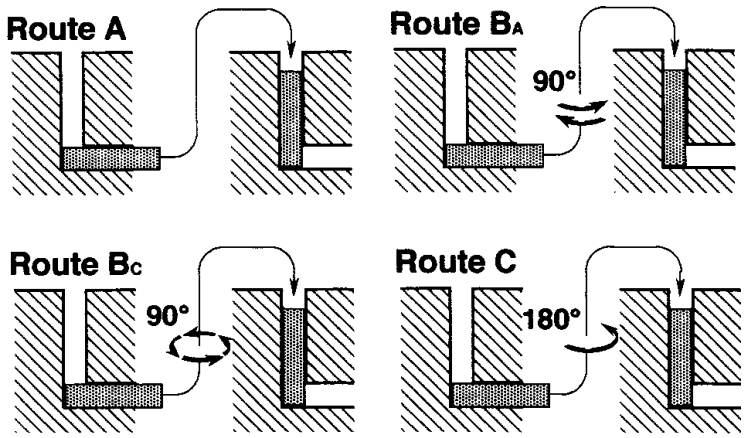

Figure 1.5 Fundamental routes can be chosen during ECAE processing of a billet [63]

1.3.1 The four routes of ECAE and their influence on microstructure refinement

Different ECAE processing routes can be defined according to the geometry of the tool. For square cross section tools, there are four well established routes. The four basic routes for a billet subjected to ECAE are illustrated in Fig.1.5. Route A involve no rotation of the work pieces between the subsequent extrusions. Route C involves a 180 degree rotation. Route B involved a 90 degree alternative (+/-) rotation between each pass, and B_C denotes a 90 degree rotation in the same direction between each pass.

Rotation around the extrusion axis for the different routes alters the morphology and texture of the microstructure. The shear characteristic related to different route is shown in Fig.1.6.

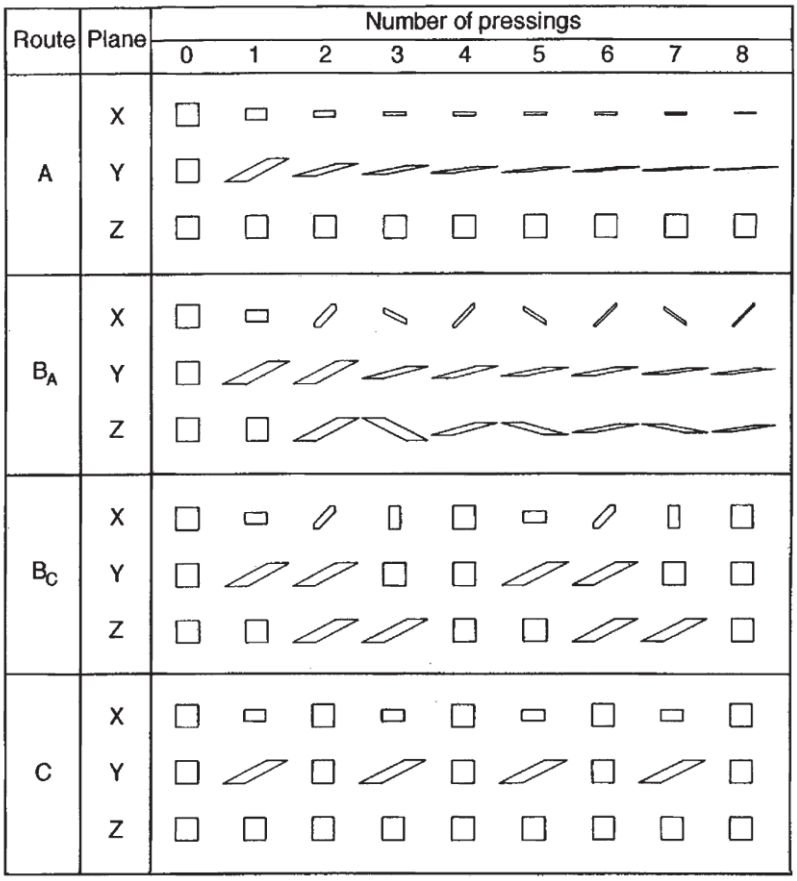

Figure 1.6 Shear characteristics on the three projected planes for four different ECAE routes up to 8 passes [56], where X is transverse plane, Y is the flow plane, Z refers to the longitude plane.

The refinement effects of routes and number of passes are summarized in [56, 64-66]. Due to a 180° rotation, the direction of shear is reversed after each pass, so the strain is restored after an even number of extrusions for route C. Route B_C also suffers

from a similar issue, because the shear strain during the first pass is cancelled by the third pass. Route A and route B are not considered as a redundant strain process, and the strain is accumulated. Four extrusion passes are commonly involved during route Bc processing, and this route commonly shows better refinement than route A and C for same number of passes.

ECAE processing enables the average grain size of metal alloys to be successfully refined to several hundred nm in numerous materials [67]. The population of high angle grain boundaries induced by ECAE typically increases with the level of strain, and significant strengthening is a frequent outcome of the ECAE process [67]. The general mechanism for grain refinement is a dislocation dominated process [57]. For example, in pure copper, the refining mechanism of the first pass is summarized as [68]: (a) dislocation generation, (b) dislocation cell formation,(c) gliding along the main slip planes and formation of an elongated laminar structure, and (d) the formation secondary micro bands due to the activation of other slip systems. However, some other refining mechanism could occur rather than the dislocation mechanism. For instance, in 304L stainless steel, deformation twinning and martensite transformation can interact with the formation of shear band, which results a further refining of the microstructure [69]. The twinning related mechanism could also extend to the HCP metal and alloys such as Ti and titanium alloys [70, 71] and magnesium alloys [72-74].

The ECAE process can be divided into cold-ECAE and hot-ECAE, depending on whether or not the processing temperature is below or above the recrystallization temperature of the material. Cold ECAE can significantly enhance the strength, but

ductility is reduced. Hot-ECAE process leads to less pronounced hardening but retention of ductility and work hardening ability. After post-annealing, a cold-ECAEed low carbon steel can regain ductility with excellent strength [75].Post-annealing of a cold-ECAEed precipitation hardening Al-Ag alloy can give an excellent combination of strength and ductility [76]. After Hot-ECAE, a spray-cast 7034 Al alloy showed redistributed precipitates [77]. The tempered EUROFER 97 steel can be strengthened without significant loss of ductility by hot-ECAE [78]. These thermo mechanical treatments (TMT), involved in ECAE or other kinds of SPD and heat treatment (HT), are frequently applied to pure metals and alloys to achieve high strength and ductility or microstructure homogeneity.

Compared with grain refinement mechanisms via ECAE, the evolution of precipitates or second phase particles during extrusion is poorly understood and less documented. Mechanical deformation can have a significant effect on the fracture and redistribution of particles in precipitation-hardened Al alloys studies [79, 80], where the precipitates commonly have a long plate or rod shape which can be broken or fractured during ECAE. Previous studies on Al based metal matrix composites show limited broken Al_2O_3 particles which were refined via the ECAE process [81]. The high processing temperature was blamed for the lack of refinement of the particles.

1.3.2 Mechanical performance of ECAE processed materials

Enhanced mechanical performance is one of the major prospects of ECAEed materials. The overall performance of ECAE processed materials can be summarized as

a strength and ductility paradox [83]: the strength increase is often accompanied by a sacrifice of ductility. This issue is more pronounced when materials are processed at lower temperature [76, 83, 84]. Fig.1.7 shows a set of typical strain stress curves of interstitial free (IF) steel extruded using a plate tool up to 8 passes [82]. The as-received IF steel has a total elongation up to 42%. While after extrusion, the elongation is decreased to around 15%. The yield strength is increased from below 200 to 500MPa.

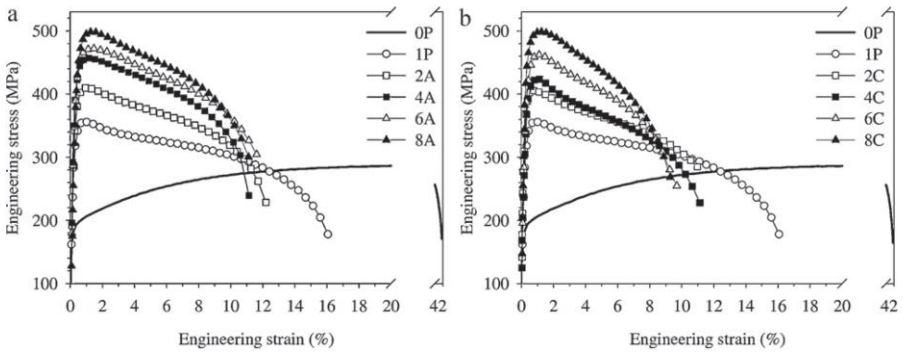

Figure 1.7 A typical stress strain curves of ECAEed interstitial free (IF) steels [82]

This issue can be alleviated through a post-processing heat treatment. Post-annealing of the ECAEed low carbon steel can improve ductility compared to as-extruded material[85]. Through cryogenic rolling with post-processing heat treatment, high strength and high ductility have been achieved simultaneously in pure copper with a bimodal structure [86]. This finding clarifies the idea of using thermomechanical treatment (TMT) combination ECAE with or other SPD processing methods with heat treatment to achieve high strength and high ductility in other engineering alloys[76, 84, 87, 88]. This method is also used in current T91 steel as discussed in a later chapter.

1.4 Radiation damage in structural steels

When high energy particles are projected into the solid material, the atoms of the solid material can be displaced from their regular lattice positions up to hundreds of times. This displacement damage can bring number of the vacancy-interstitial pairs far from their equilibrium concentration. The destiny of these points defects is either to be removed through a mutual recombination or reaction with defect sinks such as grain boundaries, dislocations, or impurity atoms and precipitates, or to accumulate to form clusters, such as dislocation loops, voids, or stacking fault tetrahedron (SFT) [89]. These point defects and their notorious byproducts can influence fundamental process such as diffusion and dislocation movement, which further degenerate the mechanical properties and can cause unexpected failure. Three major issues which contribute to the failure of structural materials will be discussed here. They are irradiation induced swelling, embitterment, and segregation corresponding to structural integrity, degeneration of mechanical properties, and corrosion resistance of structure materials, respectively.

1.4.1 Swelling

Quench induced vacancy clusters such as stacking fault tetrahedral [90] and voids [91, 92] have been observed since the late 1950s and early 1960s. However, the first irradiation induced voids were observed in a 316 stainless steel after post-examination of cladding service by Cawthorne et al in 1967 [93] as shown in Fig. 1.8. The voids developed in these samples are thought to have been formed by condensation of vacancies on helium nuclei due to the (n, α) reaction. During high temperature

annealing, these voids can be dissolved, which further confirmed the voids formed are not helium bubbles. The hoop stress generated during the cladding process can assist in the growth of voids but is not an essential prerequisite for the formation of voids, because of the fact that void formation is also observed in other unstressed steels.

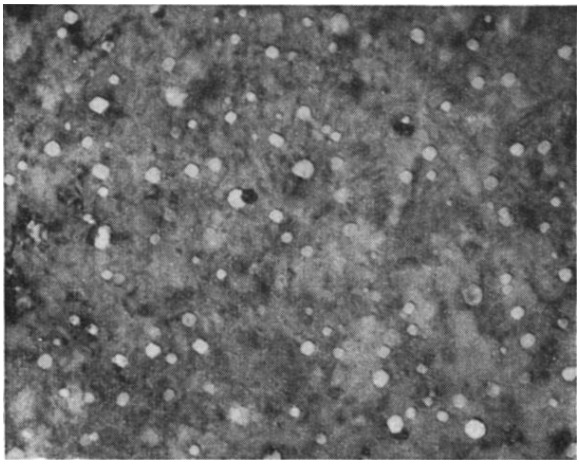

Figure 1.8 First void induced swelling observation of irradiated 316 stainless steel [93]. This sample was irradiated at 510°C by neutrons to a dose of $4.7\times10^{22}cm^{-2}$.

This void swelling phenomenon raises great interest. Pure metals like nickel, tungsten, molybdenum and vanadium were irradiated to repeat void swelling observation [94-96]. These studies proved that the formation of voids during irradiation is a widespread phenomenon. During this period, experimental approaches were developed to simulate neutron irradiation by using heavy ions[97] and high voltage electrons[98]. These methods avoided handling radiation "hot" materials after neutron irradiation and helped to isolate the factors that influence void swelling. For high voltage electron irradiation, in-situ experiments can also be performed to better understanding the process of void growth. Several important conclusions were drawn from flooded experiment

studies [99-101], including the fact that the void swelling is sensitive to composition and minor impurities[100, 102]. Pure metal is often less swelling resistant than the alloys. The simulation of swelling by electron irradiation always suffers from a surface effect [101]. An injected interstitial effect is proposed to explain the atypical neutron irradiation process of heavy ion [103-105]. The effect of helium is proposed as a mechanism to help stabilize the void nucleation [106]. Grain size effect studies note that fine grained materials exhibited better irradiation tolerance than their coarse grained counterparts [107]. Ferritic steels show better swelling resistance than austenitic steel after neutron irradiation [108]. The steady state swell rates of ferrite steels are around 0.2%/dpa compared with those of ~1%/dpa of austenitic stainless steel [109].

Theoretical methods have also been explored to understand the formation of voids and swelling. The process of dislocations was proposed as a bias defect sink preferentially to absorb interstitials, yielding a net vacancy flux within the material moving towards void surfaces [110]. A kinetic rate theory relating the swelling to void growth was developed by Brailsford and Bullough et al [110, 111]. The basic assumption is that existing defect sinks, such as dislocations, can absorb interstitials preferentially, yielding net vacancies drifting to the void surface. Kinetic theories were also derived for various types of defect sinks such as grain boundaries and free surfaces [112] and their potential influence on the fundamental processes such as diffusion [113]. At the same time, other researchers focused on atypical neutron process of heavy ion irradiation. They developed a temperature shift effect based on kinetic rate theory [106, 114-116], through which the heavy ion irradiation process can simulate neutron

irradiation with a shifted radiation temperature. This theory predict injected interstitial effects that match very well with the void growth theory developed by Russell [117], where the nucleation of voids is derived by considering solvent interstitials.

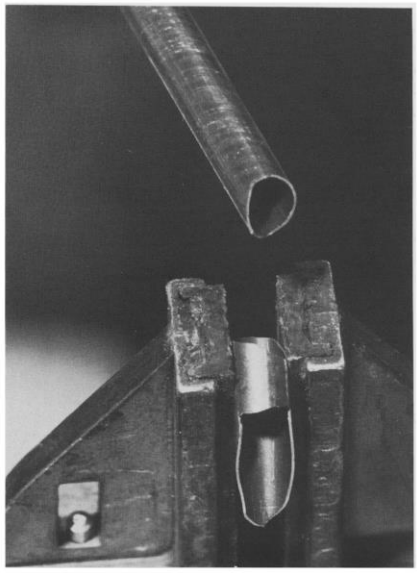

Figure 1.9 AISI 316SS suffered from severe embrittlement after irradiation to 130DPA at a hoop stress of 276MPa at 400°C [118]

1.4.2 Irradiation induced degradation of mechanical properties

The mechanical properties of structure materials can be significantly reduced by irradiation. A typical example in austenitic steel is radiation induced embrittlement [118, 119], while in ferritic/martensitic steel a more typical concern is the shift of the ductile brittle transition temperature (DBTT) [120]. Irradiation induced embrittlement is often discussed together with irradiation induced hardening, because of the stress and strain paradox. Any factor that increases the strength will yield a decrease of ductility for the same material without exception. F. Garner et al found that a typical results of austenitic

316SS after irradiation [118], was extreme brittleness. One of these materials even failed when pulled out of the test assembly. Another was broken into three pieces with one falling to the floor during clamping as shown in Fig.1.9. Copper impurity atoms were partially blamed for the embrittlement because of the fact that copper is immiscible with iron and can easily precipitate during heat treatment and irradiation [121, 122]. Copper precipitation can take several interesting close packing structures within the Fe matrix. More information related to the structure of these precipitates is given in references [123-125].

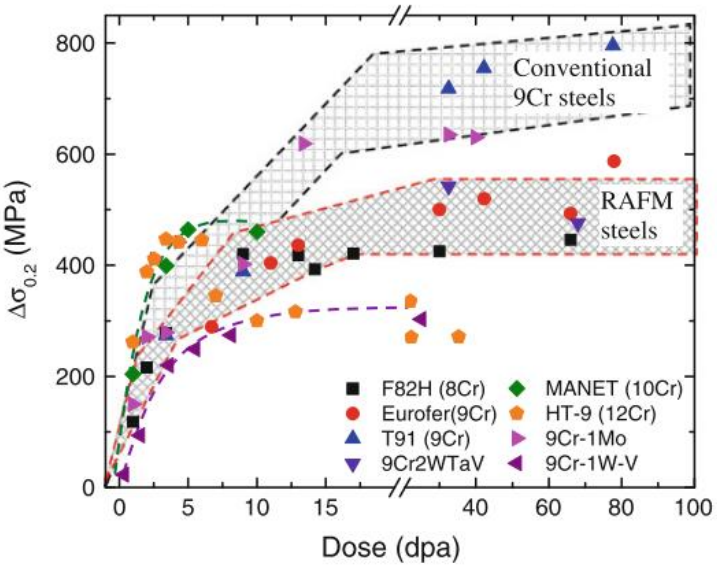

Figure 1.10 Dose dependent irradiation induced hardening of various F/M steels at a temperature less than 300°C [126]

Typical dose dependent irradiation induced hardening in F/M steels is shown in Fig.1.10. The hardening effect reaches a plateau after about ten dpa dose. This plateau corresponds very well with the early observation of a DBTT shift saturation [127].

Source hardening and friction hardening are proposed as two major mechanisms to explain the radiation hardening which refer to dislocation generation and movement [89], respectively. Source hardening is proposed to explain Luders band formation in irradiated copper by [128]in 1965. A new theory is proposed on this topic by Singh et al [129]. They propose the cascade itself can occur in the vicinity of dislocations. For this case, dislocations need to break away from the cascade products as loops or clusters. This process requires additional stress.

1.4.3 Radiation induced segregation (RIS)

Irradiation assisted stress corrosion cracking (IASCC) is a dominant failure mode in light water reactors. There are many factors that can affect SCC, including, corrosion potential, thermal gradient, water chemistry, stress status of the material, temperature and chemical composition of the materials. Radiation induced segregation (RIS) at various defect sinks, such as grain boundaries, dislocations, and precipitation interfaces, can change the chemical composition significantly. RIS is recognized as the main contributor to the IASCC failure and can occur at very low dpa values during the early service of structure materials [130, 131]. This problem was initially predicted by Anthony [132] and identified by Okamato [133], that segregation can occur at free surfaces. Later, it were extended to other defect sinks such as voids, grain boundaries and dislocations during radiation. The atomic size difference was proposed to explain the phenomena where undersize and oversize atoms migrated towards and away from surfaces[134]. This phenomena was qualitatively explained as an inverse Kirkendall (IK)

effect proposed by Marwick [135], where the defect flux coupled with the atoms to move together. For instance, undersized atoms can take the dumbbell site of interstitials, and be dragged to the sinks.

The IK model predicts very well for austenitic stainless steels [136]. However, when the IK model is applied to F/M steels, it cannot explain the conflicting results given by different steels [137]. For instance, Cr elements are enriched at the grain boundaries in HT9 while depleted in the vicinity of grain boundaries in F82H after irradiation, both of which are actually F/M steels. Was et al proposed that the differences in vacancy migration energies play a key role in the directions of segregation [131], while connected interstitial binding with solute atoms, as proposed before, may be less predominate. Wharry et al [138]introduced a concept of Cr: Fe diffusion coefficient ratios for vacancies and interstitials. A critical temperature was found below which Cr will enrich and compromise an interstitials flux and above which Cr will deplete via a vacancy flux. The IK model can be extended to explain the results observed in F/M steels.

1.5 Design of radiation tolerance materials via defect engineering

Defect sinks, such as dislocations, impurity atoms, phase boundaries, layer interfaces, grain boundaries (GBs), twin boundaries and free surfaces, can annihilate irradiation induced defects, and consequently enhance radiation tolerance of irradiated materials [139-141]. Based on these sinks, materials with high density of defect sinks can be fabricated for potential irradiation tolerance application.

In addition, multilayer interfaces can be designed with controled thickness to serve as defect sinks[142]. Molecular dynamics simulations suggest that, at a Cu/Nb interface, the two types of K-S orientation relationships can convert alternatively by absorbing a vacancy or an interstitial and form jogs. Such a process makes the Cu/Nb interface inexhaustible sinks for radiation induced defects [143]. Experimental studies of He ion irradiated multilayers, such as Cu/Nb [144, 145], Cu/Mo [146], Cu/V [147, 148], Fe/W [149] and V/Ag [150], Ag/Ni[151, 152] show clearly a size dependent enhancement of radiation tolerance, i.e. the density of He bubbles, lattice distortion, swelling and radiation hardening were much less in films with thinner individual layer thickness.

The grain boundary, an important type of defect sink, has attracted increasing attention. Direct evidence of defect clusters captured by high angle GBs was observed during *in situ* irradiation of nanocrystalline nickel by Sun *et al.*[153]. In addition, void denuded zones (VDZs) have been frequently observed in the vicinity of GBs of various metallic materials irradiated at elevated temperatures [154-156]. Sink efficiencies of GBs were evaluated as a function of their characters (coherency and misorientation angle) in several metals [154, 156, 157]. Molecular dynamic (MD) simulations have also been used to reveal defect evolution in the vicinity of GBs. Samaras *et al.* observed migration of atoms toward GB zones during thermal spikes [158]. Bai *et al.* reported a "loading-unloading" mechanism where interstitials can be first absorbed by GBs and then reemitted into grain interiors to annihilate vacancies [159]. Chen *et al.* further found that the annihilation process is often mediated by other point defects near GBs in Fe

[160]. In general, GBs have been thought to be effective sinks for irradiation-induced defects.

Due to higher GB volume fractions compared to their coarse-grained (CG) counterparts (d > 1000 nm), nanocrystalline (NC) materials (d < 100 nm) offer promise for enhanced radiation tolerance [161]. An initial study by Singh *et al.* showed that void swelling of stainless steel can be effectively inhibited by decreasing grain size, under 1 MeV electron radiation [107]. This observation was also supported by the theoretical model derived by Bullough *et al.* [112], which predicts the sink strength of GBs and grain size follow a power function relationship with a negative exponent. Irradiation-induced defects are found to be thermally unstable in NC Au even at room temperature [162]. Experimental studies of heavy or helium ion irradiated NC metals or ceramics, such as Pd and ZrO_2 [163], Fe [164] and TiN [165], show clear enhancement of radiation tolerance, i.e. in general the density of defects and helium bubbles were much lower compared to their CG counterparts. NC intermetallic NiTi and ceramic $MgGa_2O_4$ exhibited better resistance to amorphization under heavy ion irradiation compared to their CG counterparts [166, 167]. However, the opposite size-effect of irradiation-induced amorphization was also observed in ZrO_2 irradiated by Xe heavy ions [168], where ZrO_2 nanoparticles amorphized at a dose two orders magnitude lower than that of its CG bulk counterpart. To address such a contradictory issue, Shen proposed a model based on the Gibbs free energy of GB, which suggests that there is an optimum grain size for maximum radiation tolerance of a particular material [169]. Despite enhanced radiation tolerance, grain coarsening of some NC materials can occur during irradiation

[170-172]. Furthermore, bulk NC materials are still challenging to fabricate, which is a practical limitation for structural applications.

1.6 Motivation and objectives

The motivation of this thesis is to explore mechanical properties, thermal stability, and radiation tolerance of ECAE enabled TMT processed F/M steels. These studies have both practical and fundamental significance. Applications including reactor pressure vessels or piping systems would benefit from the increasing strength (without loss of ductility) in T91 steels. Also, T91 has been developed for different strength levels, which allows a single material to serve for both high strength and low strength application like bolting and baffles. The influence of TMT (via ECAE and post extrusion annealing) on the evolution of precipitates and mechanical properties has not been investigated and may contribute to new knowledge. Extrusion of ODS steels was studied initially to illustrate the possibility to redistribute nanosize particles via SPD. Understanding the grain size effect on radiation tolerance in these reactor steels has both fundamental and practical significance for potential applications in nuclear reactors.

CHAPTER II

MATERIALS AND PROCEDURES

In this chapter, the materials investigated in this thesis are introduced with detailed information. The design of the experiments is explained. The methods, experiments and facilities are described to increase the clarity of the experiments. Related information is detailed for continuing or repeating the work presented in this thesis.

2.1 Chemical composition of T91 steel and ODS steels under study

The chemical composition (in wt.%) of the present T91 alloy is listed in Table 2.1. The as-received (AR) T91 steel was hot-rolled and then heat-treated by a standard normalization (1038°C for 0.5 hour with air cooling) and tempering (760°C for 0.5 hour and air cooling)procedures described in the literature[27].

Table 2.1 The chemical composition (in wt%) of T91 steel.

Element	Specifications of T91	
	Modified T91 standard	Present study
Cr	8.0/9.5	9.376
Mo	0.85/1.05	0.911
C	0.08/0.12	0.085
Mn	0.3/0.6	0.379
Si	0.2/0.5	0.366
N	0.03/0.07	0.042
Nb	0.06/0.10	0.08
V	0.18/0.25	0.189
Cu		0.08
Ni		0.097
Al		0.032
P		0.019
S		0.0008
Fe		Bal.

The ODS alloys were prepared by mechanical alloying (MA). Elemental powders were blended with 70 micron of Fe particles, and Cr, Ta, V, and W particles of less than 10 microns in diameters, and 20 nm yttrium oxide (Y_2O_3) nanoparticles. The MA process was carried out using a planetary ball mill operated in a glove box protected by UHP Argon gas. The ball-to-powder ratio was 15:1. The milling time was typically 12 hrs. After degassing by a gas mixture of argon and hydrogen, the ball milled powders were consolidated by HIPping (hot isostatic pressing) at 1150 ℃ for 4 hrs under 100 atm pressure. The nominal chemical composition of the alloy is detailed in Table 2.1. The metallic elements are supposed to be accurate and do not deviate far from the nominate composition. The values given for non-metallic elements are measured except Boron, which is hard to measure.

Table 2.2 The chemical composition in (wt.%) of 2103H and 2104H ODS steel, the metallic elements are nominate, while non-metallic materials are measured except Boron .

Element	Specifications of ODS	
	2103H	2104H
Cr	12	12
W	1.1	1.1
V	0.2	0.2
Ta	0.14	0.14
Y	0.24	0.24
C	0.0134	0.0122
O	0.7509	0.3134
N	1.546	0.319
B		0.002
Fe	Bal.	Bal.

2.2 Experiments

The experiments designed include the following:(a) austenitizing (normalization)of T91; (b) ECAE of T91 steel with several heat treatment conditions; (c)

ECAE of ODS steel, and their thermal stability;(d) Mechanical performance and microstructure characterization of T91 steel (tensile test) and ODS steels (hardness); (e) heavy ion radiation experiments on the T91 steel.

The austenitizing experiment is performed to understand the phase transition of T91 steel. The ART91 is heat treated to 800, 900, 1000, 1100, 1200°C and austenizited for 1h, then quenched into ice waters. Air cooling or furnace cooling was also performed for selected samples. Specially, the 800°C normalization specimens were furnace cooled to get fully ferrite structure. This sample is denoted as as-annealed (AA) T91.

ECAE of T91 with a selected phase constitution was performed to give different grain sizes and deformed microstructures of the steel. The AA materials were ECAE processed up to two passes following route B at 300°C. The AR T91 steel was extruded up to two or three passes following route Bc at 625°C or 700°C.The less tempered T91steel was also ECAE processed to understand how tempered martensite deformed. Extrusion at 1000°Cwas also performed to understand the ausforming influence on the microstructure and properties.

Both ODS steels were ECAE processed. The original idea of this effort was to redistribute the tiny oxide particles and homogenize the microstructure. The extrusions were performed at 700°C up to two passes following route B or C. Extrusion at 300°Cwas also achieved. Unfortunately, the 2103H sample failed during low temperature extrusion at 300°C. Further ECAE processing at lower temperature were not pursued due to the limitation of the tool.

The mechanical performance of T91 steel was investigated by tensile tests to give an overall evaluation of the temperature and number of passes influence on the T91 steel. The mechanical performance of ODS steel was characterized by the hardness due to the limitation of samples size, which was limited for tensile tests. Thermal stability measurements were performed for both materials to understand the degeneration of ECAE processed materials, which is a practical limitation for structural applications. Selected worked T91 steels were annealed at 300,500,600, 700, and 800°C for one or ten hours. Both ODS steels (deformed and not deformed) were annealed at 700, 900, 1100, 1300°C for 10h.

Heavy ion irradiation was applied to selected samples of T91 steel to evaluate the performance of radiation tolerance. The T91 steel was exposed to a high dose at intermediate temperatures around 450°. This experiment was performed to simulate neutron irradiation of T91 up to a high dose targeting practical applications.

Intensive microstructure characterization at different scales is performed to understand the relationship between processing, performance, and microstructure of both steels under different conditions (before or after deformation, heat treatment, and irradiation).

2.3 Experimental details

In this section, the details of experiments are given so that others could repeat or conduct similar experiments in the future. These experimental details include sample preparation, ECAE processing parameters, the time and temperature of heat treatment,

the parameters used for mechanical testing, and the electron microscope sample preparation and imaging conditions.

2.3.1 Sample preparation for different experiments

2.3.1.1 T91 sample preparation

The AR T91 steel was in plate form with thickness ~ 25.4 mm. Billets with dimensions 25.4 × 25.4× 50.8 mm were cut by electro discharge machining (EDM) from the AR plate for heat treatment. The ECAE extrusion billets were cut with dimensions25.4 × 25.4× 127 ~152.4 mm. After extrusion, small square specimens with 10 × 10× 5 mm were cut for optical, scanning electron microscopy and hardness tests. Prior to optical observation, the samples were mechanical polished following the standard procedure and etched. Thin discs with 3 mm diameter were EDM for transmission electron microscopy (TEM) observation. The discs were first mechanically polished to a thickness of 50μm, and then electro-polished using a 10% (volume fraction) perchloric acid plus methanol solution at -40 °C with a voltage of 10 - 20 V. The etching temperature is a key factor during the sample preparation process. Dogbone-shaped tensile samples with gauge dimensions of 8 × 3× 1 mm were cut from the ECAE processed billets using electro discharge machining (EDM) as shown in Fig 2.1.Prior to tensile tests, the samples were electro-polished to remove the porous oxide layer left by the EDM. The electrolyte solution is a 1:1 mixture of sulfuric acid and phosphoric acid. The polishing was performed at room temperature with a voltage 8~10 V. Some of the optical microscope (OM) and SEM observation samples were cut from the tensile

specimen away from the deformation zone to give the status of the specimens before deformation. For radiation experiments, samples with dimensions 3 × 3× 1 mm were cut from the processed bar using electro discharge machining (EDM). Prior to irradiation, samples were first mechanically polished, then electro-polished to remove surface deformation effects. Cross-sectional TEM (XTEM) specimens were prepared using the focused ion beam (FIB) technique. All TEM images were taken from the irradiated XTEM specimens. A 50 nm thick Nb cap layer was sputtered onto the irradiated T91 steels as a marker of the specimen surface.

2.3.1.2 ODS samples preparation

The AR ODS steel arrived asa rod bar with a diameter of 12.5 mm and a length of 200 mm. The bars were cut in half and canned in 316SS to fit the size of ECAE tool (25×25 mm cross section). The can was made of 316L SS. Cans of 304L SS were also tried but tended to shear localize and fractured during ECAE. After extrusion, the cans were machined off and the deformed bar cut into 1 mm thickness slabs for microstructure analysis. The SEM samples were electrochemically etched using a 10g KOH in 100ml water solution, which selectively etched the Cr rich phases. The mixture solution is a diluted modified solution found effective from prior work [173]. The voltage of electro polishing was around 8~10 V. This solution can be heated to accelerate the polishing if necessary. The TEM sample preparation technique is exactly same for T91 steels. Further treatment with ion milling can be used to cut open the

particles within the matrix for close examination. This will be detailed again in the other chapters.

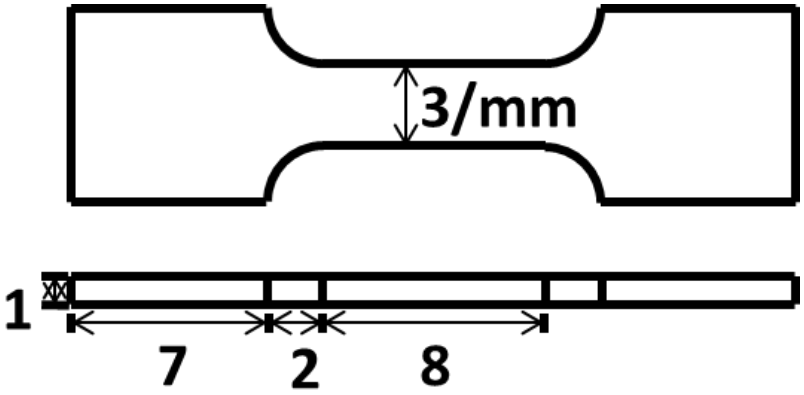

Figure 2.1 The dimension in mm for tensile test samples used in this thesis

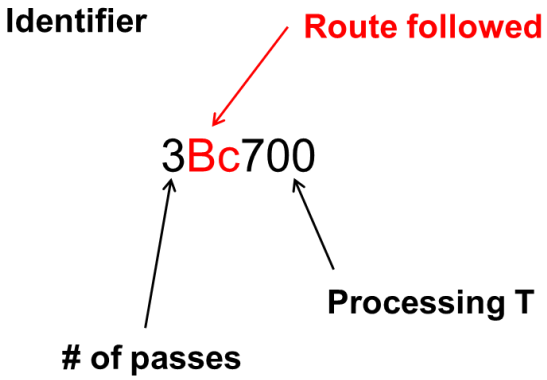

Figure 2.2 The identifier of ECAE processed samples includes information as the number of passes, the route followed, and processing temperature

2.3.2 Equal channel angular extrusion (ECAE) processing

ECAE processing was carried out on an MTS-controlled hydraulic press with 225 ton (2.22×10^3 kN) force capacity. For processing at elevated temperature, billets

were water quenched after ECAE processing. High temperature extrusions were realized by preheating billets for 1h at the desired temperature in a box furnace. The extrusion speed was chosen as 0.003inch/s during room temperature and 300°C extrusions. The billets were lubricated with "anti-seize" commercial lubricant.

During the ausforming process of T91 steel, billets were heated to 1000°C for 1h to the austenite phase field, and extruded at a rate of 1 inch/s, and immediately water quenched. The billets were at 1000°C and the die was at 300°C. The fast extrusion rate was applied to maintain the temperature of the billets close to 1000°C so that no phase transformation occurred during the extrusion. The other elevated temperature ECAE of T91 and ODS steel followed the same strategy of the ausforming processing.

Table 2.3 Successfully ECAE processed specimens used in present thesis. The bold letters indicate the sample were processed by a collaborator.

Materials	Low temperature		High temperature		
T91	1A27/1ART	1A300	1A625	***3Bc700***	1A1000
		2B300	***2B625***		
		1A300+			
2103H ODS				2B700	
				2C700	
2104H ODS		1A300		2B700	
				2C700	

The nomenclature for the ECAE processed samples is described in Fig. 2.2. The identifier gives all the information of processing parameters such as route, passes, and processing temperature. The successfully processed billets are listed in Table 2.3. More attempts were tried for both ODS and T91 steel. It was discovered that a high speed extrusion at lower temperatures inevitably causes shear localization. The samples 2B625 and 3Bc700 were extruded by another student (David. C. Foley) working on the same

materials. His ECAE processing covered 300 to 600°C, and all of which failed. When the temperature increased to 625°C, the billet survived after two passes. The canned materials included all the ODS bars and 1A300+. The later was an extrusion of tempered martensite (low temperature). Extrusion of tempered martensite can damage the tool or cause an over load if not encapsulated in stainless steel.

Typical load vs stroke extrusion curves for ODS are shown in Fig.2.3. The billets deform easily at 700°C. An additional extrusion causes the load to increase tremendously. The load for a single pass extrusion at 300°C is as high as that of the second pass at 700°C following route B.

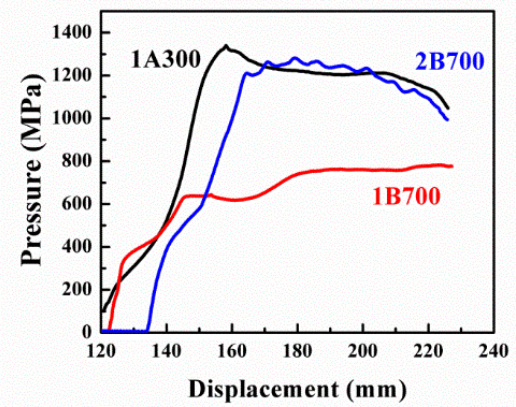

Figure 2.3 The stress (pressure) applied vs. displacement during ECAE processing at various 300 and 700 °C of 2104H ODS steel.

2.3.3 Heat treatment

The austenization experiments were performed in a box furnace with a maximum temperature of 1300±10 °C. The furnace was preheated to the target temperature. The billets were then put in the center of the furnace. Post-processing heat treatments were

carried out in a quartz tube with the protection of ultra-high purity argon gas flow, and then furnace cooled. This heat treatment was used for small samples for lower temperatures (below 1000°C). The temperature was monitored by a thermocouple, mounted above the sample in the center of the furnace. The error in temperature was supposed to be within 5 degree C. Some selected TMT conditions (including heat treatment and ECAE) for varies samples are summarized in Table 2.4. Other sample identifiers will follow the same nomenclature logic presented in the other chapters.

Table 2.4 Heat treatments and thermomechanical processing conditions of selected samples

Identifiers	**TMT processing condition**
AA	anneal as-received material at 800°C for 1h, followed by furnace cooling
800WQ	normalize at 800°C for 1h, followed by water quenching
1000WQ	normalize at 1000°C for 1h, followed by water quenching
1000AC	normalize at 1000°C for 1h, followed by air cooling
1000ECAE	one pass ECAE at 1000°C and water quench
1000WQ/500 10h	anneal 1000WQ sample at 500°C for 10h
1ART	one pass ECAE at room temperature

2.3.4 Mechanical tests

Tensile tests were performed with an MTS machine at a cross head speed of 0.008 mm/s. The hardness for the thermal stability study was measured by an LM 300AT micro hardness tester using a 2.9 N (300g) force for a loading time of 13 s by using a pyramidal shape diamond indenter. The hardness tester was always calibrated prior to the experiments. Tensile tests give information related to yield strength, ultimate tensile strength, elongation-to-failure, and Young's modulus. Hardness measurements can only give the hardness. No ductility information can be extracted from the hardness data.

2.3.5 Heavy ion irradiation experiments

Fe ions accelerated to 3.5 MeV were implanted into AA and 2B300 T91 steel at 450°C. The recrystallization temperature is ~500°C. The 450°C was selected to avoid the complexity caused by grain growth. This particular temperature is also targeted for current pressurized water reactors (~280-~350°C), and relevant for sodium cooled fast reactors and lead fast reactors. A defocused ion beam (without rastering) was used during the implantation process. Irradiation damage profiles were estimated using SRIM (stopping ranges of ions in matter) by selecting the Kinchin-Pease (K-P) model option (quick calculation model), as suggested by Stoller at al[174].A fluence of 9×10^{20} ions/m^2 was achieved, corresponding to a peak damage of 150 displacements per atom (dpa). This dpa value is a factor of ~½ of that predicted by the full cascade mode.

2.3.6 Microstructure characterization

Various characterization techniques are introduced during this section including optical, SEM, and TEM. Some related techniques are also addressed. The overall idea is that it is almost impossible to understand these steels with adequate comprehension without a combination of two or three different scale imaging techniques.

2.3.6.1 Optical observation

The optical images can give an overall view of the microstructure of these steels. Identifying the etching solution is the most important step to get good imaging. In this thesis, two solutions were tried for T91 steels. The first was a mixture of 5ml HNO_3,

plus 3ml H_2SO_4plus 92ml HCl acid, which was provided by a collaborator. The other, used for etching, was a 5g $FeCl_3$ plus 20ml HCl plus 100 ml water solution[175].The etching time varied from specimen to specimen, but generally occurred within a few seconds. The effect of etching is shown in Fig.2.4. The different color in the images results from different polarization or height, which could be influenced differently by different phase or the same phase with a different orientation, which is related to the etching speed. The first solution is commonly used to give a heavy etch and the second is for lightly etched which is easier to control. We used the second solution for the images in the thesis unless otherwise mentioned. An effective etching solution for ODS steel is not identified. No optical images of ODS steel are shown in the later chapters.

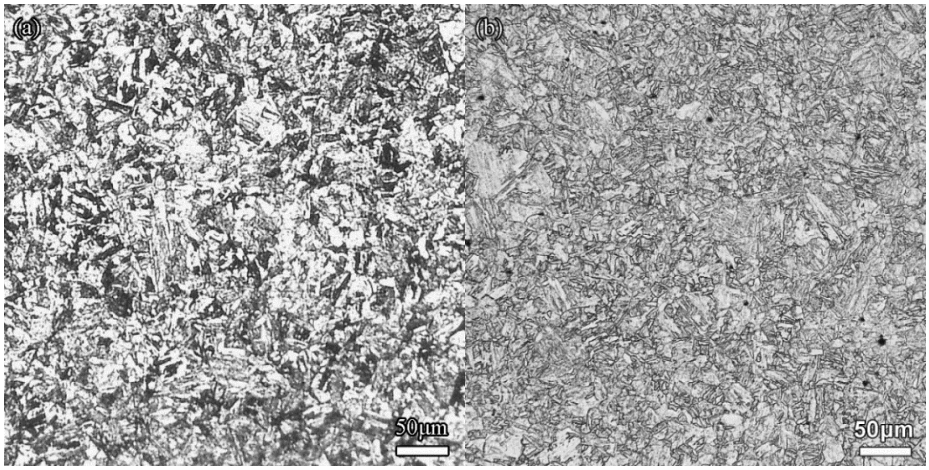

Figure 2.4 The effect of etching using different solutions: (a) etched by 5ml HNO_3, and 3 ml H_2SO_4 and 92ml HCl acid, and (b) etched by a 5g $FeCl_3$, 20ml HCl, and 100 ml water solution

2.3.6.2 SEM observation

Scanning electron microscopy (SEM) was performed on an FEI Quanta 600 microscope operated at an acceleration voltage of 20 kV at a working distance of 10

mm. The etched specimens were used directly for SEM observation. SEM can give more information at a higher magnification. An example is given in Fig.2.5.The interpretation of SEM images is based on image contrasts. The severely attacked phase (deeper phase) , which appears to be darker color, is the ferrite phase. The less attacked phase was recognized as martensite or retained austenite. This will be discussed in more details in the following chapters.

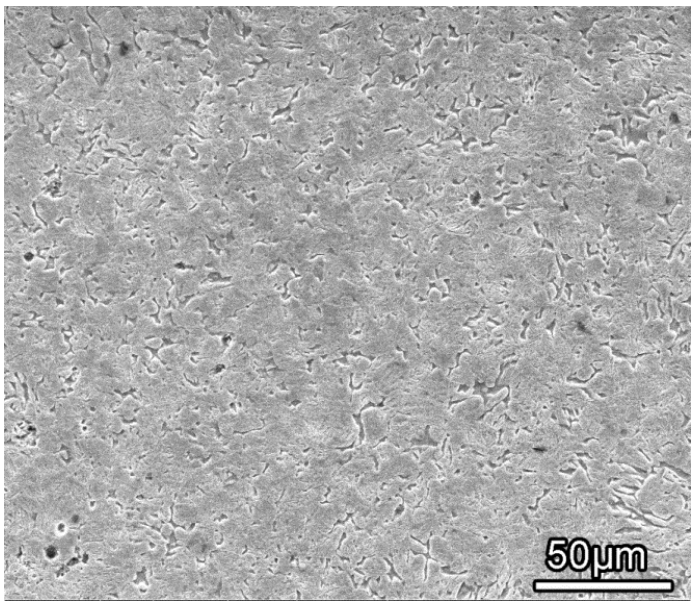

Figure 2.5 SEM image of ferritic/Martensitic T91 steel subjected to 800°C annealing for 1 h then water quenched.

2.3.6.3 TEM technique for observation

Transmission electron microscopy (TEM) experiments were performed using a JEOL 2010 transmission electron microscope operated at 200 kV. Selected area diffraction (SAD) patterns were taken by the JEOL 2010 with an inserted aperture about

~ 1.25 μm in diameter as shown in Fig. 2.6. The size of this aperture is important because it can allow a crude estimation of how many grains are involved in the diffraction process.

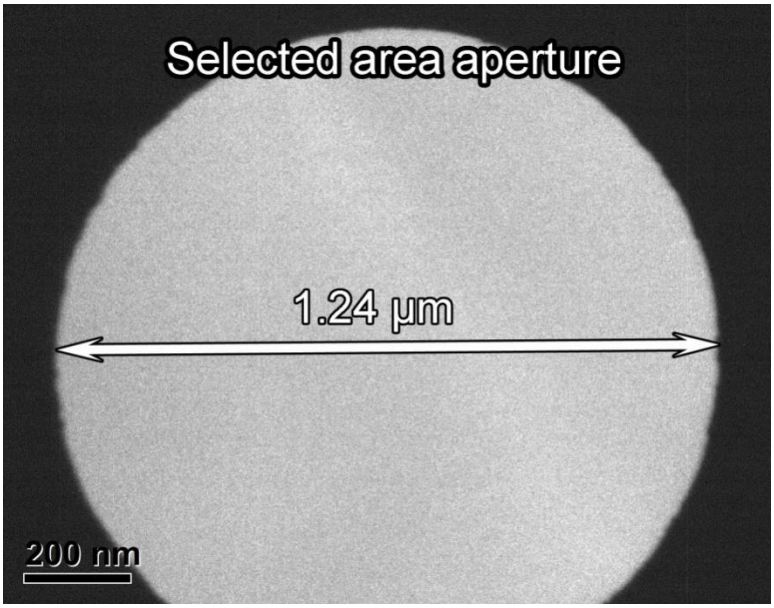

Figure 2.6 The largest selected area aperture used in the JEOL 2010 TEM for the in present work

Scanning transmission electron microscopy (STEM) studies were performed by using an FEI Tecnai F20 microscope operated at 200 kV, equipped with a high angle annular dark field (HAADF) detector and an Oxford instruments EDX detector. Before taking the images, the microscope was well aligned. Different spot sizes were chosen for different intentions.

Several special imaging techniques were used in the present work, such as high resolution TEM (HRTEM), two beam condition (TB) TEM, dark field image, and weak beam dark field imaging (WBDF) techniques. The HRTEM experiments is especially

important for the ODS steels, because the oxide particles are commonly at the scale of a few to tens of nanometers. TB and WBDF imaging are very important in the defect analysis in the irradiated materials. More details are given in reference[176], which is very important for interpretation of radiation damaged microstructures.

2.3.7 X-ray diffraction (XRD) experiments

X-ray diffraction (XRD) measurements were carried out on a Bruker-AXS D8 diffractometer. The step size was set at 0.05°/s for the quick scanning and 0.01°/s for detailed scanning. Lower noise results form a slow scanning speed, but the necessary time for lower noise increases significantly.

2.4 Summary

This chapter briefly introduced the materials used and sample preparation methods for different experiments. The design of experiments was discussed. The steps of experiments were given in some cases. The interpretations of some data were discussed. Cautions related to some experimental details were addressed to avoid making mistakes in future work.

CHAPTER III

PHASE TRANSITION OF T91 STEEL

In this chapter, the phase transition γ→α (austenite →ferrite) is reviewed. Several new observations were made. The dynamic transformation products of T91 steel are complicated as expected. A combination of different characterization techniques are applied to better understanding the microstructure of this steel.

3.1 The general phase nomenclature for steels

The dynamic products of phase transformations in steel have been studied for many years. For example, pure Fe with 0.011% C has four plateaus during rapid cooling from above the A3 temperature, which are quite complicated. These plateaus correspond to equiaxed ferrite, massive ferrite, bainite ferrite, and lath martensite at temperatures of 860, 760, 690 and 550°C [177]. The addition of Ni and Cr can change the relative difficulty in forming of these phases, which further complicate the situation. Related to these phases, some detailed mechanics of transition products are still poorly understood. For example, the bainite formation mechanism is still in controversy, although the bainite phase was found in the 1930s [178]. The core argument is related to whether or not bainitic ferrite initially forms with a super saturation of carbon. The classic phases in steels are introduced here based on the knowledge of reference [4].

Polygonal ferrite (α_P) was a blocky ferrite microstructure formed at a higher transformation temperature or from a low cooling rate, which allows nucleation at both

grain boundaries and in intragranular regions. Pearlite (P) is a mixture of ferrite and cementite, and these two phases can grow cooperatively at the transformation front from austenite.

Table 3.1 The features of transformation products during the austenite phase transformation [179]

Feature	α'_M	α_{lb}	α_{ub}	α_a	α_w	αA	α_i	P
Nucleation and growth reaction	Y	Y	Y	Y	Y	Y	Y	Y
Plate shape	Y	Y	Y	Y	Y	N	N	N
IPS shape change with large shear	Y	Y	Y	Y	Y	N	N	N
Lattice correspondence during growth	Y	Y	Y	Y	N	N	N	N
Co-operative growth of ferrite and cementite	N	N	N	N	N	N	N	Y
High dislocation density	Y	Y	Y	Y	X	N	N	N
Necessarily has a glissile interface	Y	Y	Y	Y	Y	N	N	N
Always has an orientation within the bain region	Y	Y	Y	Y	Y	N	N	N
Growth across austenite grain boundaries	N	N	N	N	N	Y	Y	Y
High interface mobility at low temperatures	Y	Y	Y	Y	Y	N	N	N
Reconstruction diffusion during growth	N	N	N	N	N	Y	Y	Y
Bulk distribution of substitution atoms during growth	N	N	N	N	N	X	X	X
Displacive transformation mechanism	Y	Y	Y	Y	Y	X	X	X
Reconstruction transformation mechanism	N	N	N	N	N	Y	Y	Y
Diffusionless nucleation	Y	N	N	N	N	N	N	N
Only carbon diffusion during nucleation	N	Y	Y	Y	Y	N	N	N
Reconstructive diffusion during nucleation	N	N	N	N	N	Y	Y	Y
Often nucleates intragranularly on defects	Y	N	N	Y	N	N	Y	N
Diffusionless growth	Y	Y	Y	Y	N	N	N	N
Local equilibrium at interface during growth	N	N	N	N	N	X	X	X
Local paraequibrium at interface during growth	N	N	N	N	Y	X	X	N
Diffusion of carbon during transformation	N	N	N	N	Y	Y	Y	Y
Carbon diffusion controlled growth	N	N	N	N	Y	X	X	X
Incomplete reaction phenomenon	N	Y	Y	Y	N	N	N	N

Note: Martensite α'M, lower bainite α_{lb}, upper bainite α_{ub}, acicular ferrite α_a, Widemanstätten ferrite α_w, allotriomorphic ferrite α_A, idiomorphic ferrite α_i, peralite P; Y consistent, N inconsistent, X sometime consistent.

Both allotriomorphic (α_A) and idiomorphic ferrite (α_i) are a kind of reconstructive transformation product. Significant diffusion occurred during the growth process. Allotriomorphic ferrite is commonly nucleated at austenite grain boundaries; its shape does not reflect its internal crystalline symmetry. On the other hand, idiomorphic ferrite

nucleates within the grain and can reflect its internal symmetry. Both of these phases are referred as a polygonal ferrite (α_P) when grain boundaries are not apparent.

The formation of the bainite phase occurs without the solute atom diffusion, while carbon can diffuse short distance during the transformation. At higher temperatures, carbon can partition into retained austenite and cementite formed between the ferrite laths. This is typical of the formation of upper bainite (α_{ub}). At lower temperatures, the carbon diffusion rate is limited so carbon has more chance to precipitate within the ferrite plates. This is how lower bainite (α_{lb}) formed.

Widemanstätten ferrite (α_w) is a needle shaped ferrite whose growth is limited by the diffusion of carbon ahead of the α_w/γ interface. In this case, solute atoms do not diffuse like bainite. Acicular ferrite (α_a) is plate ferrite nucleated on nonmetallic inclusions within the austenite grains. It common has the same transformation mechanism as bainite.

The martensite transformation is commonly defined as a diffusionless transformation where the parent lattice is shifted into that of the products, which commonly occur when the austenite is cooled below the M_s temperature on a TTT diagram.

Due to poor understanding, the same phase may have a different definition and a different symbol in the published literatures. The phases and symbols of this thesis follow the above definitions. The characterization of different phases is also given in the Table 3.1.

3.2 Phase transitions in T91 steels

3.2.1 Additional nomenclature for T91

There are some nomenclatures in this study that do not belong to the common catalog. T91 is an F/M steel, in which the tempering of martensite is crucial. The martensite can be tempered to form tempered martensite (α'_T). If fully tempered, it will contain mainly a ferrite phase with carbides. If not fully tempered, it can be a mixture of ferrite and martensite. There is another kind of tempered martensite, called auto-tempered martensite (α'_{AT}), which the first formed martensite tempered during the remainder of quenching. Because no upper bainite is identified, the lower bainite observed here is not distinguished and named α_B. The retained austenite is named γ. Other symbols are defined/discussed in the Table.3.2.

Table 3.2 Microstructural symbols and nomenclature used for different phases in this thesis

symbols	**nomenclature**
α_P	polygonal ferrite
α_A	allotriomorphic ferrite/grain boundary ferrite
α'_M	martensite
α'_T	tempered martensite
α'_{AT}	auto-tempered martensite
α_B	bainitic ferrite
M/A	martensite/austenite constituent
γ	retained austenite
PAGB	prior austenite grain boundary
ε-C	epsilon carbide
θ	cementite

3.2.2 Water quenching of T91 steels

We used the OM and SEM images (Fig.3.1 and Fig.3.2) simultaneously to interpret the microstructure of WQ T91 steel because these two techniques were complementary. The interpretation of SEM images was based on the chemical properties

of different phases and their morphologies. The ferrite phase is etched away thus appears to be “deeper” in the SEM images. The martensite is less attacked by the etchant and thus appears to be “higher” in the SEM images. The AA T91 steel has a fully tempered martensitic lath structure (α'_T) with small regions of other phases (shown in Fig.3.1a). These phases are often retained austenite or martensite (M/A constituent). Prior austenite grain boundaries (PAGB) are often decorated by “white” carbides particles (shown in Fig.3.2a). Lath boundaries with embedded carbides were also observed. Water quenching form 800°C gives a fine structure as Fig.3.1b. This fine structure was a mixture of grain boundary ferrite (α_A) and martensite (α'_M), as confirmed by the SEM images of Fig.3.2b. Some martensite laths within prior austenite grainsare also etched away. This phase was interpreted as auto-tempered martensite (α'_{AT}), because of its resemblance of ferrite phase. Water quenching from 900°C and 1000°C give a fully γ-transformed structure including martensite ($\alpha'_M + \alpha'_{AT}$) and a small percentage of polygonal ferrite (α_P) as shown in Fig.3.1c-d and Fig.3.2c. α_P exhibits as a white clean grain under OM. No grain boundary ferrite (α_A) was observed in the 900WQ specimen. Thus, the $\alpha \rightarrow \gamma$ phase transformation temperature is inferred to be somewhere between 800-900°C in the present T91 steel. Although there is no carbide decoration, PAGBs can still be observed in the WQ specimens (marked in Fig.3.2c). Significant coarsening of austenite grains occurred after heat treatment at 1100°C (Fig.3.1e-f). The coarse austenite grains lead to a higher aspect ratio of martensitic laths. Bainitic ferrite is seen within the prior austenite grains in the 1200WQ specimen, which is commonly thicker

than the martensite laths. Auto-tempered martensite is observed in all the WQ specimens.

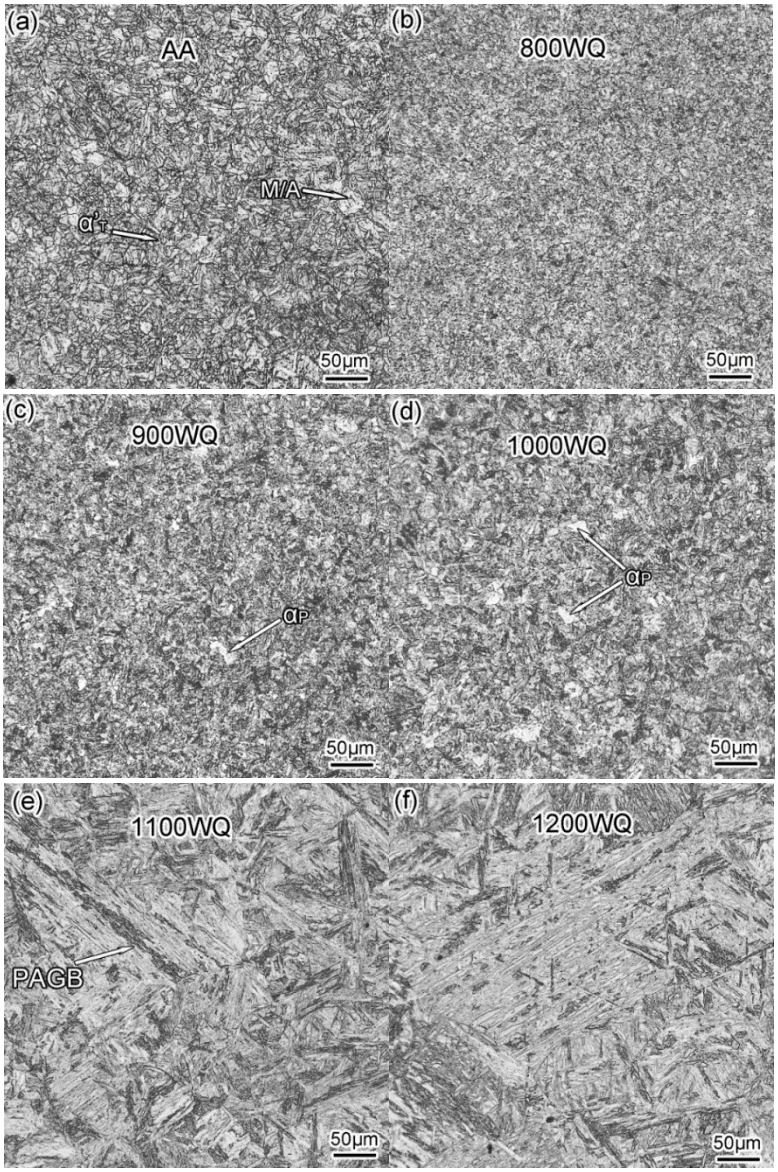

Figure 3.1 Typical optical micrographs show the microstructure of as-annealed (AA) and water quenched (WQ) T91 steel. (a) The AA material is a predominantly ferrite with a dispersed equiaxed M/A constituent. (b) Heat treatment at 800°C for 1h followed by WQ (800WQ) led to a mixture of martensite (α'_M+ α'_{AT}) and GB ferrite (α_A). Heat treatment via (c) 900WQ and (d) 1000WQ resulted in a mixture of martensite (α'_M+ α'_{AT}) and polygonal ferrite (α_P), identified as clean grains by arrows. (e) 1100WQ and (f) 1200WQ yielded primarily martensite (α'_M+ α'_{AT}). A prior austenite grain boundary (PAGB) was identified in the 1100WQ specimen.

Fig.3.3 shows the prior austenite grain size of the WQ T91 steel. AA T91 has a heat treatment history of austenization at 1040°C, which yields a slightly larger grain size than 1000WQ T91. The grain size increases from ~ 13 μm to ~ 150 μm, about an order of magnitude, above 1100WQ. No delta ferrite was noticed during the WQ process till 1200 °C as shown in Fig.3.4 in the lower magnification of OM.

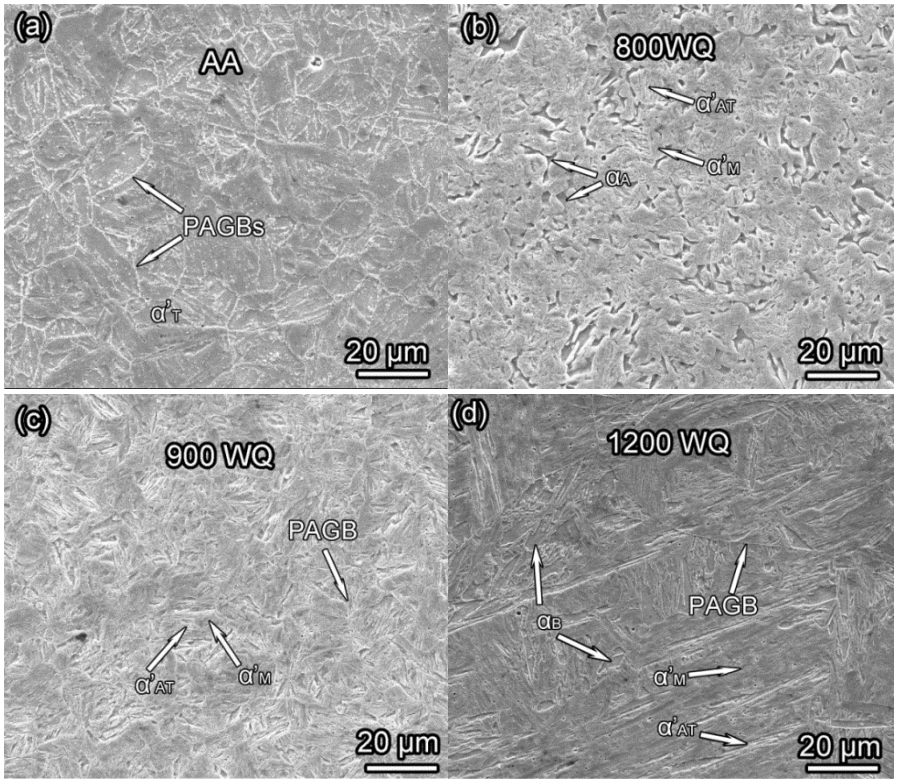

Figure 3.2 Representative SEM images of AA and WQ T91 steel. (a) The PAGBs decorated by positioned carbides (white lines) are observed in the as-annealed (AA) condition. (b) Three phases are identified in the 800WQ sample. The darker phase is allotriomorphic ferrite (α_A)or grain boundary ferrite due to the fact that the shape of it cannot represent its internal crystalline symmetry. The auto-tempered martensite (α'_{AT}) shows the lath feature and etched because it has partially ferrite properties. The un-etched phase is martensite phase (α'_M). (c) No allotriomorphic ferrite was observed in 900WQ T91 material. (d) Except martensite (α'_M) and auto-tempered martensite (α'_{AT}), bainitic ferrite (α_B) was also observed in the 1200WQ material.

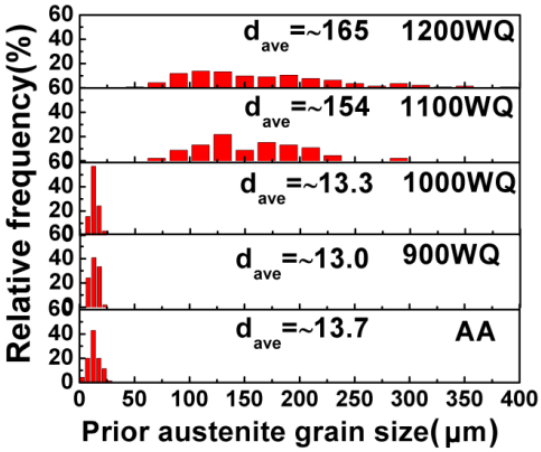

Figure 3.3 Grain size distribution of prior austenite grains at various WQ conditions show that, austenite grains coarsen significantly at 1100°C or higher.

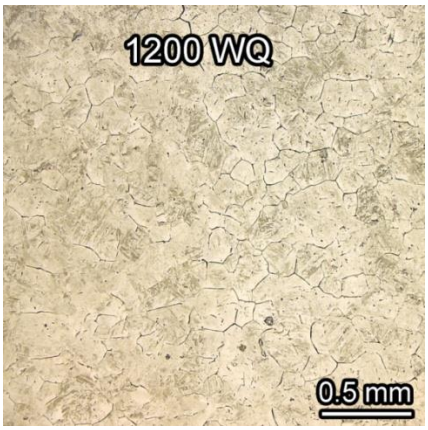

Figure 3.4 The PAGB was attacked by the etching solution. No delta ferrite was observed at a large scale.

Table 3.3 Microstructural features of T91 steel following austenitizing for 1 h and water quenching (WQ)

Temperature before WQ (°C)	**Initial phase**	**Phases after WQ**	**Grain size of γ(μm)**
800	γ + undissolved α + undissolved carbides	α'_M+ α'_{AT} +α_A +carbides	N/A
900	γ	α_P+α'_M+ α'_{AT}	13
1000	γ	α_P+α'_M+ α'_{AT}	13.3
1100	coarsen grained γ	α'_M+ α'_{AT}	154
1200	coarsen grained γ	α'_M+ α'_{AT}+α_B	165

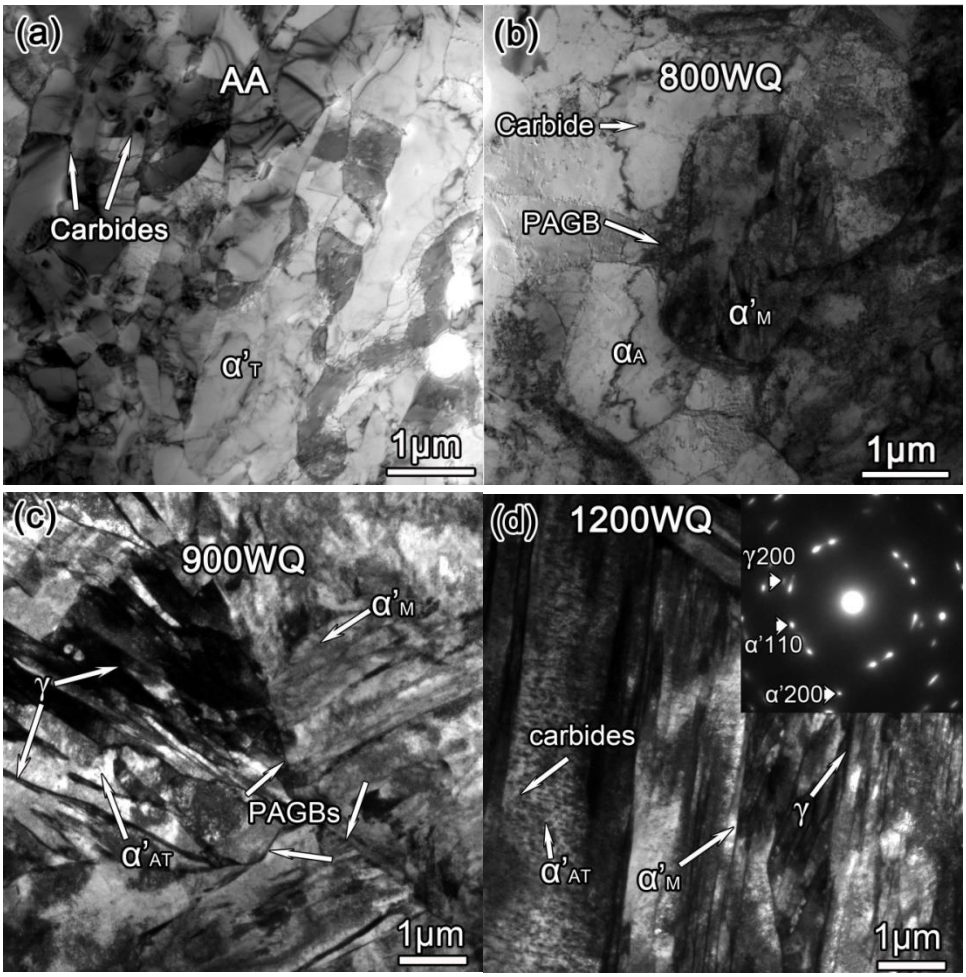

Figure 3.5 TEM micrographs of AA and WQ T91 steel. (a) fully tempered AA T91 steel with predominantly the ferrite phase and carbide precipitate. (b) 800WQ exhibits a duplex structure (α'_M+ α_A). The α_A phase is marked following the contours of PAGBs. (c) Triple junctions of PAGBs in 900WQ specimen with a mixture of α'_M and α'_{AT}. (d) Carbides are observed in the martensitic lath structure in the 1200WQ specimen. Auto-tempering occurred during the quenching process. The retained γ phase is a thin layer located between two martensitic laths. The inserted selected area diffraction (SAD) pattern reveals the coexistence of martensite (α'_M + α'_{AT}) and the γ phase.

Fig.3.5 shows representative TEM micrographs of WQ T91 steel. The AA specimen in Fig.3.5a shows partially recrystallized tempered martensite with carbides at the grain boundaries. A prior austenite grain is surrounded by adjacent grain boundary ferrite in the 800WQ specimen (Fig.3.5b). Undissolved carbides are observed within the grain boundary ferrite. A triple junction of prior austenite grains in 900WQ T91 is

shown in Fig.3.5c. Retained γ is identified as the thin layer between martensite laths with black contrast in Fig.3.5c. Martensite laths ($\alpha'_M+\alpha'_{AT}$) with a large aspect ratio dominate the microstructure of the 1200WQ T91 as shown in Fig.3.5d. Carbides were trapped within the martensite laths. Fig.3.6 shows an overall martensite microstructure ($\alpha'_M+\alpha'_{AT}$) within a prior austenite grain. Auto-tempered martensite differs from martensite by the intralath carbides. Thicker martensite laths are susceptible to auto-tempering because they are commonly formed at higher temperatures. All the microstructure features observed in this study is listed in Table 3.3.

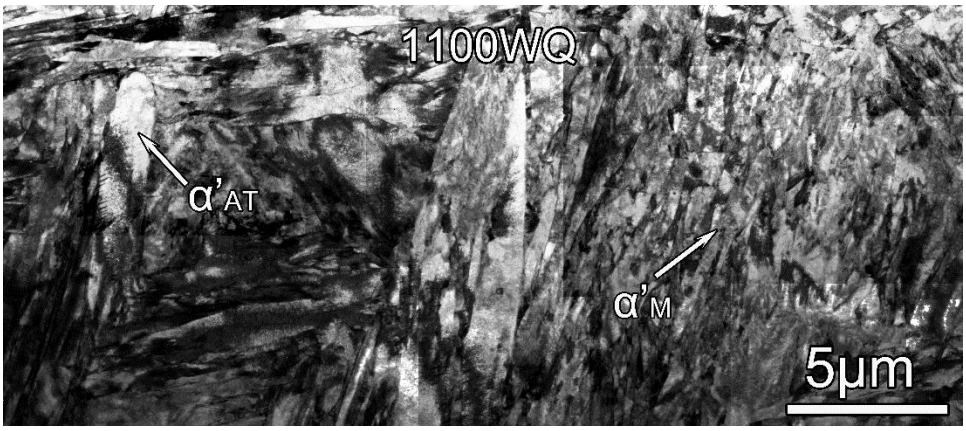

Figure 3.6 Panoramic view of the microstructure of the 1100WQ specimen shows a mixture of martensite (α'_M) and auto-tempered martensite (α'_{AT}) (with carbide precipitates inside the lath).

3.3 ε-carbides in the water quenched T91

ε-carbides that have never been observed in T91, were observed in this study. Both martensite and carbides were observed within a bainite ferrite matrix in the 1200WQ T91 steel (Fig.3.7). High resolution TEM (HRTEM) reveals that a substantial amount of strain was built up around the needle shape carbides (Fig.3.7b). The carbides

were confirmed to be ε-carbide by fast Fourier transformation (FFT) analysis. The classic Jack orientation relationship between carbide and martensite prevails [180], where $\alpha[1\bar{1}1]//\varepsilon\text{-C}\ [1\bar{2}10]$, $\alpha(011)//\varepsilon\text{-C}\ (000\bar{2})$. This observation was frequently observed within the auto-tempered martensite. Fig.3.8a shows the precipitate phase is a black needle at the TB condition. The contrast was reversed in the Fig.3.8b, where the edge of the precipitates shows a white line. High resolution TEM images reveal that the precipitates are ε-carbide and cementite. Both of these share the same precipitation plane with different directions. The cementite has an orientation relationship $\alpha[011]//\theta[010]$, and $\alpha\ (\bar{2}\bar{1}1)//\theta\ (200)$ with the matrix.

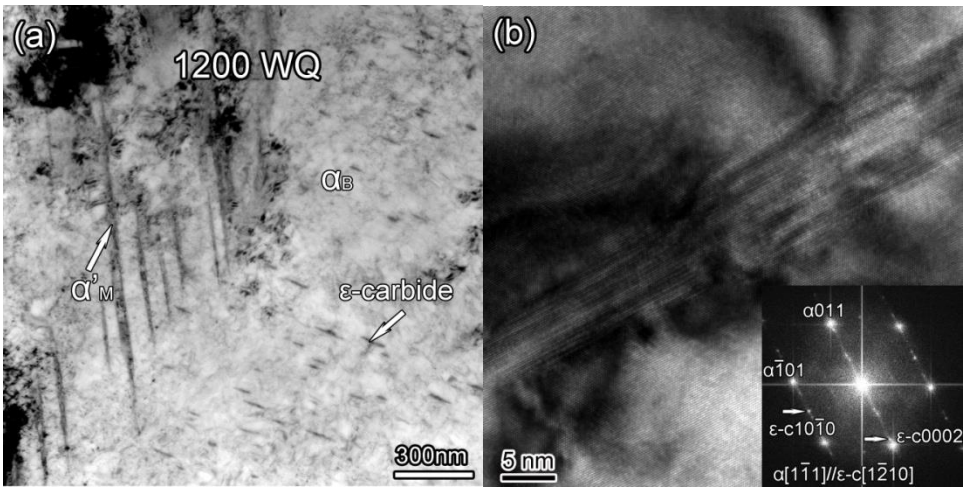

Figure 3.7 (a) TEM micrograph shows that the 1200WQ specimen contained precipitates, including martensite and epsilon carbides, with bainite ferrite. (b) HRTEM micrograph of needle shaped ε-carbide with fast Fourier transformation (FFT) inserted at the bottom right corner.

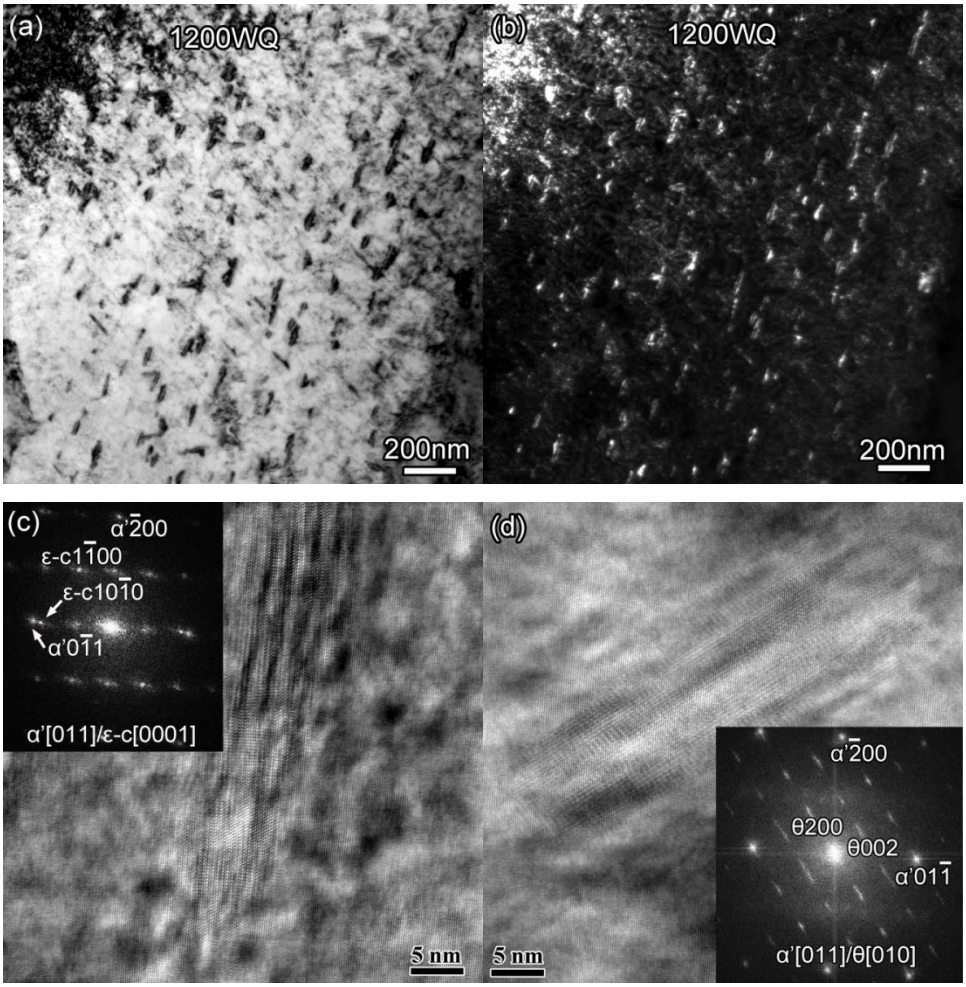

Figure 3.8 ε-carbide and cementite in WQ T91 steels (a) Bright field TEM images at the near two beam condition.(b) corresponding weak beam dark field images (c) HRTEM of ε-carbide (d) HRTEM of cementite

3.4 Summary

In this chapter, the basic products from the γ→α (austenite→ferrite) transformation are introduced. Bainitic ferrite, which is unlikely to form in T91 steel, was observed. ε-C was first observed in T91 steel. The orientation relationship of ε-C and the matrix follow the classic orientation relationship. Most of the WQ T91 examined

contains auto-tempered martensite. The austenite grain size coarsened significantly above 1100°C.

CHAPTER IV

ECAE ENABLED TMT PROCESSING OF T91 STEEL*

In this chapter, the microstructure and mechanical properties of ECAE processed T91 is discussed. The ECAE is performed on several T91 bars with different heat treatment history, such as heavily tempered martensite and slightly tempered martensite at various processing temperatures. An ausforming process is also performed, for which the T91 is deformed at 1000°C in the austenite phase zone with a high strain rate, then water quenched.

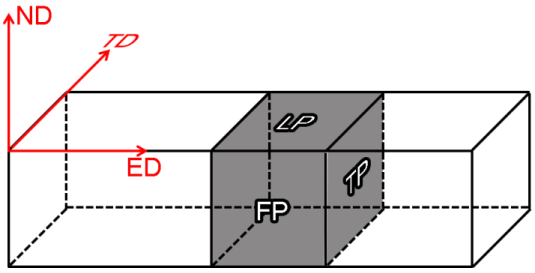

Figure 4.1 Direction of extruded billet. These directions and planes are denoted as: ND, normal direction; TD, transverse direction; ED, extrusion direction; LP, longitude plane; FP, flow plane; TP, transverse plane.

4.1 ECAE processed heavily tempered T91 steel

4.1.1 Microstructure of ECAE processed heavily tempered T91 steel

The heavily tempered martensitic T91 steel is predominately ferrite with the tempered lath structure, where the lath boundaries and PAGB are decorated by carbides.

*Partially reprint with the permission from "Enhancement of strength and ductility in ultrafine-grained T91 steel through thermomechanical treatments" by M. Song *et al*, 2013. Journal of Materials Science, 48, 7360-7373, Copyright [2013] by Springer.

The various direction definitions of the extruded billet are denoted in Fig.4.1. The flow plane (FP) often carries more information. The transverse plane (TP) usually presents the smallest grain size. The microstructure evolution on these three planes are characterized by OP, SEM, TEM and STEM.

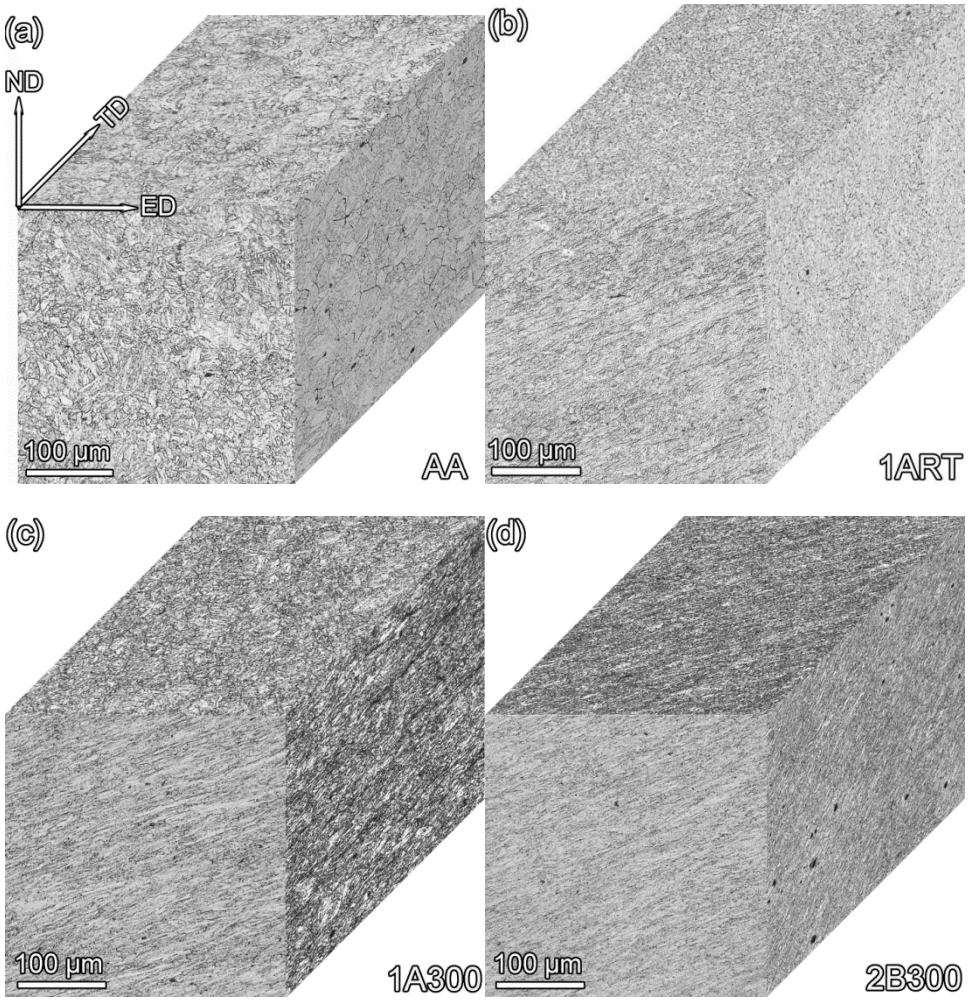

Figure 4.2 Optical images that show the results of plastic flow of the grain structures subjected to low temperature extrusion (a) AA, typical tempered martensite structure in all three planes; no deformation grain structure was observed before extrusion. (b) 1ART, clear shear structure is observed within FP, no significant shear structures were observed on TP or LP. (c) 1A300, band structure was noticed FP. (d) 2B300, shear structure can be observed in all three directions. All specimens are etched.

To investigate the influence of processing temperature on grain refinement, we selected two groups of processing conditions. In the first group, the extrusion temperature was less than the common recrystallization temperature of T91 steel, ~ 500°C, and this process is thus named "cold-ECAE". The starting material for the cold-ECAE process was the AA materials, which is fully ferritic. In the second group, "hot-ECAE", the specimens were processed at temperatures greater than 500°C. As pre-extrusion annealing (1h) was performed on all hot-ECAE specimens at temperatures sufficient to achieve a fully tempered microstructure, AR materials were used for these experiments. Direct plastic flow was observed for cold-ECAE as shown in Fig 4.2. The AA specimens shown in Fig.4.2a are of a typical tempered martensite microstructure without any deformation. Banded structure was observed after a single extrusion at RT (1ART) on the FP as shown in Fig.4.2b. The shear feature is not significant in the other two planes LP and TP. For single shear at 300°C (1A300), some white bands are observed with the shear structure on the FP. Further extrusion following route B at 300 °C (2B300) gives a banded structure on all three planes. A similar white banded structure is observed on all three planes, but with less band thickness.

Hot-ECAE extrusions are done with the AR material by preheating to target temperature for 1hour and then extrusion. The AR T91 is also tempered martensite similar to the AA structure as shown in Fig.4.3a. A thicker band was developed during a single pass of this materials at 625°C (1A625). Two passes following route B at the same temperature (2B625) gives a band structure in all three directions. Three passes at

700°C (3Bc700) yields a recrystallization structure. Recrystallized grains with a white contrast can be observed in Fig.4.3d.

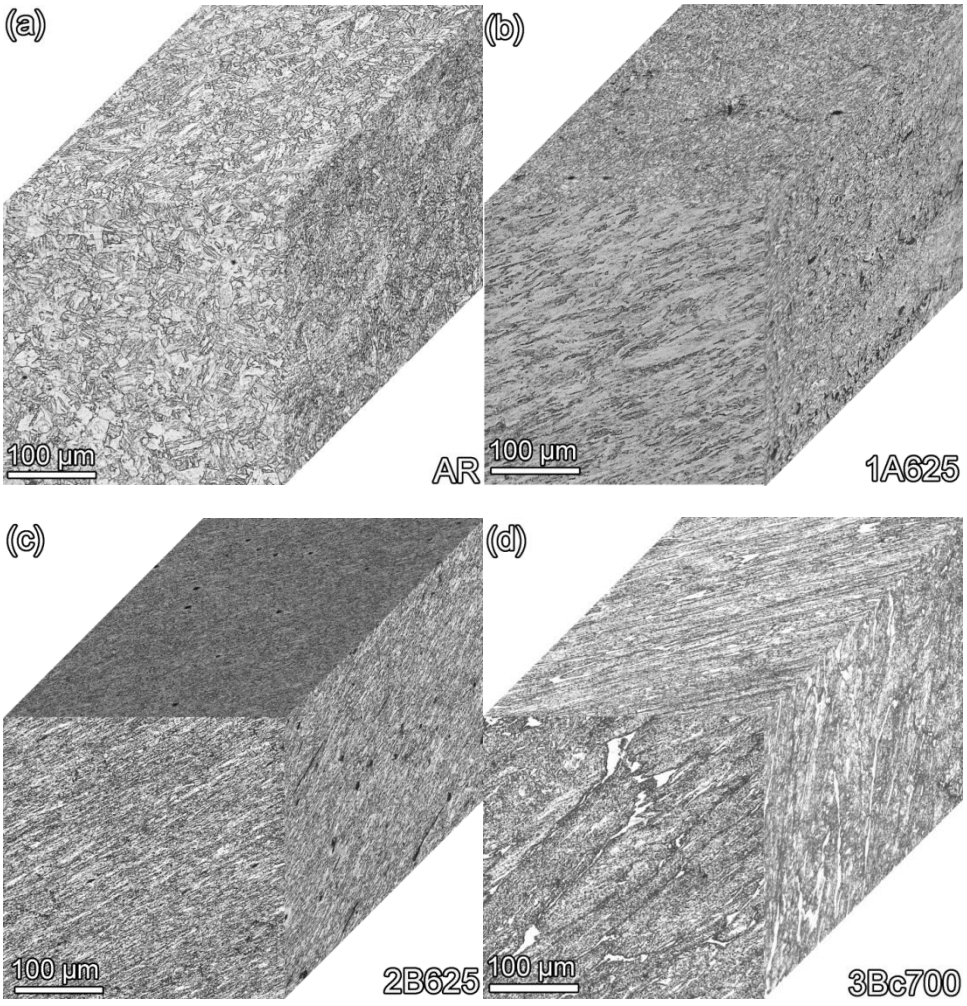

Figure 4.3 Optical images showing plastic flow of grain structures subjected to elevated temperature extrusion. (a) AR, heavy tempered martensite structure on all three directions. (b) 1A625, clear shear structure is observed on the FP. (c) 2B625,a shear structure is observed on all three directions. (d) 3Bc700, recrystallization grains are observed on all three directions. (a-c) Specimens are etched. Specimen 3Bc700 was observed directly after electro polishing.

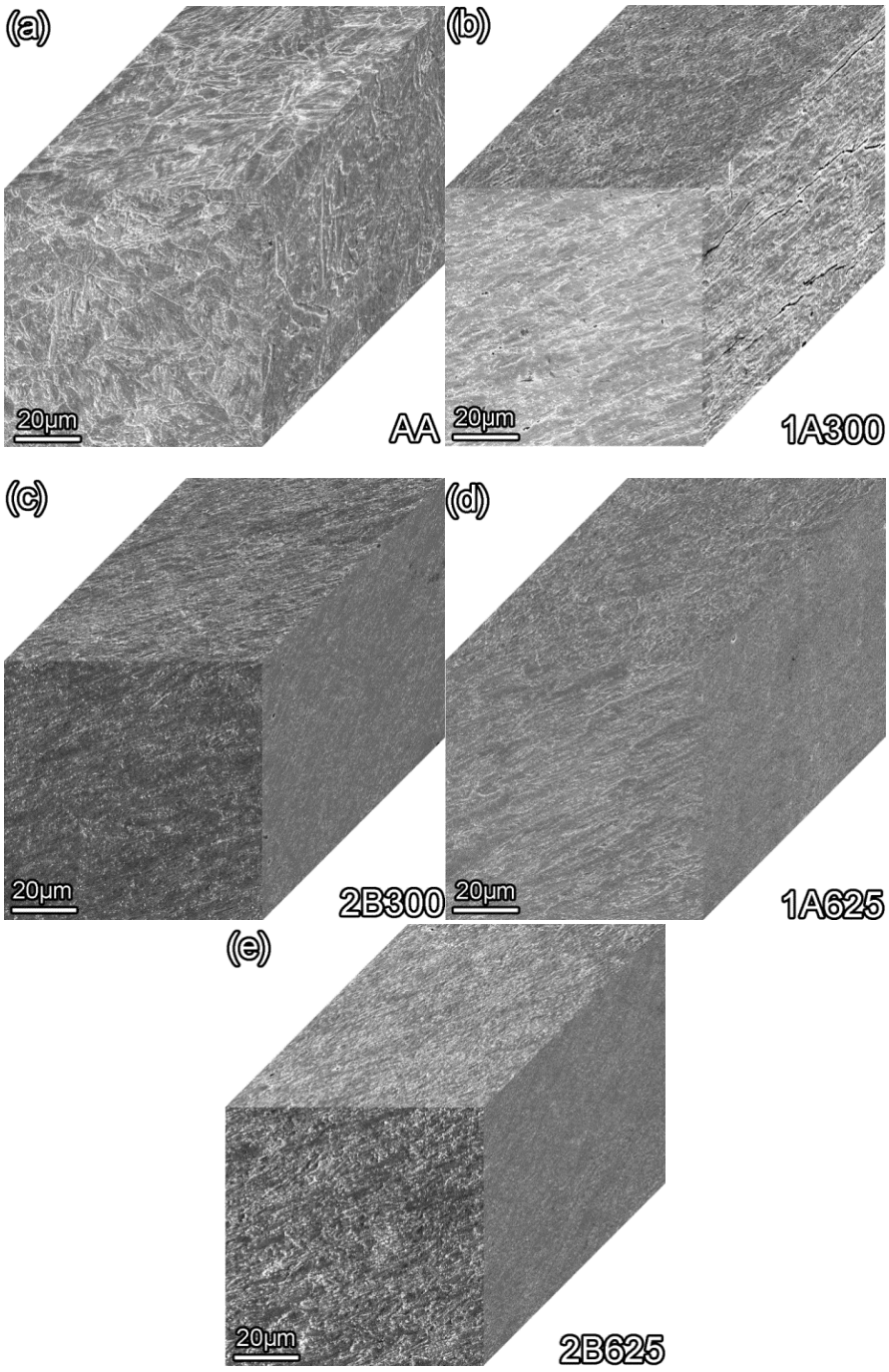

Figure 4.4 SEM images showing redistribution of carbides and deformation of the PAGBs by ECAE. (a) AA, PAGB is clearly observed on all the three planes; (b) 1A300, carbides decorated at PAGB are redistributed and PAGB broken into pieces; (c) 2B300, PAGB was further deformed; (d)1A625, (e)2B625, carbides seem smaller after the high temperature refining process.

Fig.4.4 shows the breaking of PAGBs by ECAE. The carbides at the PAGBs were redistributed uniformly within the material after ECAE. For the AA specimens, it is clearly observed that the PAGBs are decorated by white particles. Some pattern of carbides can be still found in the single pass extrusion as shown in Fig 4.4b and d, because the PAGBs are not fully broken up. Additional passes redistribute the carbides throughout the material. Hot-ECAE seems to be more effective for redistribution of carbides compared to cold ECAE.

The grain structure and carbide particles evolution were also observed at a higher magnification using TEM (Fig.4.5 and 4.7) and STEM (Fig 4.6). The ferrite grain size of AA is ~ 2.8 μm measured on the TP. Large carbides are usually at PAGBs. These carbides are presumably $(Fe, Cr)_{23}C_6$ and Nb (C, N)[181, 182]. For the 1A300 specimen (Fig4.5b, 4.6b, and 4.7d), the grain size was effectively refined to below 1 μm as observed on the TP. The FP shows an elongated lamellar structure (ELS) with a thickness below 1μm. Meanwhile, the density of intragranular dislocations is not as high as that in the case of 1ART (Fig.4.7c). After an additional extrusion via route B at 300°C (2B300), the average grain size was further reduced to about 0.15 μm as observed on the TP. The ELS thickness was further reduced to below 200 nm. The density of intragranular dislocations also increased (Fig.4.5c, 4.6c, 4.7e) compared with the 1A300 specimen. Intergranular carbides are frequently observed in the cold-ECAEed samples as examined using STEM. The carbides were redistributed following the deformation of PAGBs but the size was not reduced.

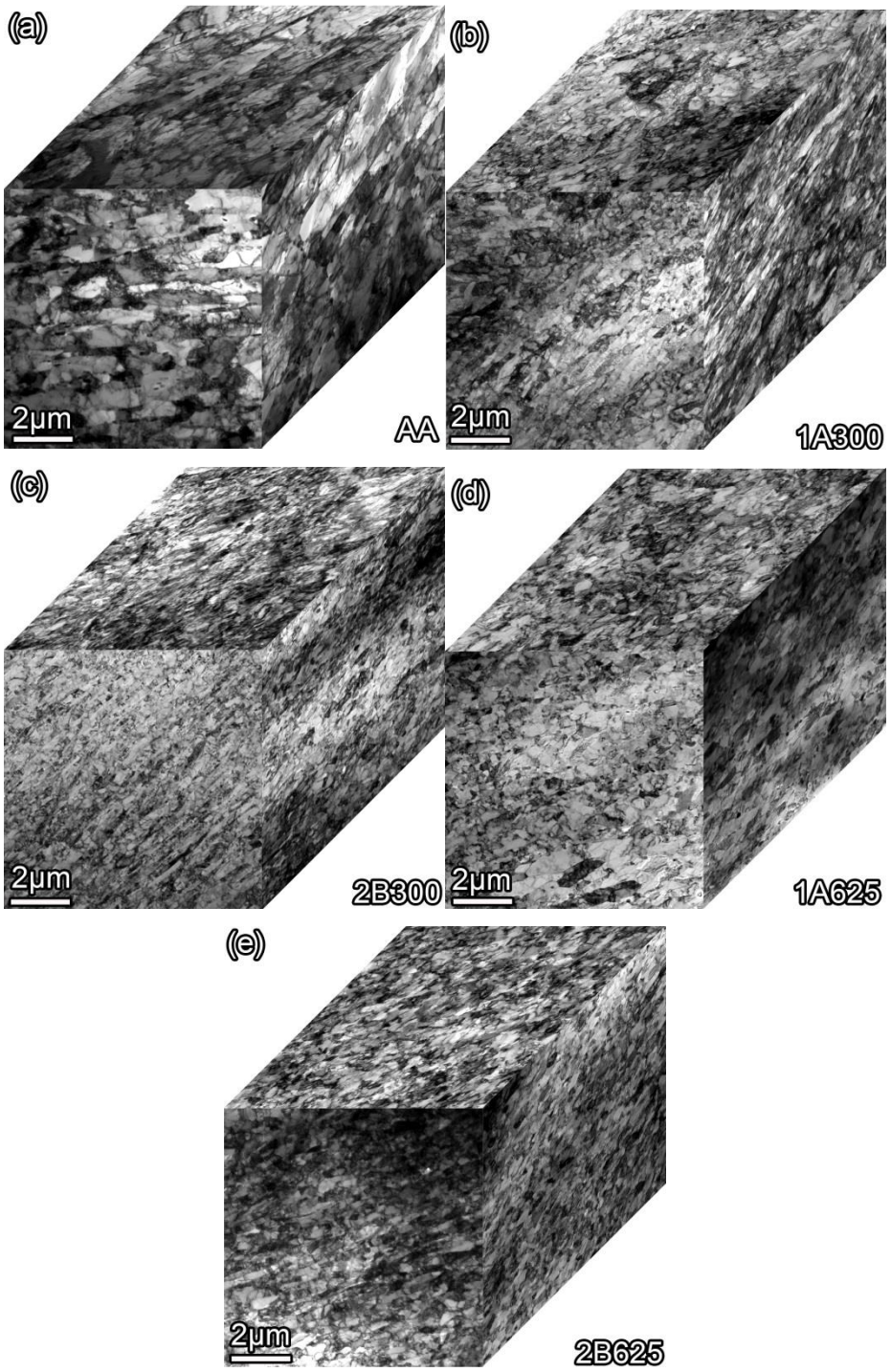

Figure 4.5 TEM images showing significant grain refinement by ECAE. (a) AA, typical tempered martensite lath structure on all three planes; (b) 1A300, martensite laths can be refined after single pass deformation; the deformed structure shows an elongated lamella structure. (c) 2B300, further refinement occurs during extrusion on all three planes; (d)1A625, grain refinement occurs after a single pass and the refined grains show lower dislocation density; (e)2B625, two passes at elevated temperature can also refine the grains on all three planes.

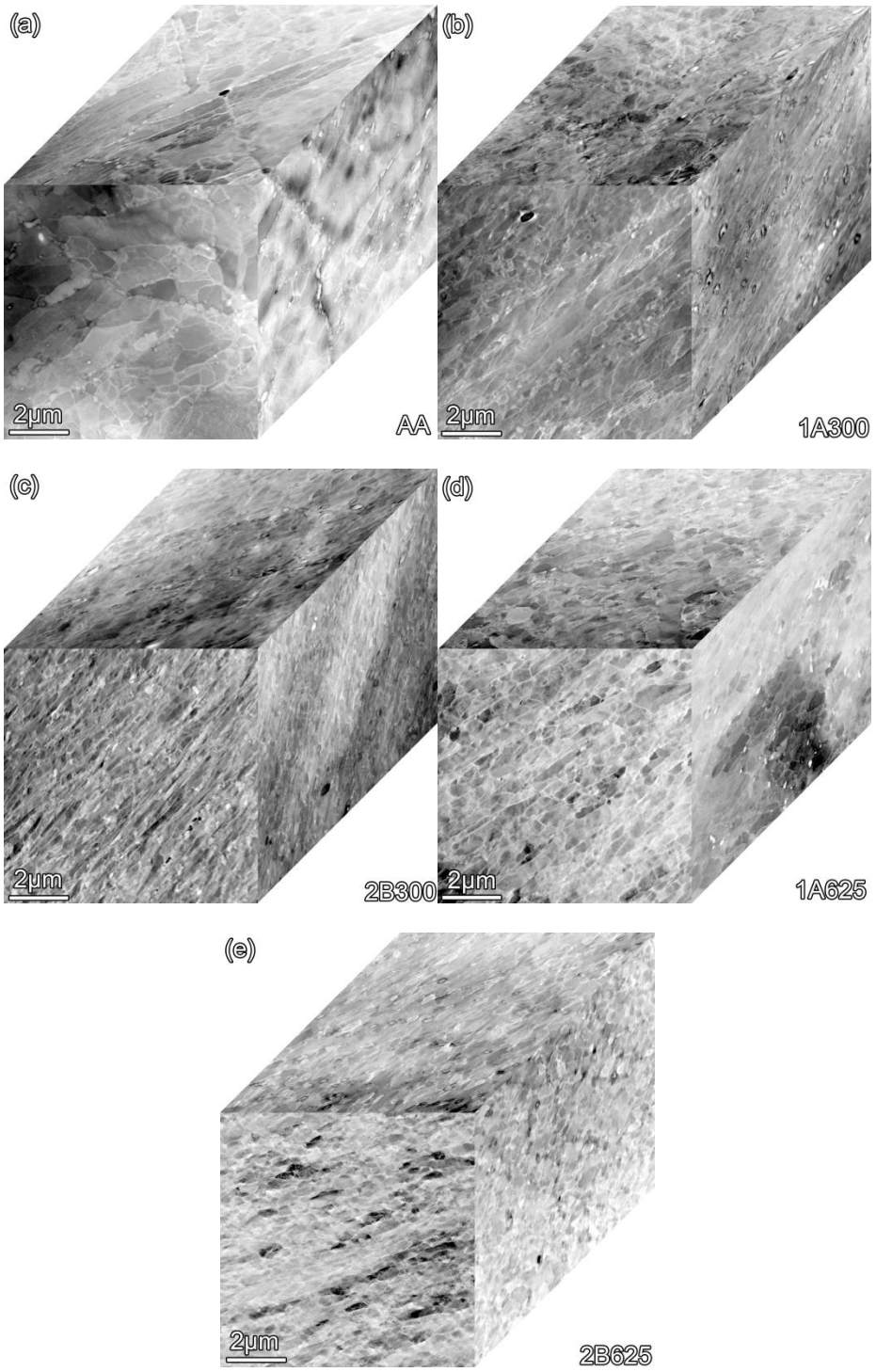

Figure 4.6 TEM images showing redistribution of carbides and deformation of the PAGBs by ECAE.(a) AA, PAGB is clear observed. (b) 1A300, grains are refined and carbides are redistributed; (c) 2B300, grains are further refined, and PAGBs are invisible;(d) 1A625 and (e) 2B625, relatively small sized carbides are observed after ECAE at elevated temperature.

In comparison to cold-ECAE, hot-ECAE processing (at temperatures greater than 500°C) leads to a different microstructure. The 1A625 (Fig.4.5d and 4.6d) material shows moderate refinement of grain size compared to the 1A300. The ELS is larger with a smaller aspect ratio compared to the 1A300 material. The 2B625 specimen (Fig.4.5e, 4.6e and 4.7f) has an average grain size of 0.31 μm observed on the TP, although the same amount of strain was introduced here as for the 2B300 case. The ELS shows a smaller aspect ratio with a more equivalent grain boundary microstructure. Also, the density of intragranular dislocations is much lower than the cold-ECAEed specimen. Abundant fine intragranular carbide particles (less than 100 nm in diameter) are observed in t hot-ECAE processed T91 steel. The prior austenite boundaries are completely decomposed for this processing condition. Compared to the 2B625 specimen, extrusion via 3Bc700 does not refine the average grain size further, and more intragranular carbides are observed for this processing condition (Fig.4.7g).The carbide is confirmed to be (Cr, Fe)23C6 by the STEM line scanning as shown in Fig.4.8. The white particles are Cr enriched M23C6 carbide.

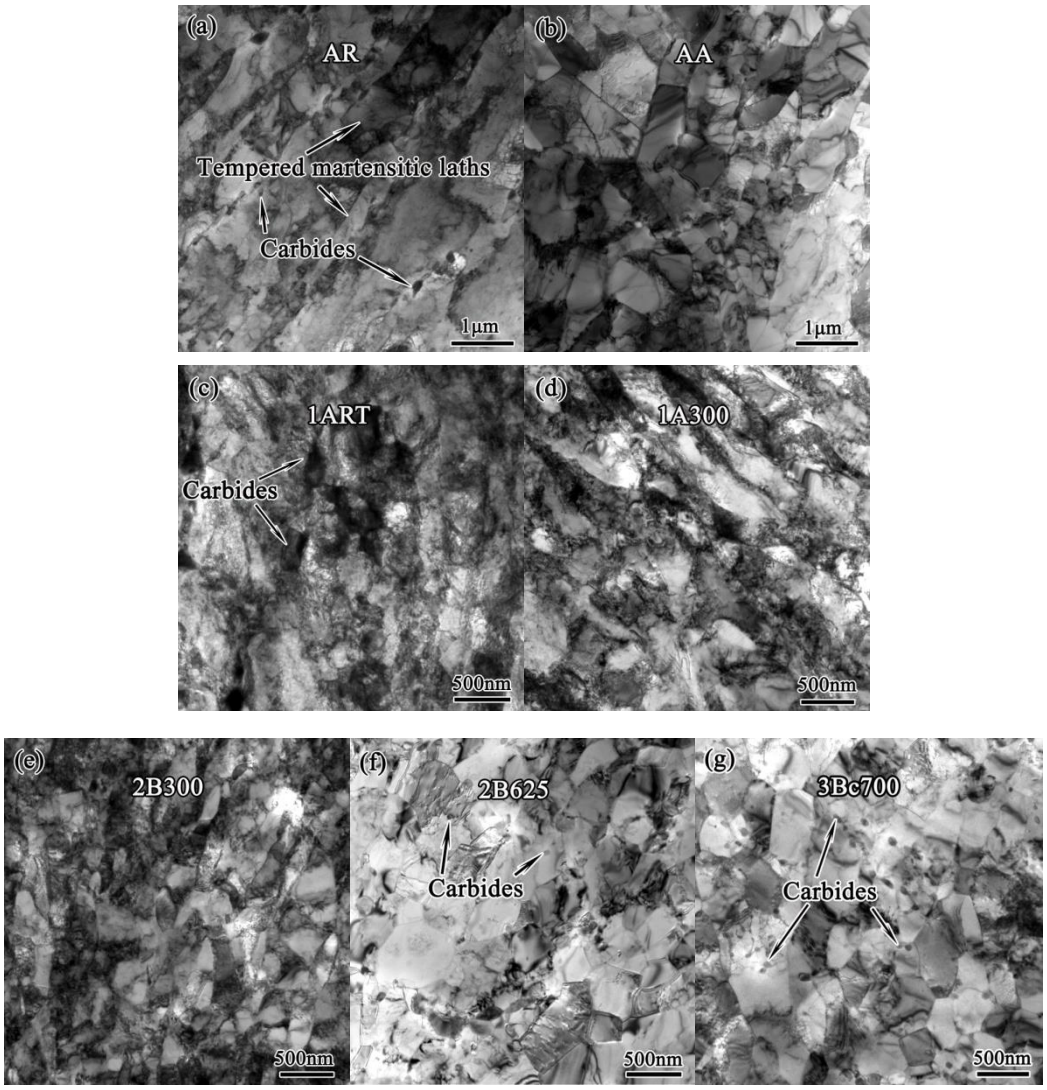

Figure 4.7 Bright field TEM micrographs showing the microstructure of the initial and ECAE processed T91 steel. (a) As-received (AR) material has fragments of the original martensitic laths within a ferritic matrix with carbides. (b) As-annealed material (AA) has a recrystallized microstructure of AR specimen with an average grain size of 0.63 μm. (c) After single-pass ECAE at room temperature (1ART), a high density of dislocations is observed. (d) After ECAE at 300°C (1A300), the dislocation density increases, and the average grain size is ~ 0.27 μm. (e) Two pass ECAE following route B at 300°C (2B300) leads to a reduction of the average grain size to 0.15 μm. (f) After two passes of ECAE following route B at 625°C (2B625), the average grain size is refined to 0.31 μm and the dislocation density inside grains is lower than that processed at lower temperatures. (g) Three passes of ECAE at 700°C (3Bc700) yields an average grain size ~0.30 μm and a relatively low dislocation density. Numerous carbides are observed as well for this processing routes.

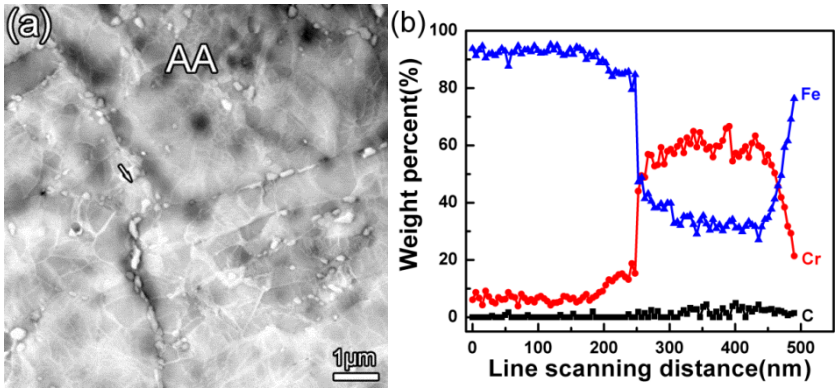

Figure 4.8 (a) STEM images of carbides in the AA specimen and (b) corresponding EDS line scan profile. The white dots were founded to be Cr enriched caribide.

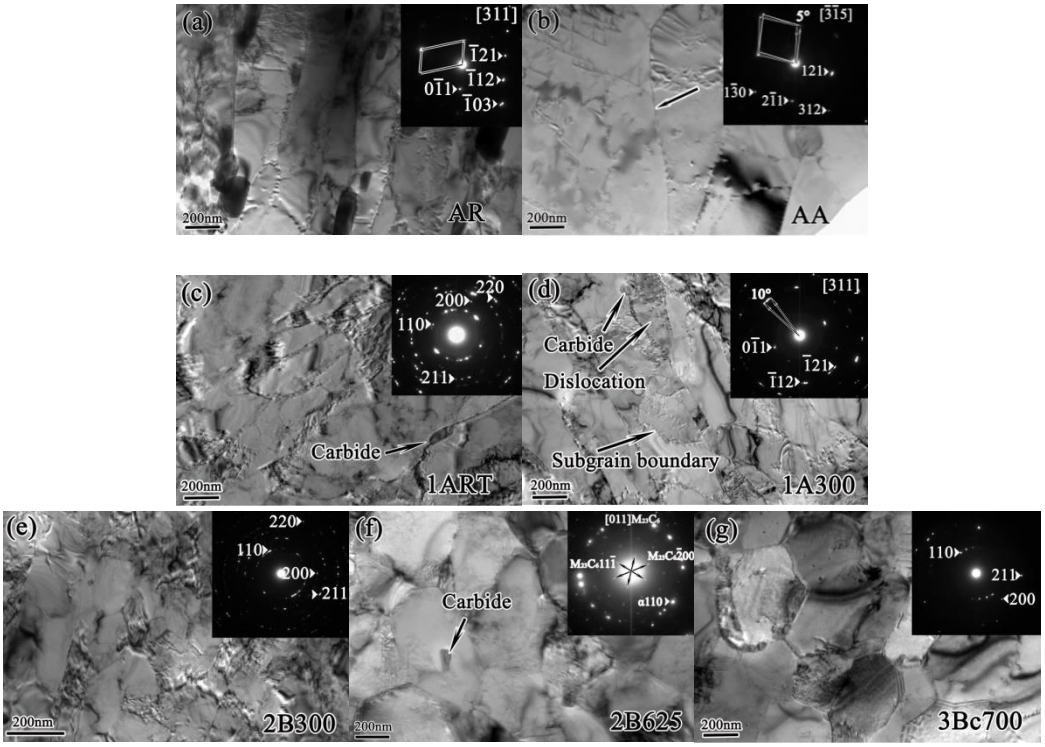

Figure 4.9 Typical bright field TEM micrographs with SAD patterns showing grain boundary (GB) characteristics of the initial and ECAEed T91 steel. (a) The AR material typically had low angle GBs as shown by the inserted SAD pattern examined along the [311] zone axis. (b)A typical example of a 5° GB (marked by arrow) studied along $[\bar{1}\bar{3}5]$ zone axis in AA material. (c) In the 1ART specimen, abundant high angle GBS are seen. (d) For the 1A300 specimen, a majority of the GB angles are below 10°. (e, f) In the 2B300 and 2B625 specimens, high angle GBs are frequently detected. (g) The 3Bc700 specimen has predominately high angle GBs.

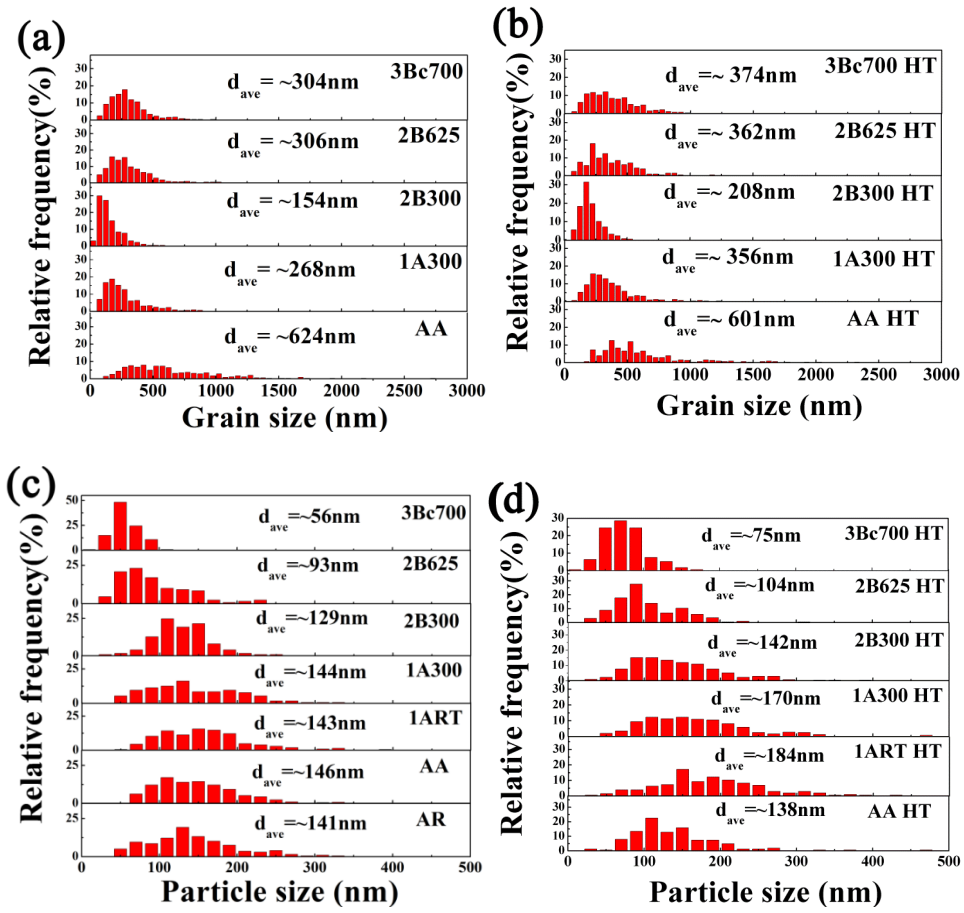

Figure 4.10 Grain and carbide size distributions in T91 alloys following different TMT. (a) Grain refinement occurred in all ECAE processed specimens. The 2B300 specimen has the smallest average grain size, ~ 150 nm. (b) After heat treatment (500°C/10h, denoted as HT), grains coarsened slightly in the ECAE processed samples. (c) The 3Bc700 specimen has a large number of fine carbides with an average diameter of ~ 50nm. No significant refinement of carbides was observed in Cold-ECAE processed T91. (d) After heat treatment, most carbides coarsened in the ECAE processed samples. But the average carbide dimension remains less than 100nm in the 3Bc700 specimen.

4.1.2 Refining effects and thermal stability

The evolution of grain boundary (GB) characteristics (primarily misorientation angle of GBs) is recorded in Fig.4.9. Both the AA and AR specimens show predominately low angle GBs as indicated by the inserted SAD patterns in Figs.4.9a-b. The average GB angle increased after 1A300, but is still within the range of low angle GB as shown in Fig.4.9d. Meanwhile, 1ART resulted in high angle GBs according to the

SAD in Fig.4.9c. High angle GBs were frequently observed after two or more passes, as shown in Figs.4.9e-g. In addition, a typical carbide particle in the 2B625 specimen is seen along its [011]zone axis as shown by the inserted selected area diffraction pattern (SAD) in Fig.4.9f. This carbide particle is an FCC type of $M_{23}C_6$ (M=Fe, Cr, Mo) with a lattice parameter of ~1.06 nm.

Statistical analyses of the microstructures were performed to determine the size distribution of hundreds of grains and carbide precipitates by using the linear intercept method. During cold-ECAE, the maximum grain size (as shown in Fig.4.10a) reduces from ~2.7 μm (AA alloy) to less than 1 μm via route 1A300, and is refined further via 2B300 down to 0.6 μm with primarily smaller grains. Hot-ECAE processing is less effective to refine the average grain size. However, in general, the average grain size of all ECAEed material is ~150- 300 nm, corresponding 25 -50 % of that of the AA T91 alloy. Post-extrusion annealing leads to grain coarsening in all the ECAE processed samples (Fig.4.10b). The 1A300 specimen coarsened more significantly among all investigated specimens. The evolution of carbides after TMT is shown in Figs.4.10c-d. One hundred fifty or more particles were analyzed for each case. In general hot-ECAE is more effective to refine carbides. The average diameter of carbides subjected to cold-ECAE is barely changes, in contrast to a significant reduction from 140 to 56 nm via hot-ECAE (Fig.4.10c). After heat treatment, the carbides coarsen for all extruded specimens (Fig.4.10d), but their average diameter remain less than 100 nm in the hot-ECAE processed material.

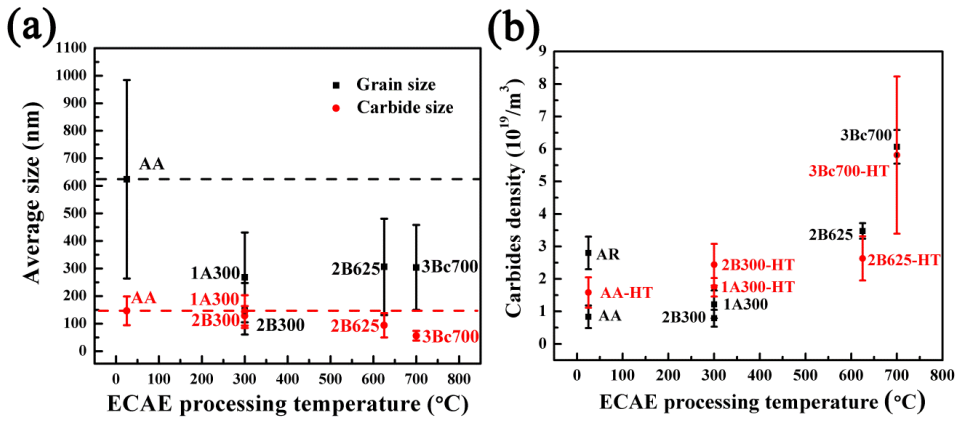

Figure 4.11 (a) The evolution of carbide particles and grain size after ECAE at different temperatures. Cold-ECAE is more effective for grain refinement and achieved an average grain size of ~150nm. Hot-ECAE reduces the average grain size to ~ 300 nm, and is effective for refining the carbide size to ~50 nm. (b) The particle density of carbide was slightly changed after cold-ECAE, but increases significantly during hot-ECAE. Post extrusion heat treatment leads to insignificant variation of carbide particle density.

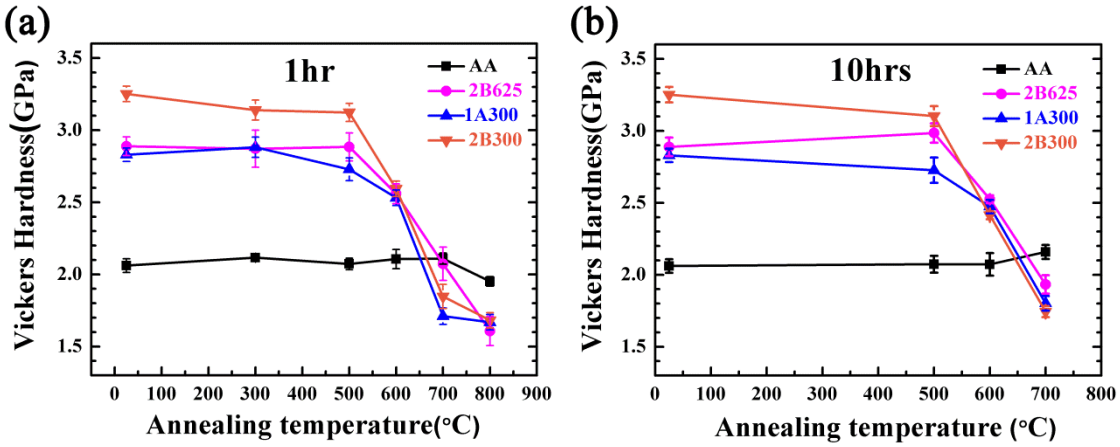

Figure 4.12 Evolution of Vickers hardness of T91 steel after annealing for (a) 1 h and (b) 10 h. The hardness of ECAE processed samples remained unchanged up to 500°C/10h, followed by significant softening at higher annealing temperatures.

Fig.4.11 summarizes the influence of extrusion temperature on the refinement of grain size and carbides. The average grain size decreased after all ECAE processes; the minimum average grain size was achieved in the 2B300 specimen (Fig.4.11a). In parallel, the average diameter of carbides decreased consistently with increasing ECAE

processing temperature. The minimum average diameter of carbide was achieved in the 3Bc700 specimen. Meanwhile, the density of carbides increases gradually at a higher processing temperature, and after processing at 3Bc700 (Fig.4.11b), it reached ~ six times that of the AA specimen. The average thickness of TEM samples was measured to be ~100-150 nm by using the convergent beam electron diffraction technique. After heat treatment, there is an insignificant change in carbide particle density.

Figs4.12a-b show the evolution of hardness of the AA and ECAEed T91 alloys after heat treatment for 1h or 10h, up to 800°C. The AA samples had insignificant hardness variation (consistently low hardness) throughout various annealing experiments. For ECAE processed T91 alloys, hardness remained unchanged up to ~500°C, above which significant softening occurred.

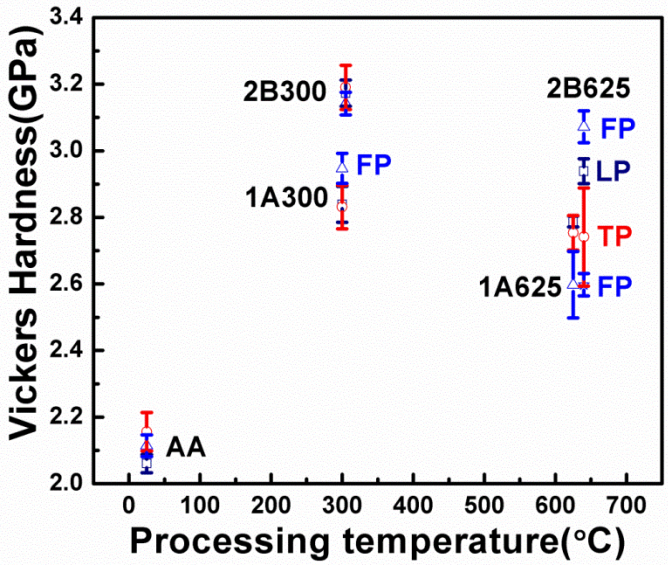

Figure 4.13 Hardness evolution on different planes of ECAE processed T91 steels.

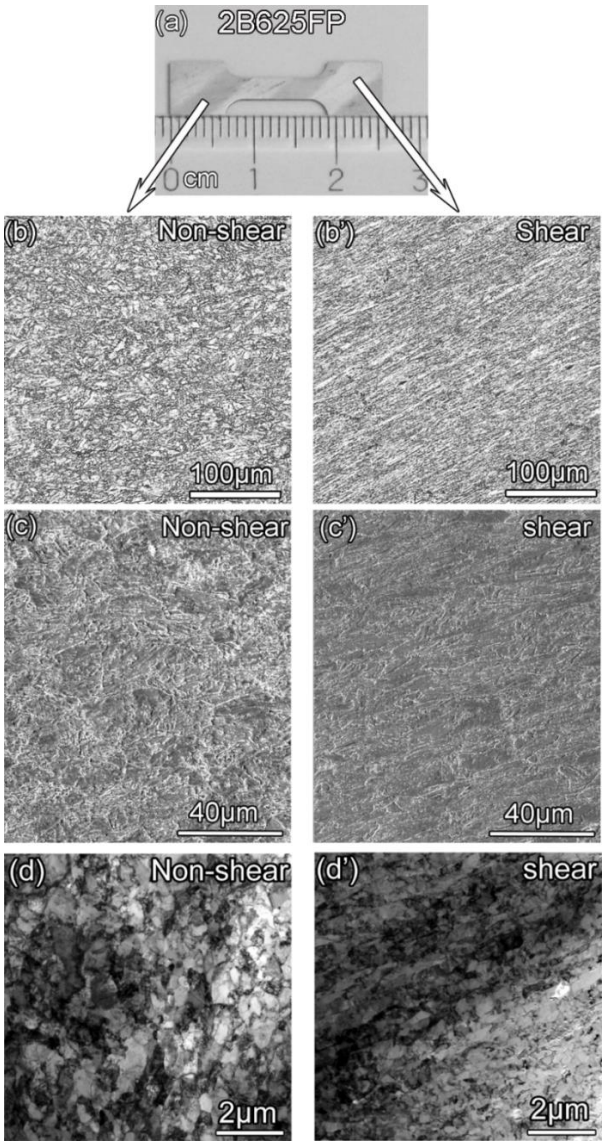

Figure 4.14 Direct observation of shear bands after shear localizaiton. (a) The tensile specimen is etched to reveal the shear and non-shear zones. Optical iamges of (b) non-shear and (b') shear. SEM images of (c) non-shear and (c') shear zone; TEM obsevation of (d) non-shear and (d') shear zone. Signifcnat grain refinement occurred in the shear zone.

4.1.3 Mechanical properties of heavily tempered T91 steel

The Vickers hardness on different planes after extrusion is almost within the error bar for most different case (Fig.4.13). For 2B625, two different values were measured on the FP, while measurement on the TP suffers from a large error bar.

Examination of the microstructure shown in Fig.4.14, indicates that there are two regions on the FP of 2B625. One region appears not have been deformed during the second pass. The other region is sheared during both ECAE passes. The grain size is refined during shearing, which yields a higher hardness.

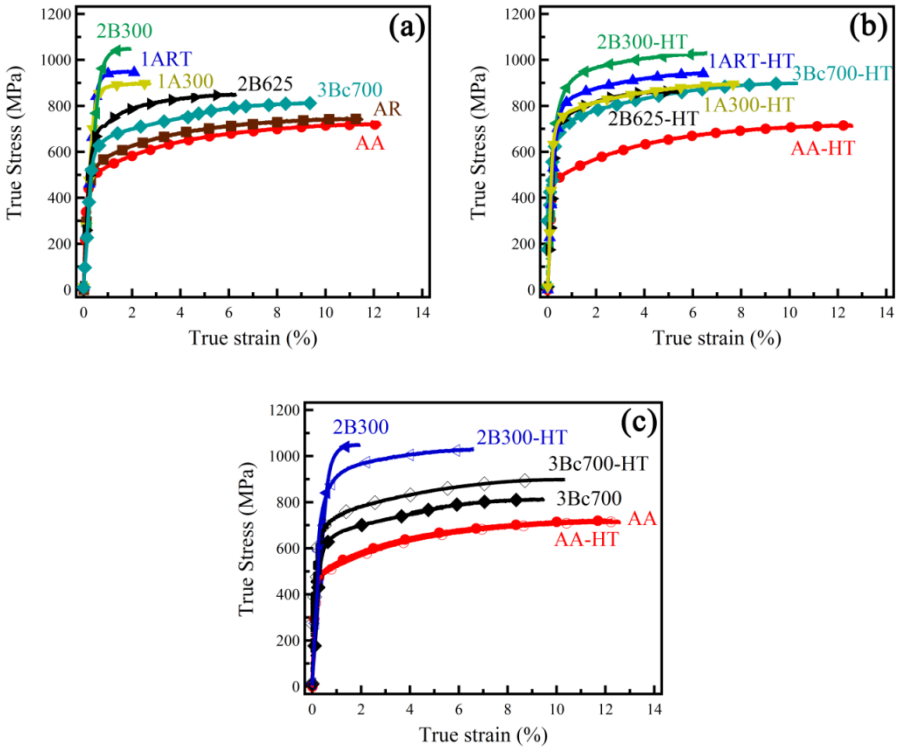

Figure 4.15 Tensile true stress-strain curves of T91 steel. (a) After cold-ECAE (processing at less than 500°C), specimens show a significant increase in yield strength but considerable reduction in uniform elongation. Specimens after hot-ECAE (above 500°C) exhibit a moderate increase in yield strength and retention of ductility. (b) Tensile tests performed on all post extrusion annealed (500°C/10h) T91 steels after ECAE processing. (c) Comparisons show that after annealing, cold-ECAE specimens (2B300) show considerable recovery of uniform elongation and work hardening with insignificant loss of mechanical strength. Whereas the ductility is essentially unchanged for hot-ECAE samples (3Bc700), and a slight increase of tensile strength is noticed.

Fig.4.15a provides a comparison of the tensile true stress – true strain curves of T91 alloys before and after various ECAE processing. The AA materials have slightly

lower ultimate tensile strength (σ_{UTS}) and yield strength (σ_y) than the AR samples with similar ductility. In general, cold-ECAE leads to significant increases in mechanical strength, but diminished work hardening and ductility. The 2B300 samples show the highest σ_{UTS} and σ_y of ~ 1031 and 982 MPa, respectively. Hot-ECAE induces a moderate increase in yield strength and retention of considerable ductility. The 3Bc700 samples exhibit the greatest total elongation (ε_t=22%) and uniform strain (e=11%) among the hot-ECAEed T91 materials. After heat treatment (500°C for 10h), the ductility and work hardening of cold-ECAEed T91 steels improve significantly with a slight reduction of yield strength, and insignificant change in ductility for the hot-ECAEed specimens. Detailed results of tensile test are summarized in Table 4.1.

Table 4.1 Summary of the mechanical properties of the T91 steel subjected to various thermo-mechanical treatment (TMT) conditions. The standard deviations are obtained from multiple independent experiments.

Sample ID	σ_y (MPa)		σ_{UTS} (MPa)		Elongation to failure (%)		True uniform strain (%)	
	Before HT	After HT	Before HT	After HT	Before HT	After HT	Before HT	After HT
AR	508±3	-	681±4	-	20±2	-	10.6±1.5	-
AA	482±3	445±23	646±3	645±3	21±1	24±1	11.5±1	13.9±1.9
1ART	900±2	775±3	935±3	885±3	7.9±0.9	13±1	1.8±0.1	6.5±0.7
1A300	838±3	709±25	886±5	828±7	9.2±0.5	16±2	3±0.4	8.4±1.2
2B300	982±2	845±15	1031±3	968±3	8.5±0.1	16±2	1.8±0.1	6.5±0.7
2B625	681±22	719±13	805±2	848±22	10.9±1	13±1	5.3±1	5.2±0.2
3Bc700	615±4	650±3	763±15	797±23	22±2	22±1	11.1±1.6	11.1±1.1

HT：500°C annealing 10h, furnace cooling

4.2 ECAE processed less tempered martensite and ausforming

4.2.1 Microstructure of TMT T91

The flowchart of TMT processed T91 is illustrated in Fig.4.16. SEM micrographs of the TMT processed T91 steels are shown in Fig.4.17. Similar to the

900WQ T91 steel in the previous chapter, 1000WQ exhibits a mixed of martensite structure. Air cooling of normalized T91 at 1000°C leads to a complex structure including martensite (α'_M), auto-tempered martensite (α'_{AT}), polygonal ferrite (α_P), and bainite (α_B) are shown in Fig.4.17b. Further tempering of 1000WQ at 500°C can encourage the formation of carbides at the PAGBs as shown in Fig.4.17c. Martensite laths are partially tempered during this process. ECAE can build a high density of dislocations in the partially tempered T91 steel. The PAGBs were deformed as shown in Fig.4.17d. Deformed prior austenite grains are a typical feature of the ausformed T91 steel.

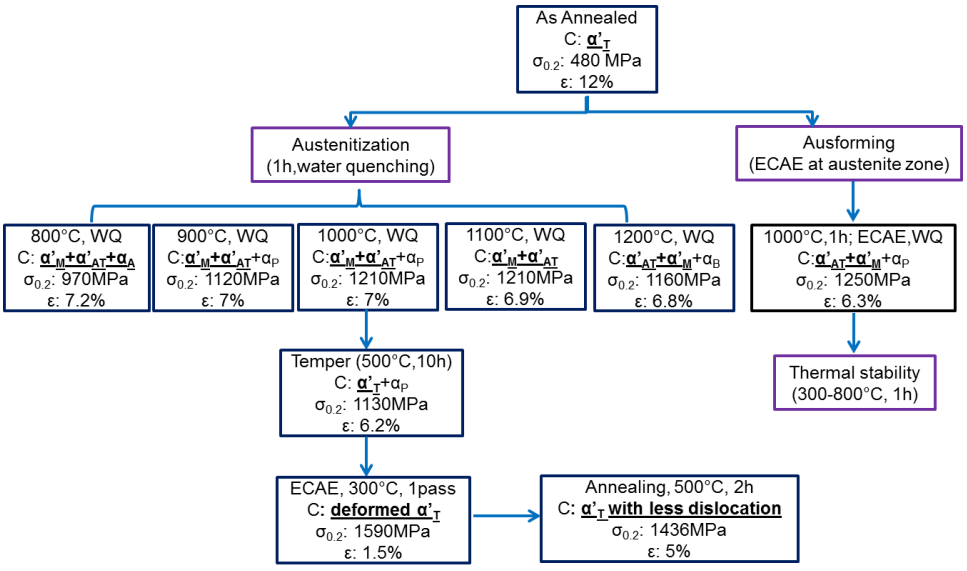

Figure 4.16 Flow chart of thermo-mechanical processing results of T91 steel with microstructure features and mechanical performance after each treatment. Notation: major phase constitution C, yield strength $\sigma_{0.2}$ and uniform elongation ε. Noted among multiple phases, the major phases are highlighted in bold fonts.

Fig.4.18 shows representative TEM micrographs of the TMT processed T91 steel. Auto-tempered martensite (α'_{AT}) and martensite (α'_M) are the predominant phases

in the 1000WQ T91 steel. A partially tempered martensite structure is achieved after 500°C 10h tempering. Further ECAE of tempered martensite gives a deformed martensite with a high dislocation density. Broken martensite laths and vertical growth small grains are observed within the deformed martensite lath structure as shown in Fig.4.18c. Ausforming can give a textured martensite structure. Shorter martensite laths are observed compared to the 1000WQ specimen.

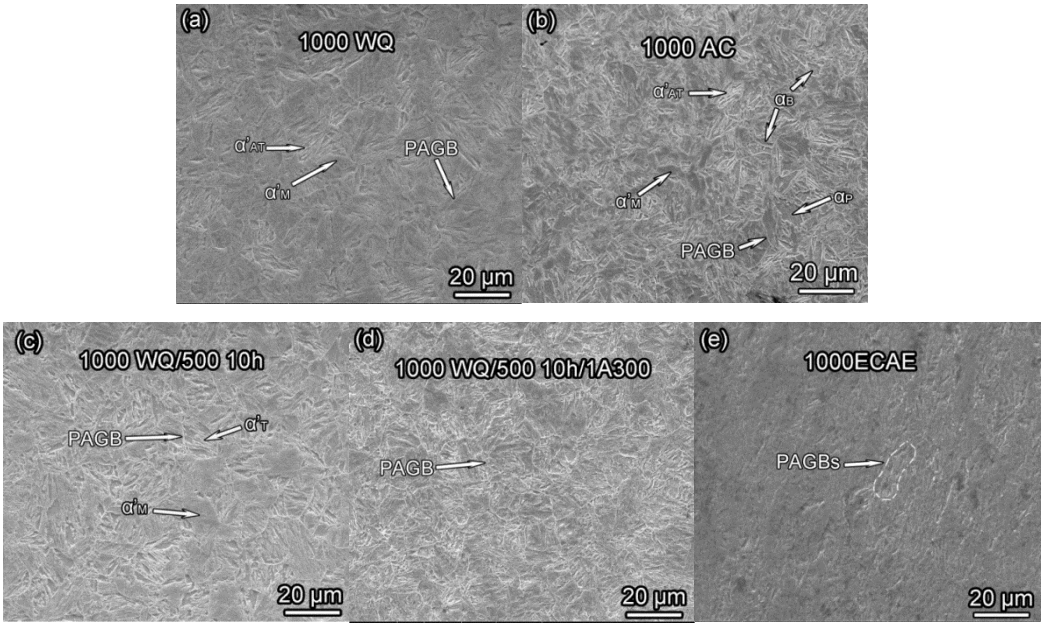

Figure 4.17 SEM micrographs of T91 after various thermomechanical treatment procedures. (a) Water quenching after normalization at 1000°C show a predominately martensite structure ($\alpha'_M + \alpha'_{AT}$). (b) Air cooling after normalization at 1000°C (1000AC) created a complex mixture of martensite (α'_M and α'_{AT}), bainite (α_B) and polygonal ferrite (α_P). (c) Tempering of 1000WQ at 500°C for 10h yielded a tempered martensite structure. The PAGBs become clear due to the formation of GB carbides. (d) ECAE deformation at 300°C of tempered T91 (1000WQ/500C 10h/1A300) induce a deformed martensitic structure. (e) Ausforming of T91 steel at 1000°C (1000 ECAE) leads to a shearing of PAGBs.

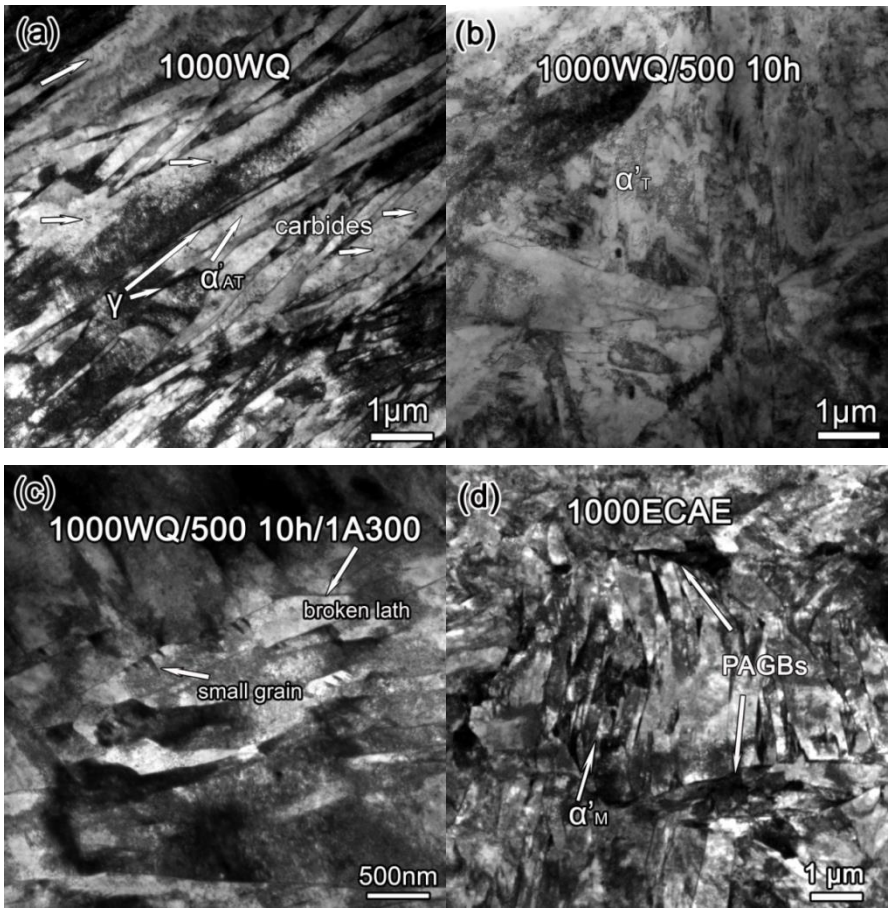

Figure 4.18 TEM micrographs of T91 processed via various thermomechanical treatments. (a)TEM micrograph of 1000WQ T91 shows the existence of α'M laths, and a same fraction of auto-tempered martensite α'AT and residual austenite γ. (b) Heat treatment of the 1000WQ T91(1000WQ/500 10h) gives rise to a tempered martensite α'T structure. (c) ECAE of tempered T91 at 300°C (1000WQ/500 10h/1A300) leads to a deformed martensitic structure with a high dislocation density. (d) ECAE processing at 1000°C followed by WQ (1000ECAE) induces a textured fine martensitic structure (observed from the transverse plane).

4.2.2 Mechanical properties of TMT T91

Fig.4.19 provides a comparison of the engineering stress-strain curves and true stress-true strain curves of WQ T91 steels. In general, the WQ T91 steel shows a good combination of strength and ductility. The yield strength ($\sigma_{0.2}$) of 800WQ was around 970MPa or ~150MPa lower than that of WQ above 900°C. The uniform elongation was

around 7% for all the WQ T91 steels, and is independent to the different austenitizing temperatures.

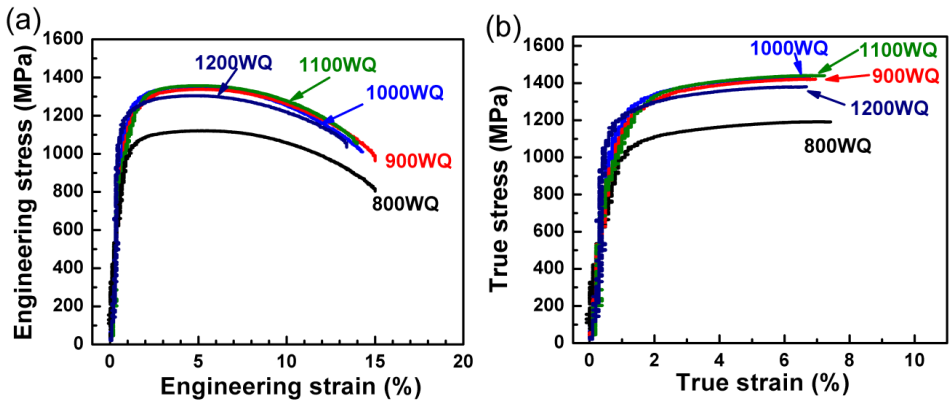

Figure 4.19 (a) Engineering stress-strain and (b) true stress-true strain curves of WQ T91 alloy. Samilar flow stress levels are achieved for 900~1200 WQ specimens, which is ~ 200 MPa higher than that of 800WQ T91.

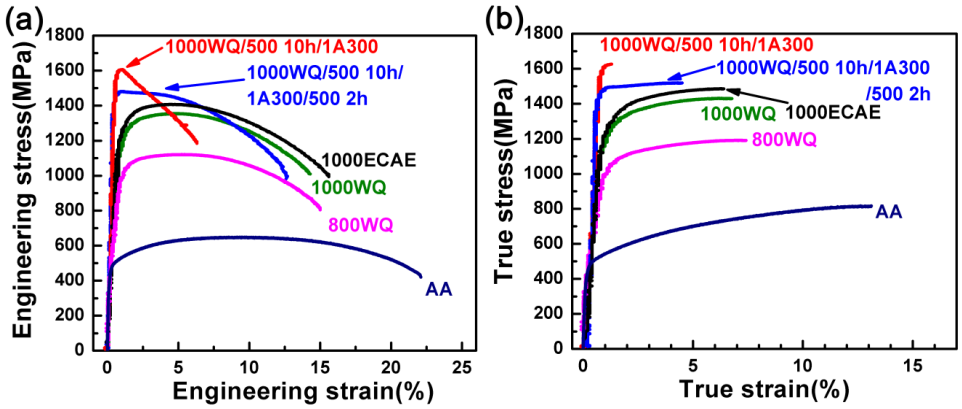

Figure 4.20 (a) Engineering stress-strain and (b) true stress-true strain curves of T91 alloys after various types of thermomechanical treatments. Compared to 1000WQ T91, high temperature ECAE (1000ECAE) leads to a moderate increase of strength with comparable ductility. ECAE at low temperature (1000WQ/500 10h/1A300) causes a substantial increase of the yield strength with however lower ductility. Heat treatment of the same specimen (1000WQ/500 10h/1A300/500 2h) results in a combination of high strength and remarkable ductility.

The mechanical performance of TMT T91 steel at different strength levels is displayed in Fig.4.20. The yield stress of AA material can be increased by a factor of ~ 3.3 from ~ 482 to ~ 1600 MPa after selected TMT processing. Direct quenching can produce a good combination of strength and ductility. Although TMT processed T91 can give different levels of strength, the ductility is sacrificed as shown in Fig.4.20b.

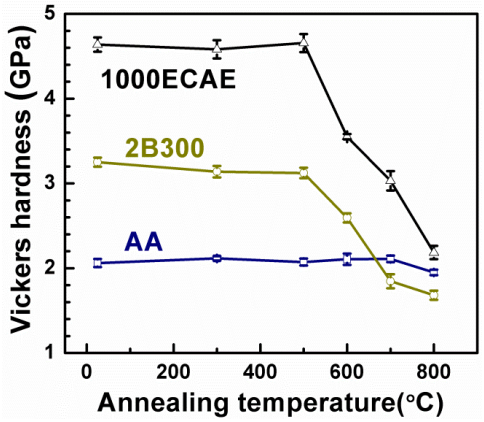

Figure 4.21 Probing thermal stability of T91 via measurement of hardness evolution with annealing temperature for two representative ECAE processing procedures. The hardness of ECAE processed T91 remained unchanged up to 500°C /1 h, followed by significant softening at higher annealing temperatures.

4.2.3 Thermal stability of TMT T91

Thermal stability is characterized by the evolution of hardness vs temperature. Fig.4.21 shows the hardness of 1000ECAE T91 steel after isothermal heat treatment for 1h up to 800°C, with AA and 2B300 T91 data included as a comparison. 2B300 denotes two pass extrusion following route B at 300°C. The Vickers hardness of 1000ECAE is around 2.3 times that of the AA T91 up to 500 °C. Significant softening occurs after 500°C for both ECAEed T91 steels. However, the Vickers hardness of 1000ECAE is

still comparable to the as-worked 2B300 T91. After 800°C, the benefit of deformation becomes neglectable and the hardness could be less than the AA T91 materials.

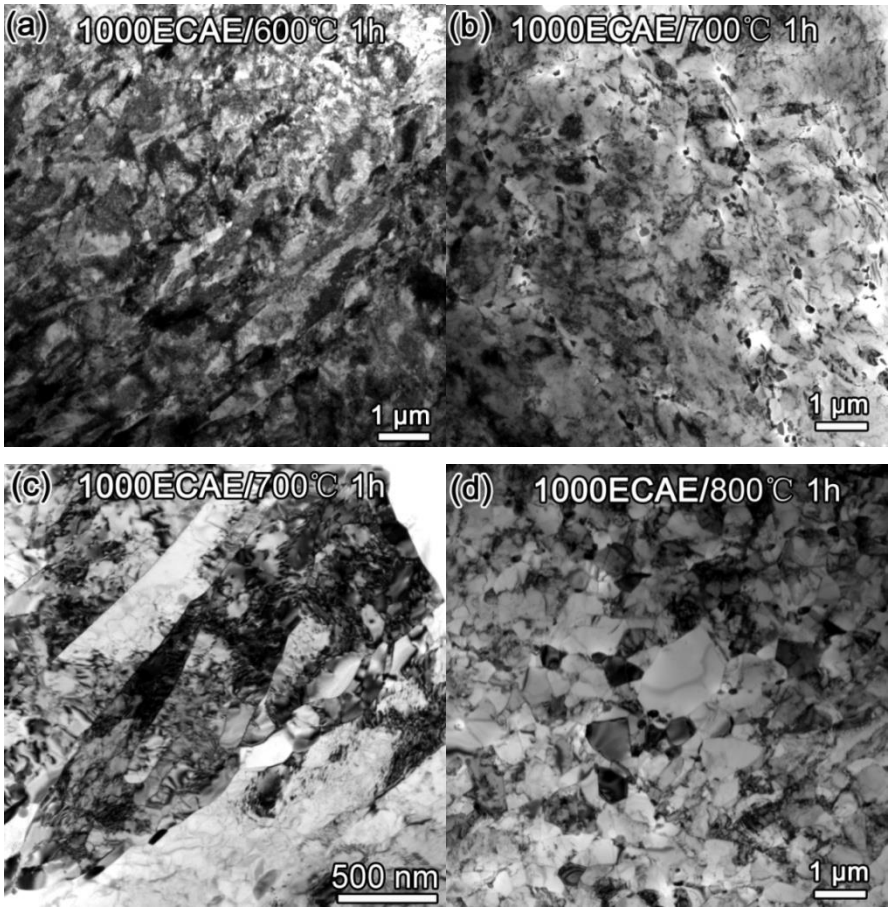

Figure 4.22 TEM micrographs showing microstructure of 1000ECAE T91 tempered at elevated temperatures.(a) After tempering at 600°C, tiny carbides precipitated at martensitic lath boundaries. (b) At 700°C, carbides coarsen and (c) tempered martensitic laths around 0.5 μmin thickness formed by consumingthinner martensitic laths. (d) After tempering at 800°C, recrystallization and grain growth are evident.

Fig.4.22 illustrates the tempering response of 1000ECAE T91 steel at various temperatures. After tempering at 600°C, tiny carbides precipitate at martensitic lath boundaries as shown in Fig.4.22a. Significant coarsening of carbides occurs for 700°C tempering Fig.4.22b. Fig.4.22c shows that tempered martensitic lathsare formed from

thinner martensitic laths. The lath tip of martensite were “blunted” during the process. The microstructure is fully recrystallized and loses the martensitic structure at 800°C after ausforming as shown in Fig.4.22d.

4.3 Road map for strengthening T91and strength-ductility paradox

We now evaluate the influence of TMT at various conditions on work hardening of T91 steels. Uniform elongation, as a key parameter to evaluate ductility, is determined from the stain at onset of necking, where work hardening cannot sustain the geometrical weakening of the deformed region[183, 184]. The Considère criterion is widely used to determine the onset of necking [185],

$$\left(\frac{\partial\sigma}{\partial\varepsilon}\right)_{\dot{\varepsilon}} = \sigma \qquad \text{Eq.4.1}$$

where σ and ε are true stress and true strain, $\dot{\varepsilon}$ is the strain rate, and $\partial\sigma/\partial\varepsilon$ is the work hardening rate. The strain that satisfies this criterion is considered true uniform elongation. Fig.4.23 compares several representative cases. The AA specimen has lower yield strength, but a high work hardening rate, and consequently can sustain a large uniform elongation. The large grains in the AA specimen have a low density of preexisting dislocations, and thus can accommodate a rapid increase of mobile dislocation density during deformation. In contrast, the cold-ECAEed 2B300 specimen has higher yield strength but significantly lower work hardening rate and diminished uniform elongation. The cold-ECAE process induces a high density of dislocations in 2B300 in grain interior, making it difficult to nucleate mobile dislocations during

deformation, resulting in very limited work hardening capability. The hot-ECAEed 3Bc700 specimen has 20% greater yield strength than AA and a comparable work hardening rate and ductility as the specimen has a low density of dislocations in the grain interior. After annealing, the 2B300 specimen at 500°C, recovery occurs as evidenced by the reduction of intragranular dislocation density, accompanied by a moderate increase in average grain size (from 150 to 200 nm). The significantly higher work hardening ability leads to a several times greater uniform elongation in 2B300 T91. Interestingly, annealing of 3Bc700 T91 leads to a greater yield strength and ultimate tensile strength in spite of moderate grain growth (from 300 to 350 nm). We suspect that the precipitation of fine carbide nano precipitates may have led to the slight increase of mechanical strength. The source limited strengthening stated previously could be an alternative explanation. The forgoing discussion clearly suggests that hot ECAE is a preferred way to achieve enhanced work hardening capability so that a combination of high strength and high ductility can be achieved.

Fig.4.24 compares the water quenching and ausforming processing. The grain boundary ferrite phase within the 800WQ specimens can provide additional room for a rapid increase of mobile dislocations, thus it can have better ductility. However, the ferrite phase is softer than the martenstie or tempered martensite. Thus, the strength is lower for the 800WQ specimen compared to that of 1000WQ or 1000ECAE. Auto-tempered martensite commonly shows a higher preexisting dislocation density. It is hard for auto-tempered martensite grains to accommodate a rapid increase of mobile dislocation during deformation, thus it turns out to have a lower ductility.

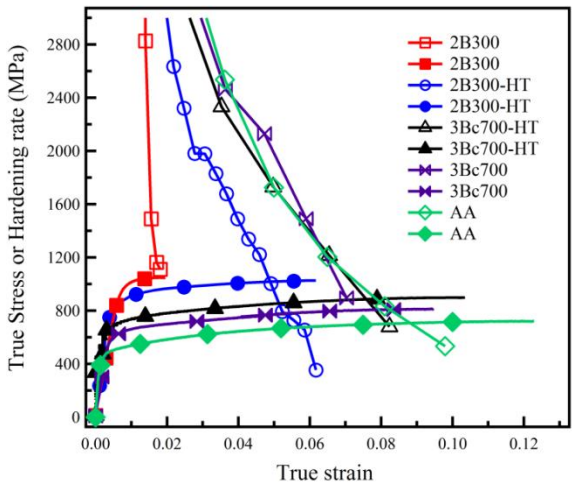

Figure 4.23 Plots of work hardening rate (open data point) and true stress-true strain (solid data points) for ECAE processed T91.The intersection of the two curves is where plastic instability starts ($d\sigma/d\varepsilon=\sigma$). Cold ECAE (2B300) leads to a significant reduction of work hardening rate and uniform elongation. Annealing can lead to recovery of uniform elongation. Hot-ECAE (3Bc700) results in greater yield strength, and similar work hardening capacity and ductility compared to AA specimens.

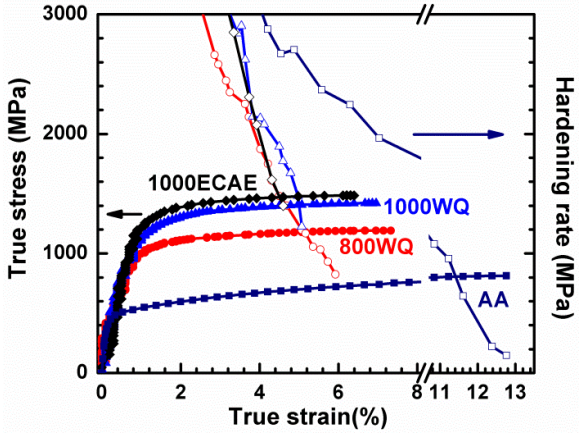

Figure 4.24 Plots of work hardening rate (open data) and true stress-true strain (solid data points) for several WQ T91 steels and 1000ECAE T91. The intersections between the two sets of curves imply the initiation of plastic instability. AA T91 has excellent uniform elongation. WQ leads to the reduction of uniform elongation to a few percent. 1000ECAE results in a ductility comparable to that of WQ T91.

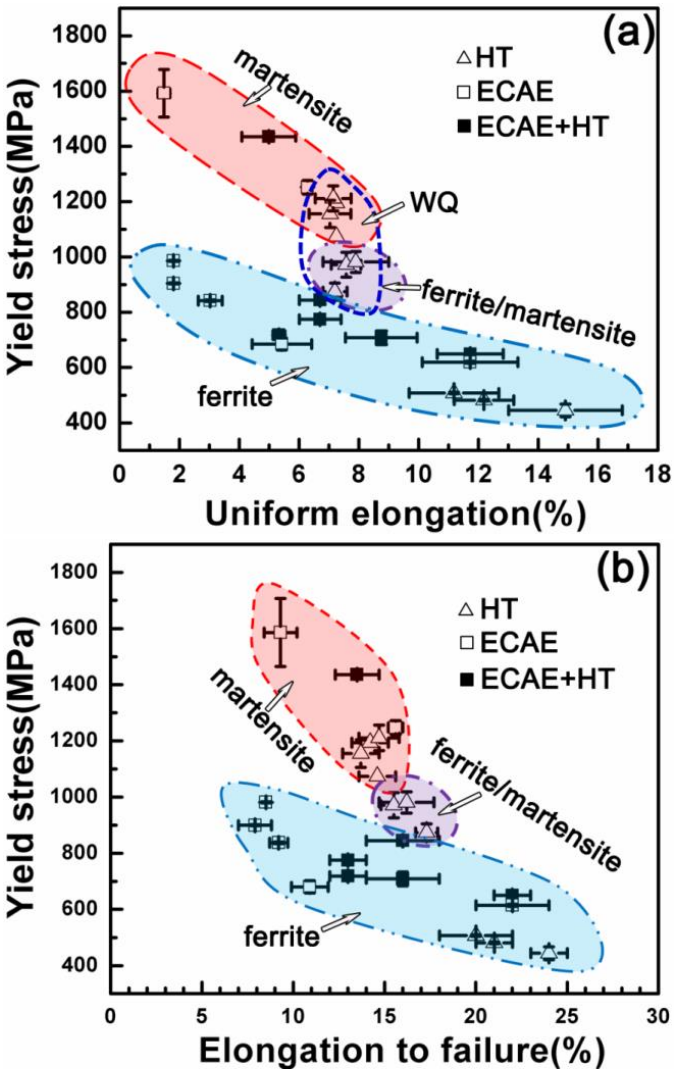

Figure 4.25 Summary of yield stress-uniform elongation (a) and yield stress-elongation to failure (b) maps for T91 steel subjected to various types of thermomechanical treatment. Three distinctive zones are identified based on the primary phase after processing. In the lower ferrite zone with a banana shape (light blue), ECAE of the ferrite phase T91 steel leads to fine ferrite. Heat treatment at various temperatures were applied to tailor strength and uniform elongation. In general, a higher strength is accompanied by lower ductility. In the upper martensite zone (red shadow), including water quenching from 900-1200°C, 1000ECAE or 1000WQ/500 10h/1A300/500 2h leads to martensite with a combination of high strength and reasonable ductility. In the middle ferrite/martensite regime (purples shadow), T91 is processed by primarily water quenched from 800°C and tempering of water quenched specimens at 600°C. Water quenching from 800-1200°C always leads to ductile martensite with several percent of uniform elongation because of the auto-temper effect.

The increased strength of a given material will always be accompanied by sacrificing ductility. Any increase in strength will somehow decrease the dislocation

accumulation ability and thus decrease the ductility, which is the actually strength and ductility paradox. Fig.4.25 shows the situation clearly in T91 steels. Processing with the heavy tempered martensite, which is predominant ferrite, will always be located within the banana region. This processing can include ECAE and annealing. However, when the phase construction is changed, the strength and ductility can change to new levels. Further processing of the less tempered or auto-tempered martensite will again fall into the banana region. Multi strength level can be achieved within single materials after these ECAE enabled TMT process in T91 steel.

4.4 Summary

In this chapter, ECAE was applied to T91 steels with various heat treatment histories. This ECAE enabled TMT process can alter strength in T91 steels to different levels which can be applied as high strength for bolting or low strength for baffle. Thermal stability is identified as a major issue for the deformed material which limits the applications to below 500°C.

CHAPTER V

REFINING AND STRENGTHENING MECHANISMS OPERATING IN T91 STEEL

In this chapter, the grain and carbide refining mechanisms of the TMT process is discussed. A carbide refining mechanism is proposed when T91 is subjected to hot-ECAE. The possible associated strengthening mechanism is discussed in general. Selected mechanisms are applied to the ECAE enabled TMT processed T91 steels.

5.1 Microstructure refining mechanism

5.1.1 The grain structure evolution of ECAE processing T91 steel

Grain refinement and the evolution of GB misorientation angle during ECAE processing are dislocation dominated processes [57].As the dislocation density increases with plastic strain (ECAE), dislocations become entangled and form dislocation cells. At greater plastic strain, the width of cells decreases and the cell walls become sharper as the misorientation angle between two neighbor cells increases. Sub-grains with high angle GBs eventually form through a polygonization process.

The initial structure of tempered martensite laths within prior austenite grains exhibits low angle GBs in the AA and AR samples. A similar microstructure has been observed by electron backscattered diffraction (EBSD) mapping of T91 during long term of aging [186]. During ECAE, the density and distribution of dislocations are strongly dependent on deformation temperature. Though the same amount of strain is applied, a

smaller grain size (~ 150 nm) is achieved during cold-ECAE compared with that of hot-ECAE (~ 300 nm). This is because, at low processing temperatures, the dislocations proliferate with a slow recovery rate, so the process of grain refinement through accumulation and interaction of dislocations can progress to a greater extent. The cold-ECAE processed specimens (1ART, 1A300 and 2B300) show a higher density of dislocations than the hot-ECAE counterparts because of suppressed dynamic recovery. The formation of low angle GBs after a single ECAE pass is consistent with early observations in pure Al and Al alloys [65, 79], which show that during the early stages of dislocation interactions, the cell walls typically form low angle GBs. After two passes, high angle GBs begin to form. Three passes following route Bc enables GBs to evolve into predominately high angle GBs. It has been shown that route Bc is an effective route to populate high angle GBs [65].

5.1.2 The evolution of carbide precipitates during ECAE and post-processing heat treatment

Compared with an understanding of grain refinement mechanisms via ECAE, the evolution of precipitates during ECAE processing is less well understood. The mechanical deformation can have a significant effect such as the fracture and redistribution of particles in precipitation-hardened Al alloy studies [79, 80], where the precipitates commonly have a long plate or rod shape which induces large bending stresses or fracture. Previous studies on Al based metal matrix composites show limited broken Al_2O_3 particles, which were refined via the ECAE process [81]. The high

processing temperature probably caused the lack of refinement of the particles. The precipitation of carbides during ECAE in the present T91 alloy strongly depends on the processing temperature. After cold-ECAE, large carbide precipitates are present at the prior austenite GBs, whereas for the hot-ECAE processed T91 steels, the carbide precipitates are effectively refined and mostly are of the intragranular type.

The refinement mechanisms of carbides via cold- and hot- ECAE processing are proposed in Fig.5.1 by using 300°C and 700°C as examples. During cold-ECAE as illustrated in Fig.5.1a-d, although grain size has been significantly refined, the prior austenite GBs have not been completely decomposed. The large carbide precipitates preferentially formed at these GBs are less affected by ECAE as the processing temperature is not sufficient to promote the decomposition of carbides. The coarsening of carbides after post extrusion annealing (500°C/10h) could be explained by the preferential reprecipiatation of carbon to prior austenite GBs by pipe and GB assisted diffusion of carbon [181].

During hot-ECAE as shown in Figs.5.1b'-d', the prior austenite GBs (the preferential nucleation sites for carbide) are eliminated. The higher processing temperature (625°C or greater) together with a high density of dislocations and GBs assist rapid diffusion of carbon, so that new carbides with much smaller size form both intergranularly and intragranularly. These particles together with the undissolved small carbides (carbides which were not fully dissolved during the heat treatment prior to ECAE) lead to a more homogenous distribution of carbides. Post extrusion annealing (500°C/10h) did not lead to significant coarsening of carbides, implying that hot-ECAE

is a remarkable approach to achieving a uniform microstructure and retention of fine carbide precipitates. A combination of hot-ECAE and cold-ECAE has the potential to achieve a fine structure with smaller grain size and fine uniformly distributed particles.

5.2 The strengthening mechanism

The strengthening mechanisms occurring in T91 alloy include: solid solution hardening, second phase strengthening, precipitation hardening, work hardening, and dislocation pile-ups at grain boundaries or lath boundaries (Hall-Petch relationship). The yield strength σ_y of single phase T91 (ferrite or martensite) can be estimated by the following equation (where rule of mixture applies):

$$\sigma_y = \sigma_{Fe} + \sum_i \sigma_{ssi} + \sigma_c + \sigma_p + \sigma_{dis} + \sigma_{GB} \qquad \text{Eq.5.1}$$

where σ_{Fe} is the lattice friction of the Fe matrix, σ_{ssi} is solid solution hardening from the i element, σ_c is the solid solution hardening from carbon, σ_p is the precipitation hardening, σ_{dis} is dislocation strengthening based on Taylor's equation, and σ_{GB} is strengthening from the grain boundaries or martensitic lath boundaries.

The lattice friction can be estimated by the interception of Hall-Petch type plot with the y axis (stress), which is also the yield stress of coarsen grained Fe. Han*et al* reported a yield stress of 100MPa for a grain size around 200 μm for a 99.95wt% Fe with a carbon content less than 1ppm [188].

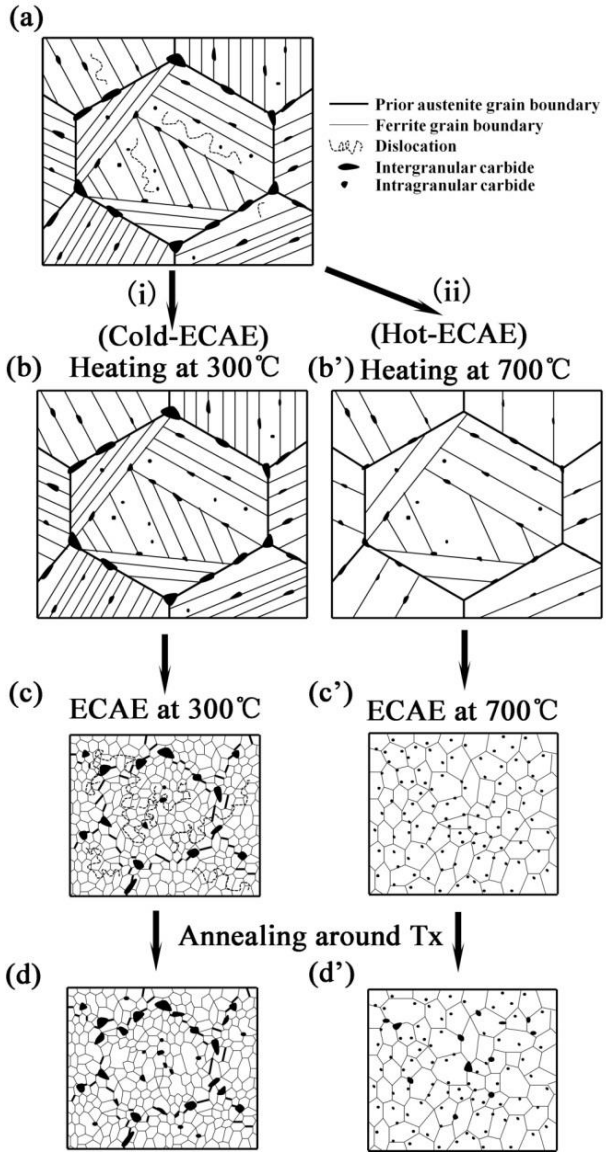

Figure 5.1 Illustration of evolution of grain boundaries and precipitates subjected to various routes of TMT: (i) cold-ECAE (a→b→c→d), and (ii) hot-ECAE (a→b'→c'→d'). The drawing of tempered martensite structure follows the style of Sakasegawa et al [187]. (i) For the route of cold-ECAE, the prior austenite grain boundaries are the preferred nucleation site for large intergranular carbides (5.1a).Annealing at 300°C (prior to ECAE process) moderately reduces the dislocation density (5.1b). After cold-ECAE, the prior austenite grain boundaries are topologically and chemically conserved, and in parallel significant grain refinement occurs (5.1c). Post-ECAE annealing at 500°C (~ recrystallization temperature) reduces the dislocation density, but relatively large carbides are reprecipitated around prior austenite grain boundaries (5.1d). (ii) In comparison, during hot-ECAE, the prior austenite grain boundaries are eliminated, so the carbides begin to precipitate uniformly around the grain boundaries of ultrafine grains, and the average dimension of carbide precipitates is significantly reduced (5.1c'). Post extrusion annealing at 500°C does not lead to the reprecipitation of large carbides. Instead, a more uniform microstructure is obtained (5.1d').

The solid solution hardening (MPa) in T91 can be estimated by the following equation at room temperature [189],

$$\sigma_{ss} = \sum_i \sigma_{ssi} + \sigma_c = 1723\sqrt{[C]} + 5.8[Cr] + 18[Mo] + 105[Si] + 45[Mn] + 37[Ni] + 4.8[V] \quad \text{Eq.5.2}$$

where [X] is the wt.% of X solute. For the ferrite phase, the solution hardening is estimated by considering the reduction of Cr content in the form of $Cr_{23}C_6$ carbides, which are the main form of carbon atoms (lower than 0.00005 solid solution at room temperature in ferrite[189]). The solution hardening is calculated as ~132 MPa at maximum. The solution hardening for martensite is 128MPa for substitute alloying atoms and 505 MPa for interstitial carbon. The solid solution hardening for the substitute alloying atom show few differences in the ferritic or martensitic phase. However, carbon atoms contributes significantly to the hardening, because that can cause asymmetrical distortion of the crystal structure, and thus impede mobile dislocation [189]. However, too much solid solution carbon atoms may lead to load transfer from common easy slip system to other slip systems, which can lead to poor ductility, as brittle martensite. For the present martensitic T91 steel, the c/a ratio is 1.00387 according to the equation in the reference [189], which is not significantly different from that of the bcc structure, which explains the good ductility of martensite in the WQ T91 steel.

Precipitation hardening is estimated using the Ashby-Orowan relationship [190],

$$\sigma_p = (0.538Gbf^{1/2} / X)\ln(X / 2b) \quad \text{Eq.5.3}$$

where G is the shear modulus about ~ 8.2×10^4 (MPa) of Fe, b is the Burgers vector 2.49×10^{-7} for present alloy (mm), f is the volume fraction of particles, and X is the diameter of the particles. We can also use the simple Orowan mechanism [191],

$$\tau = \beta Gb / L \qquad \text{Eq.5.4}$$

where τ is the additional shear stress necessary for a dislocation to bypass an obstacle, and β is a parameter related to the detachment angle for dislocations and is ~ 0.81 [192]. L is the inter-particle distance on the slip plane, which could be related to the particle density n via

$$L \propto 1 / \sqrt[3]{n} \qquad \text{Eq.5.5}$$

Please notice that different models may give totally different strengthen values.

A modified Hall-patch model is introduced here. In the modified model proposed by Hansen [193-195], GBs are subdivided into incidental dislocation boundaries (IDBs) and geometrically necessary boundaries (GNBs) according to the different configuration of GBs. The IDBs are presumably formed by mutual trapping of glide dislocations, and thus cause dislocation strengthening. The GNBs are boundaries whose angular misorientations are controlled by the difference in glide-induced lattice rotations in adjoining volumes, and are considered as GB strengthening. Similarly, the modified strengthening equation can be written as [195]:

$$\sigma_{dis} + \sigma_{GB} = M\alpha Gb\sqrt{\rho_0 + (\frac{3(1-f)\theta_{dis}}{bd_R})_{IDB}} + k\sqrt{(\frac{f}{d_R})_{GNB}} \qquad \text{Eq.5.6}$$

where the M is Taylor factor (=2.733 for BCC iron) [196], α is 0.4 for BCC metal [188], which describes an average interaction strength between dislocations [197], G is the shear modulus (82GPa for the present alloy with ν assumed to be 0.33), b is the Burgers vector (2.49×10^{-10} m for the present alloy), d_R is the average spacing between

boundaries, ρ_0 is the initial dislocation density, θ_{dis} is average GB misorientation angle below the critical angle, f is the volume fraction of GNBs, and k is the grain boundary strength. The critical angle is GB misorientation angle, above which the GBs can be considered as GNBs and below that the GBs can be treated as IDBs. The values of f and θ_{dis} vary depending on the critical angle. The first term in Eq.5.6 arises from IDBs, which considers strengthening contributions from both initial dislocations and low angle GBs. The second term represents strengthening due to GNBs, which are typical high angle GBs.

The yield stress for the duplex structure (as in 800WQ case) is as follows (rule of mixtures),

$$\sigma_y = x_f \sigma_{yf} + x_m \sigma_{ym} \qquad \text{Eq.5.7}$$

where x_f and x_m are the volume fraction for ferrite and martensite, σ_{yf} and σ_{ym} are the yield strength for the ferrite and martensite.

In the ECAE ferrite T91 steels, the main operating mechanisms strengthening by dislocation, grain size, and precipitates. An established strengthening model which considers dislocation density ρ and grain size d was proposed as follows [198], where the simple rule of mixtures is applies, the total strengthening should in the form as follows:

$$\sigma_y = \sigma_0 + \lambda\sqrt{\rho} + \beta/\sqrt{d} \qquad \text{Eq.5.8}$$

where σ_0 is the lattice friction, the second term is basically Taylor's equation, and the third term arises from the Hall-Petch relationship.

Table 5.1 Calculated precipitation hardening induced by carbides.

Sample ID	Particle density (10^{19}/m^3)		Precipitation hardening (MPa)	
	Before HT	After HT	Before HT	After HT
AR	3.1±0.7	-	~140	-
AA	0.8±0.3	1.6±0.5	~90	~110
1A300	1.2±0.4	1.7±0.3	~105	~120
2B300	0.8±0.3	2.4±0.6	~90	~130
2B625	3.5±0.2	2.6±0.7	~150	~135
3Bc700	6.1±0.5	5.8±2.4	~180	~175

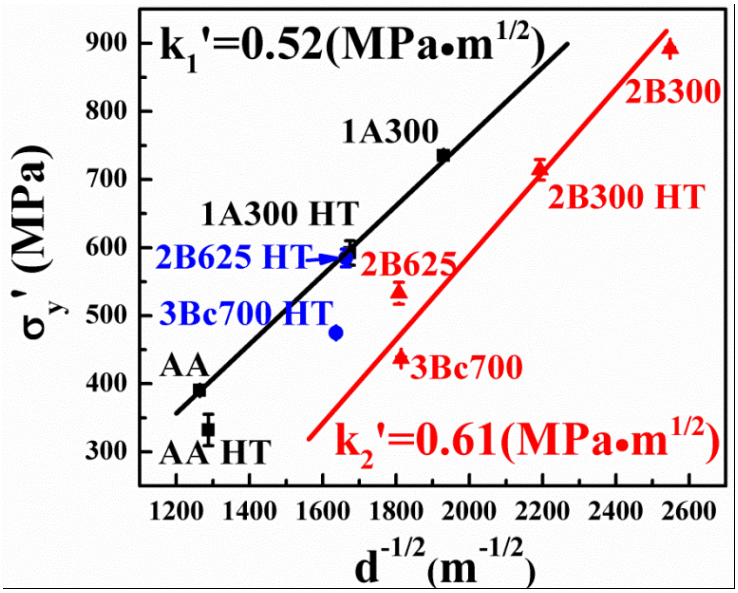

Figure 5.2 Hall-Petch relationship of the ECAE processed T91 steel. The black line is a linear fit of specimens with predominately IDBs (incidental dislocation boundaries). The red line is a linear fit for specimens with GNBs (geometrically necessary boundaries). The points of 2B625HT and 3Bc700HT do not belong to either of the two cases. The equivalent grain boundary strength k_2' is larger than k_1', which indicates the GNBs are more effective barriers than IDBs for pile-up of dislocations.

Add all terms into the Eq.5.8, and the final form of the strengthening equation becomes:

$$\sigma_y = \sigma_0 + M\beta Gb\sqrt[3]{n} + M\alpha Gb\sqrt{\rho_0 + (\frac{3(1-f)\theta_{dis}}{bd_R})_{IDB}} + k\sqrt{(\frac{f}{d_R})_{GNB}} \quad \text{Eq.5.9}$$

The above equation can be written as a modified Hall-Petch relationship form,

$$\sigma_y = (\sigma_0 + M\beta Gb\sqrt[3]{n}) + \left\{ M\alpha Gb\sqrt{\rho_0 d_R + \frac{3(1-f)\theta_{dis}}{b}} + k\sqrt{f} \right\} \frac{1}{\sqrt{d_R}} = \sigma' + k' \frac{1}{\sqrt{d_R}} \quad \text{Eq.5.10}$$

This equation shows that σ' and k' can be influenced by several factors.

The precipitation hardening due to carbide particles is calculated and listed in Table 5.1. The magnitude of calculated precipitation hardening for the 3Bc700 specimen is nearly two times that of AA samples before heat treatment. To fit the Hall-Petch equation, the contribution of precipitation hardening should be removed from the yield strength as follows:

$$\sigma_y' = \sigma_y - M\beta Gb\sqrt[3]{n} = \sigma_0 + k' \frac{1}{\sqrt{d_R}} \quad \text{Eq.5.11}$$

where σ_y' is the equivalent yield stress without a precipitation hardening effect.

In the present study, isolation of these parameters is not easy. Further assumptions must be made to fit the Hall-Petch relationship to fit the experimental data. We now attempt to explain strengthening in two groups of T91 specimens.

In the first group of specimens, the GBs of AA, AA HT, 1A300, and 1A300 HT specimens are predominately of low angle type, which could be converted into dislocation density. So these samples have something in common: dislocation density plays a major role in their strengthening mechanism. In these specimens, assume f = 0 (that is all GB angles are below the critical angle, thus there is no contribution from GNBs), andρ_0 is assumed to be on the order of $10^{14}/m^2$. An angle between 2~2.5° will yield a k' in the range of 0.47~0.54 MPa·$m^{1/2}$ over the grain size of 268 ~ 624 nm.

Experimentally, the linear fit of hardness for these specimens results in a slope k_1' of 0.52 MPa·$m^{1/2}$ (with R^2 of 0.997) as shown in Fig.5.2. The angle used to estimate the hardening from Eq.5.10 is comparable to that of deformed pure Al, Ni, Cu and IF steel (interstitial free steel), 0.4-4° [195, 199]. The linear fit of the ECAEed T91 using the Hansen's modified model indicates that dislocations and low angle grain boundaries account nicely for their hardening.

The second group of specimens, 2B625, 3Bc700, 2B300 HT and 2B300 specimens also share a common feature: their GB angles are predominately high angle. Although the dislocation density is high in 2B300 specimens, after two passes of ECAE, most other specimens have a relative low density of dislocations and an insignificant fraction of low angle grain boundaries. So GB strengthening may dominate the strengthening process in these specimens. A slope of k_2'=0.61 MPa·$m^{1/2}$ is achieved with a good linear fit (R^2=0.995). This value is approximately equal to k' when f is 1. The slightly larger value compared to the low angle GB case implies that high angle GBs are stronger barriers than low angle GBs for blocking the migration of dislocations.

The 2B625HT and 3Bc700HT specimens are not included in the plot because annealing induced hardening in these specimens. The slight hardening after annealing may be caused by several factors. First, source limited deformation in UFG materials could be an explanation. It is known that GBs are sources for nucleation of dislocations. Irregularity (ledges or steps) at GBs are more likely to trigger the nucleation of dislocation because the stress concentration at these locations may be higher. During annealing of the 2B625 and 3Bc700 specimens, the population of irregularities at high

angle GBs may decrease. Additional stress is thus needed to activate new dislocation sources at GBs during deformation. Source limited strengthening has been frequently observed in Ni, Au, and Mo submicron pillars [200-202], and heavily worked pure Al with submicron grain sizes [203]. Second, during annealing, the precipitation of fine nanoscale carbides (below the resolution of microscopy studies) may also contribute to hardening.

The overall scenario of all the T91 steels is as follows. The AA sample had the lowest yield strength ~ 480MPa, because of the large grains, and coarsened carbides and a relatively low dislocation density. The strengthen difference ~ 365 MPa between AA and 2B300HT is mainly a grain size effect. These two samples exhibited similar carbide size and a low dislocation density. The strength difference between 1000WQ ~1180 MPa and 3B700HT ~ 650MPa, is mainly the carbide solution effect. The lath size is ~300nm for 1000WQ, which is close to the grain size of 3B700HT. If we assume the k value is same for ferrite and martensite, the carbon solution hardening gives ~ 505 MPa extra strength in martensitic T91, which is close to the gap ~530MPa. The difference between 1000WQ+ ~1500MPa and 1000WQ ~1180MPa is from the reduced lath thickness and increased dislocation density. The yield strength of the duel phase materials is between the fully ferrtic and fully martensitic cases, which could be understood by Eq.5.7, where the soft ferrite phase within the matrix will lower the overall strength of the materials which is around 200 MPa in the present case.

5.3 Summary

In this chapter, the refining mechanisms for grains and carbides were discussed. A new carbide refining mechanism was proposed. The element behavior around PAGBs plays a key role in redistribution of the carbides. Various strengthening mechanisms are discussed related to solution hardening (Cr, Mo, et al), second phase strengthening (α_A and α'_M), precipitation hardening (carbides), dislocation hardening, and a Hansen Modified HP model. However, a detailed calculation to fit the strength data remains challenging. We realize the calculated data is sensitive to the model chosen.

CHAPTER VI

ECAE PROCESSED ODS STEEL*

In this chapter, the ECAE technique was extended to process two 12Cr ODS steels. The mechanical performance and thermal stability were evaluated. Special attention was paid to the evolution of tiny oxide particles. The oxide difference between these two ODS steels was found to play a key role in the strengthening and thermal stability of ODS steels.

6.1 ECAE processed oxide dispersion strengthening (ODS) steel

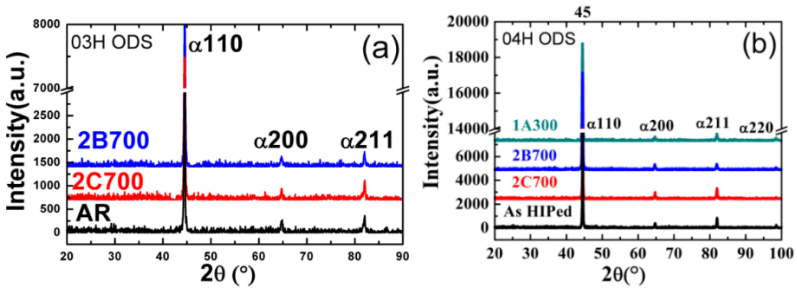

Figure 6.1 X-ray diffraction patterns of ODS steels (a) 2103H and (b) 2104H. All peaks correspond well to the bcc ferritic phase with a lattice parameter of ~ 0.288 nm. No oxide peaks are seen.

The XRD patterns of two ODS steels after various ECAE routes are shown in Fig.6.1. The pattern of the as-HIPped sample can be indexed very well with a BCC structure with a lattice parameter of ~ 0.288 nm. No obvious Y_2O_3 peaks are detected in

*Partially reprint with the permission from "Microstructure refinement and strengthening mechanisms of a 12Cr ODS steel processed by equal channel angular extrusion" by M. Song *et al*, 2013. Journal of Alloys and Compounds, 577, 247-256, Copyright [2013] by Elsevier.

both steels, because the relatively low volume fraction of the oxide nanoparticles is beyond the resolution of the present equipment. The grain and particle structure after shear processing will be discussed separately in the following pages.

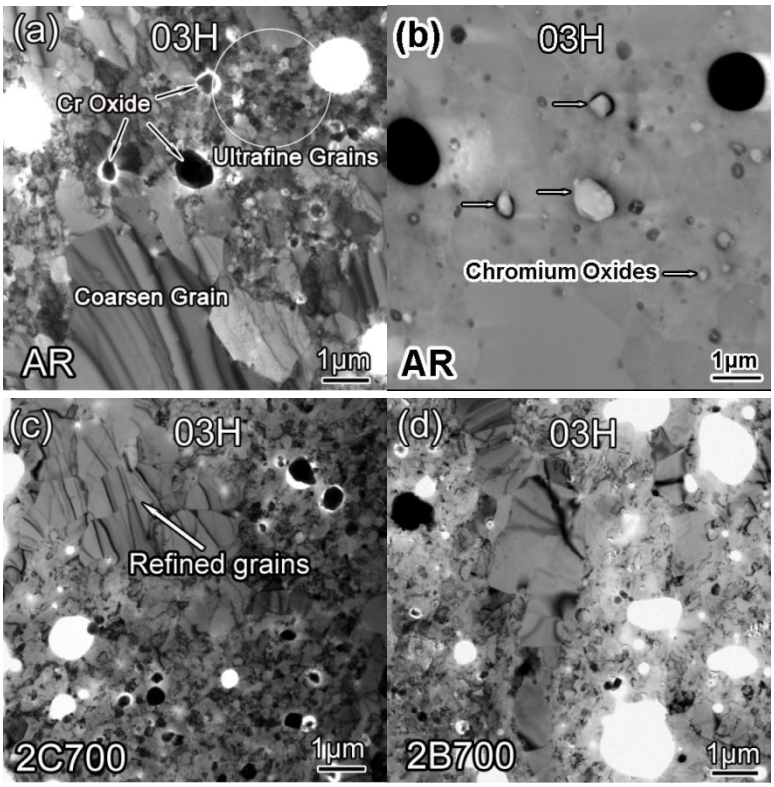

Figure 6.2 (a) Bright field TEM micrograph of as-received 2103H ODS steel having a bimodal structure, i. e. larger grains, ~several microns in diameters, and puddles of ultrafine grains, ~ 250nm, spotted with black chromium oxide particles. (b) Corresponding STEM image of the same region shows the chemistry and thickness contrast from chromium oxide particles with various sizes. (c-d) TEM micrographs of ODS steel following 2C700 and 2B700 ECAE processing conditions. The large grains are refined during the ECAE process.

6.1.1 Grain structure

Fig.6.2 (a) shows a representative TEM micrograph of the as-HIPped 03H ODS steel after electro polishing. The as-HIPped 03H ODS steel shows a bimodal grain size structure with average sizes about 1.7 μm of coarse grains and 250 nm of ultrafine grains

(based on a statistic of 230 grains total, grain size ≥900 nm was taken as coarse grains, others as ultrafine grains). The black dots located at grain boundaries are Cr rich oxides. The grain boundaries as a high diffusion path can accelerate the growth of the particles. The enrichment of Cr in the particle led to the depletion of Cr content near it, which deteriorated the corrosion resistance of the matrix around and thus made the corrosion property non uniform. Holes are present at the interfaces between the particles and matrix. Fig.6.2 (b) is the STEM image giving the chemical contrast of the same region. The Cr rich oxides should show darker contrast for the relatively low atomic number. But the higher thickness caused by the corrosion properties enhance the elastic scattering of the electrons and also a short distance to the detector. These factors made the contrast of the particles brighter. The as-HIPped 04H ODS sample has a similar bimodal structure as shown by the representative TEM micrograph in Fig.6.3a. The average size of coarse grains is about 2.5 μm and the maximum grain size is ~ 8 μm. The surrounding ultrafine grains are 400 ~500 nm in diameter.

Significant refinement of large grains was observed after ECAE. For example, a newly formed grain is clearly surrounded by small grains as shown in Fig.6.2c. Coarse grains of 04H were effectively refined to below 2 μm and all grains became more equiaxed as shown in Fig.6.3b. When applying route B at the same temperature (2B700), although the same amount of strain was introduced into the specimen, some even smaller grains were identified in Fig.6.2d. But the refinement is not as uniform as the route C case in 03H ODS steel. Some non- equilibrium grains are observed in the 04H 2B700 specimen. The volume fraction of non-equilibrium grain boundaries and fine grains is

greater as shown in Fig.6.3c. 03H processed at 300°C got shear localized. However, 04H was successfully processed at a low processing temperature. After processing via 04H 1A300, a smaller grain size was achieved (Fig.6.4d) compared to that in 04H 2B700.

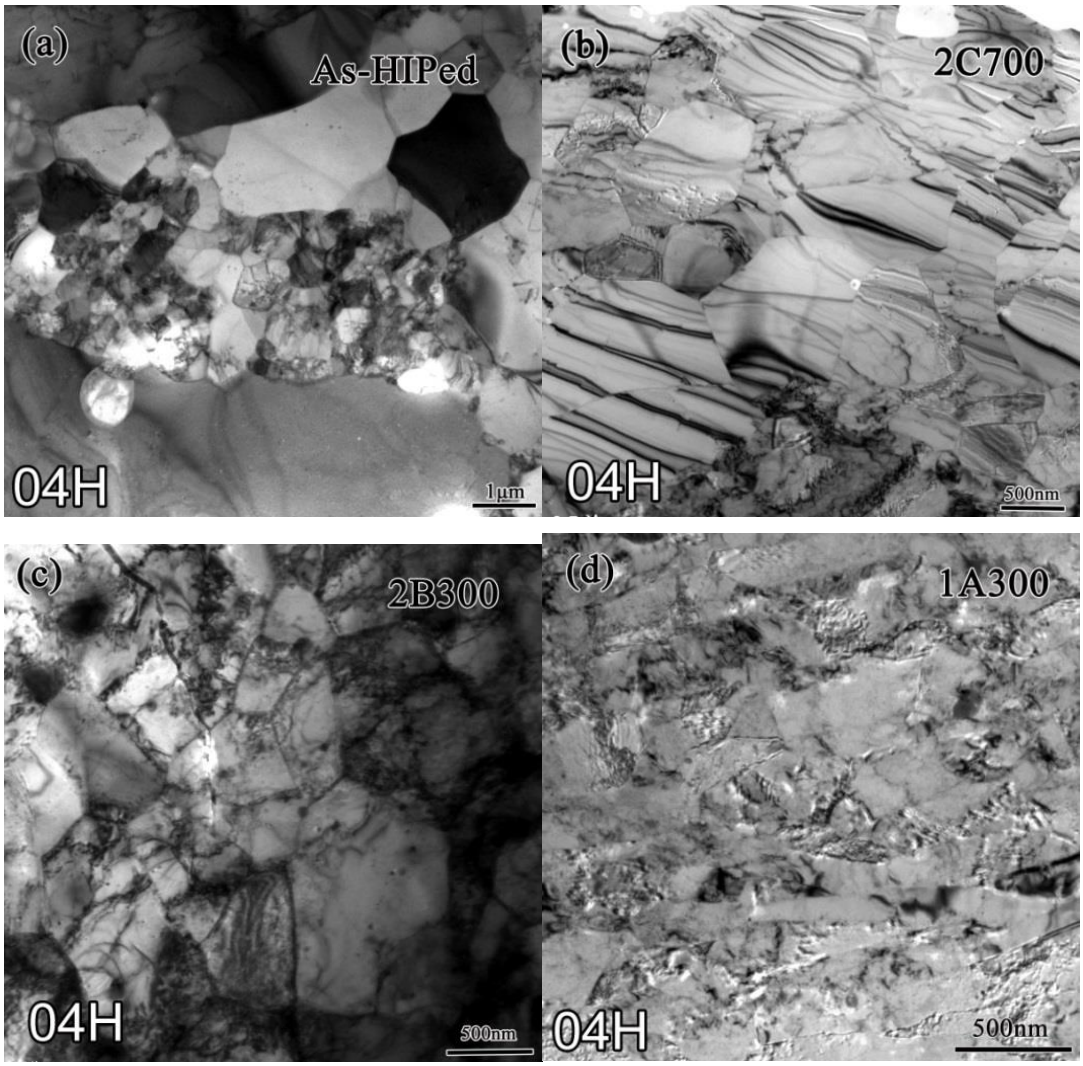

Figure 6.3 (a) Bright field TEM micrograph of as-HIPped 04H ODS steel having a similar bimodal structure with larger grains of several microns and puddles of small grains of ~ 460 nm in diameter. (b-d) are TEM micrographs of ODS steel following 2C700, 2B700, and 1A300 ECAE processing conditions.

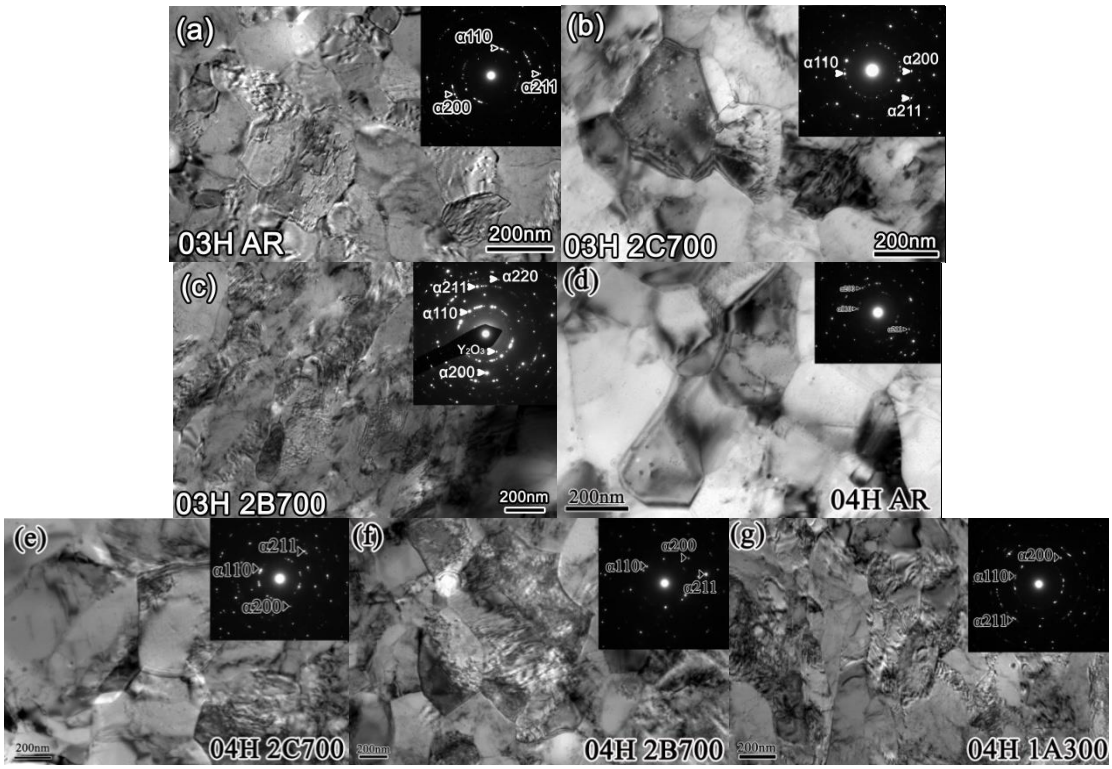

Figure 6.4 Comparisions of ultra-fine grains (UFG) in as-received and ECAEed 03H and 04H ODS steel. (a,d) The UFG grains in 03H AR and 04H ARsteel exhibit relatively low density of dislocations within the grains. (b,e) Some grains within the UFG regions begin to recrystallize after the 2C700 process. (c,f,g) The dislocation density increases significantly in the UFG region after 2B700 process and 1A300 process in 04H. The grains are sheared due to the intensive stress. Diffraction spots from Y_2O_3 partices are noticed.The inserted select area diffraction (SAD) patterns show that the ODS steels subjected to ECAE processing have a predominant BCC structure.

In the ultrafine grain zone, shown in Fig.6.5, grain refinement is not as pronounced. However, the density of dislocations in grains significantly increased (Fig. 6.5b-c, e-g). Also, a greater fraction of high-angle grain boundaries was observed in the 03H 2B700 and 04H 1A300 materials as shown by discontinuous rings in the inserted SAD patterns. The d-spacing measurement shows that this steel has a predominantly BCC structure, which confirms the earlier XRD results.

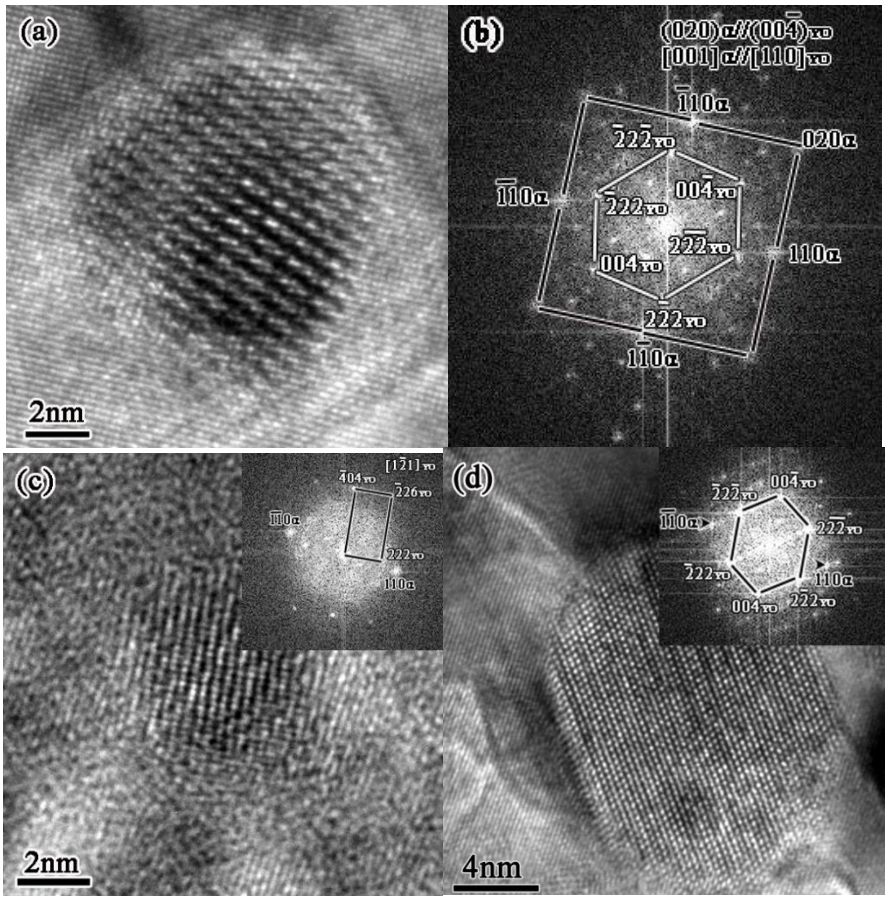

Figure 6.5 HRTEM images of nanoscale oxide particles in the as-HIPped alloy: (a) a medium-size spherical Y_2O_3 particle, about 8 nm in diameter with corresponding (b) FFT pattern shows the orientation relationship between the Y_2O_3 particle and matrix. The zone axis of the oxide particle is [110]. (c) A 4 nm oxide nanoparticle indexed as Y_2O_3 examined along its [1-21] zone axis; and (d) a larger faceted oxide particle examined along the same zone axis as the oxide particle in (a) revealed clear phase boundaries between oxide and matrix.

6.1.2 Particles structures

HRTEM examination was performed to determine the crystalstructure of the oxide particles in 04H ODS. As shown in Fig.6.5a, many oxide nanoparticles appear spherical with diameters of ~ 8 nm. Fast Fourier transform (FFT) of the micrograph, in Fig.6.5b, shows that the oxide particle had a BCC Y_2O_3 structure with a lattice parameter of 1.06 nm. The diffraction spots near the central beam are from the secondary diffraction of the matrix spots. The orientation relationship between the crystalline oxide

particles and the matrix (denoted as α phase) derived from FFT patterns were determined to be $(020)_{\alpha}$ // $(00\bar{4})_{Y2O3}$ and $[001]_{\alpha}$ //$[110]_{Y2O3}$. Smaller and larger oxide particles were also characterized. Many larger oxide particles (Fig.6.5d) had a faceted shape rather than the spherical shape of smaller particles. The corresponding FFT patterns show a crystal structure similar to the medium sized particles. The tiny oxide particles are similar in the 03H ODS steel.

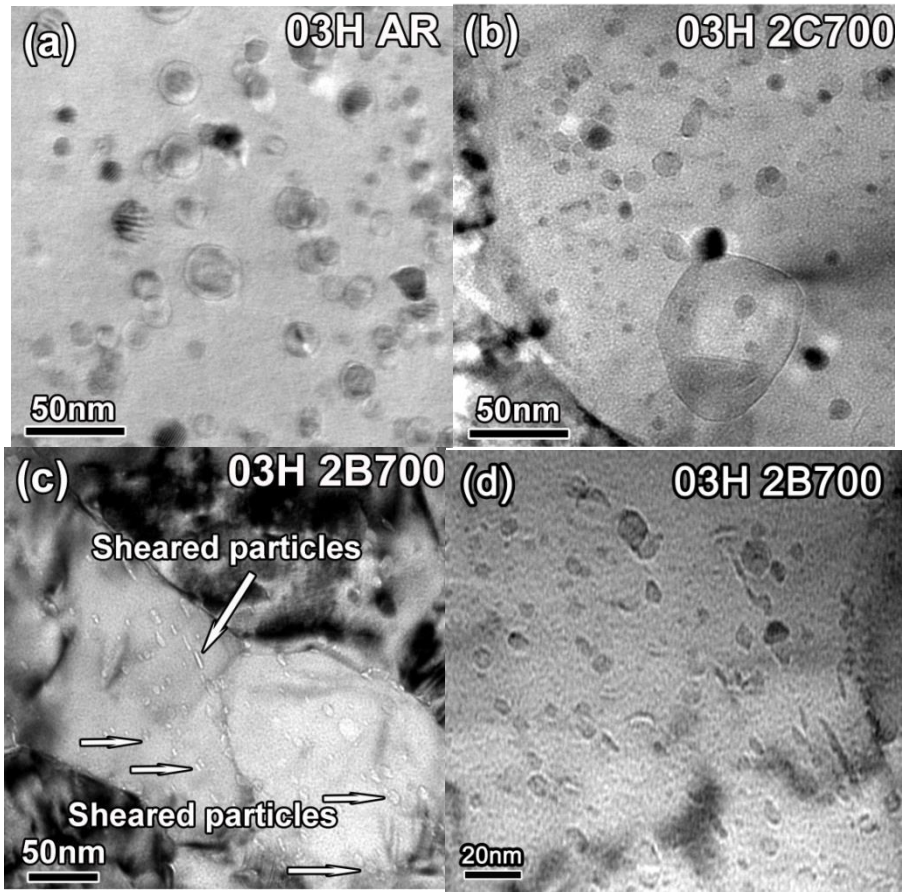

Figure 6.6 Compariation of tiny oxide particles in AR and ECAEed ODS steels. (a) In the AR ODS steel, a core-shell structure and bi-phase particles are observed. (b) The 2C700 specimen shows simple and complex particles. (c) Deformed and sheared particles were observed in the 2B700 ODS steels due to the intense shear stress.(d) Numerous oxide particles are deformed via shear stress after ECAE

Fig.6.6a shows that the oxide particle distribution within a grain in 03H ODS steel. The oxide particles are uniformly distributed within the grains. In the 03H 2C700 specimen (Fig.6.6b), some large particles with a complex structure are observed. The growth of new particles such as Cr oxide can take the preexisting Y_2O_3 as a nucleation site. Several oxide particles were sheared by the intensive shear stress of ECAE as shown Fig.6.6c-d. The second pass of route B is sufficient for same particles to shear in particular directions.

Fig.6.7a shows that oxide particles of 04H ODS steel are also well distributed inside certain grains of the as-HIPped specimen. Other types of precipitates (Cr rich oxide particles) as indicated by circles are also observed. A non-uniform distribution of the oxides within other larger grains is also observed. For instance, numerous oxide particles are arranged preferentially along grain boundaries in the prior ultrafine grain region (Fig.6.7b). After ECAE at 700 °C, oxide particles are more uniformly distributed inside grains as shown in Fig.5c. When applying single pass ECAE at a lower temperature, 300 °C, triangular or elliptic shaped oxide particles are observed as marked by arrows in Fig.6.7d.A close examination of oxide nanoparticles shows that their structure remained BCC Y_2O_3 with a lattice parameter of 1.06 nm as shown in Fig.6.8a. Some of the oxide nanoparticles tended to evolve into smaller particles (Fig.6.8b) similar to the case of 03H after 2B700.

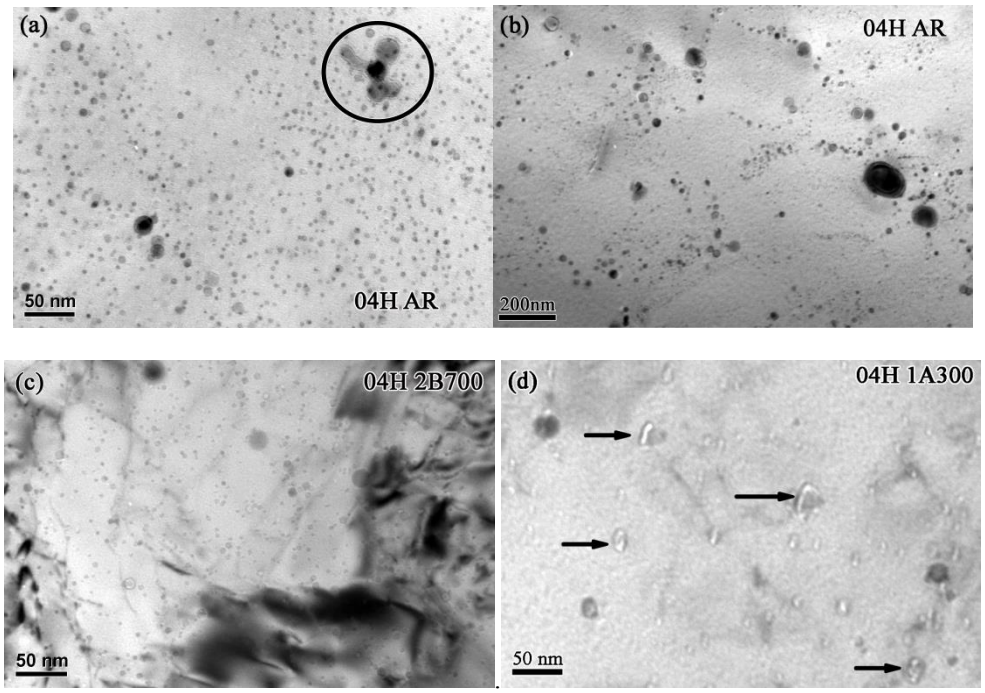

Figure 6.7 TEM micrographs show that (a) oxide particles are randomly distributed in the 034H AR ODS steel. (b) Oxide particles decorate the grain boundaries of prior ultra-fine grains in as-HIPped specimen. (c) After ECAE (2B700), oxide particles are more uniformly distributed throughout grains. (d) Numerous oxide particles in ECAE processed samples (1A300) are deformed via shear.

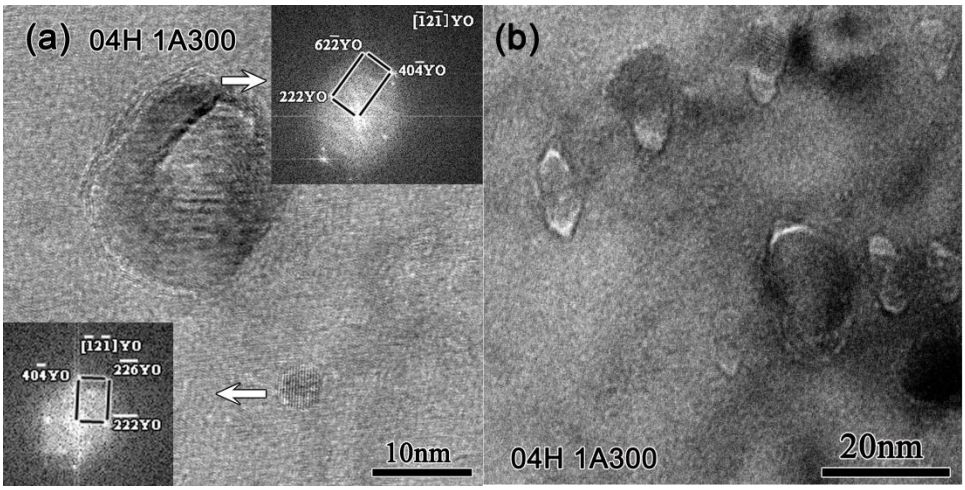

Figure 6.8 (a) HRTEM images of nanoscale oxide particles in specimen 04H 1A300. The FTT patterns (upper-right from the 20 nm and lower-left from the 5 nm diameter Y_2O_3 oxides) show that the oxide particles remain BCC in crystal structure (zone axis along [-12-1]). (b) Numerous oxide nanoparticles are deformed by shear stress.

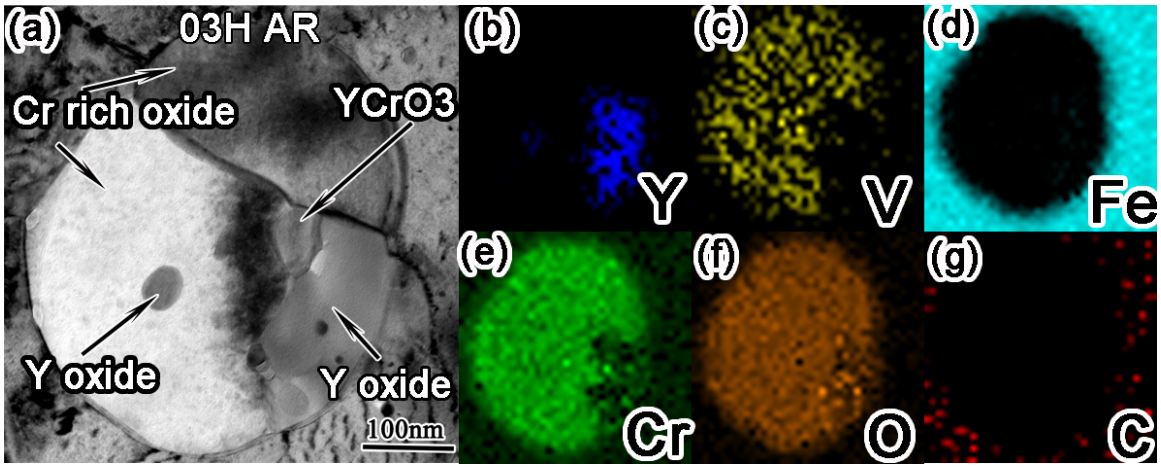

Figure 6.9 (a) TEM micrograph of complex oxide particles in as-HIPped 03AR ODS steel with (b-g) corresponding STEM elemental mappings of Y, V , Fe, Cr, O and C.

Other types of precipitates were investigated further in the 03H AR and 04H AR specimens. Fig.6.9 shows the bright field image of a complex, cut-open oxide particle in 03H ODS steel and corresponding elemental mappings. This particle was located at a grain boundary. The center is found to be a $YCrO_x$ type particle with all of its edges surrounded by Cr rich oxide or Y rich oxide. The two Cr rich particles were detected with similar chemical composition but different orientations. V was also detected within the Cr rich particles. In the Y rich oxide particles, a small amount of Cr was also detected. None of the elements C, Fe, Ta and W were detected within the particles.

Fig.6.10 shows a “palm like” precipitate in 04H AR ODS tilted to a perfect [110] zone axis. This precipitate has an FCC structure with a lattice parameter of 1.07 nm as confirmed by the inserted SAD pattern. A STEM image of the same location is shown in Fig.6.10b. Chemical analysis (Fig.6.10c) reveals that the precipitate has the stoichiometry of $(Cr, Fe)_{23}C_6$. Other Cr rich oxide particles were also detected. As shown in Fig.6.11a (TEM) and 6.11b (STEM mode), a larger particle with ellipsoidal shape was

identified with the shorter dimension of ~ 500 nm. According to the EDX line scan result, Fig.6.11c, the particle is a Cr rich oxide similar to the 03H AR ODS case but without “cutting open”.

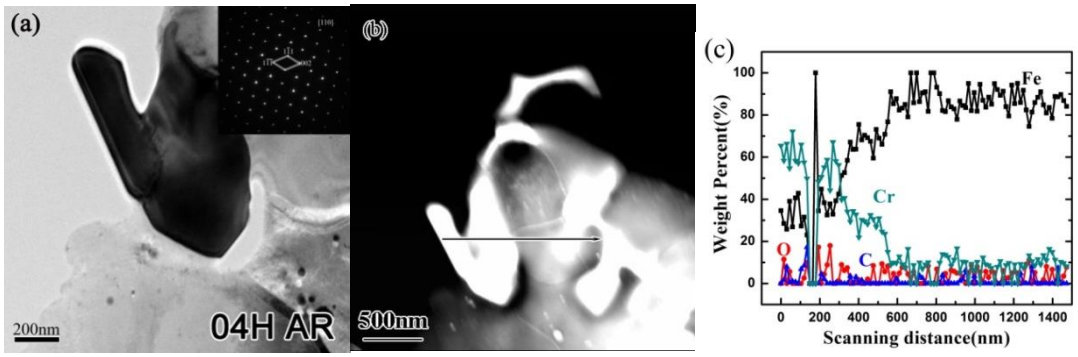

Figure 6.10 (a) Bright field TEM image and the corresponding SAD pattern of $(Cr, Fe)_{23}C_6$ particles in 04H AR ODS steel; (b) STEM image of the same region and (c) the corresponding compositional profile along a line scan (black line in (b)) showing chemical composition changes along this line.

The enrichment of Cr inside the particle led to the depletion of Cr in surrounding matrix. The same type of particles were also investigated by SEM (after selectively etching by KOH solution) as shown in Fig.6.11d in order to obtain statistical distribution information of particle sizes. No pronounced geometry change is observed for the Cr oxide particles and Cr carbides after ECAE according to the SEM results (not shown here). Similar SEM images in the 03H ODS steels are also given in Fig.6.12.

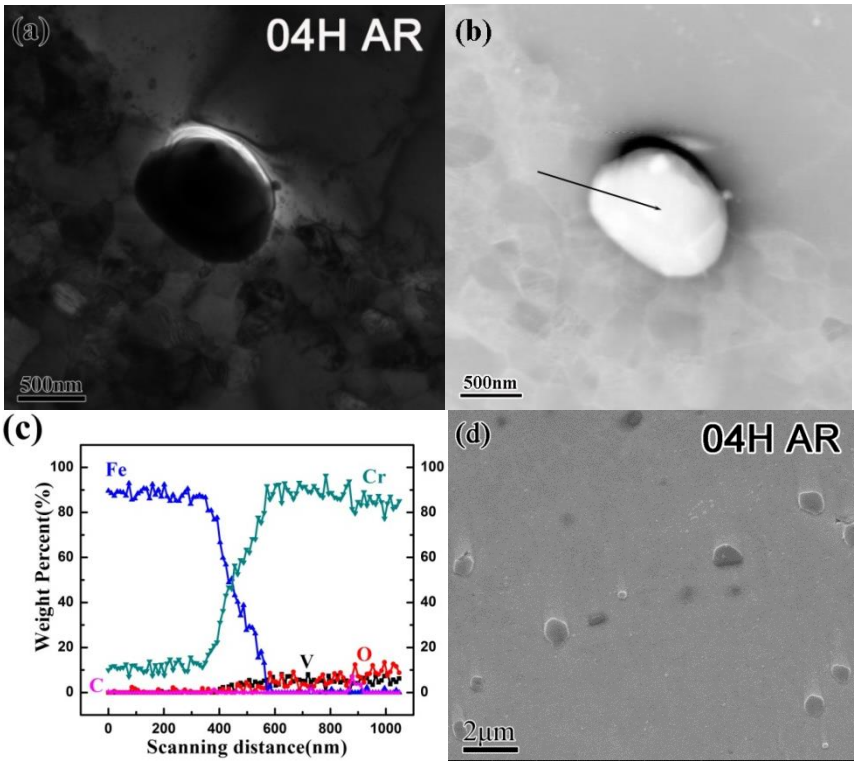

Figure 6.11 (a) TEM micrograph of a large oxide particle in as-HIPped alloy with corresponding (b) STEM image.(c) The line scan along the black line in (b) shows that the particle is depleted in Fe, and enriched with Cr and contains V and O. (d) SEM micrograph shows that after KOH solution treatment, Cr rich particles are selectively etched.

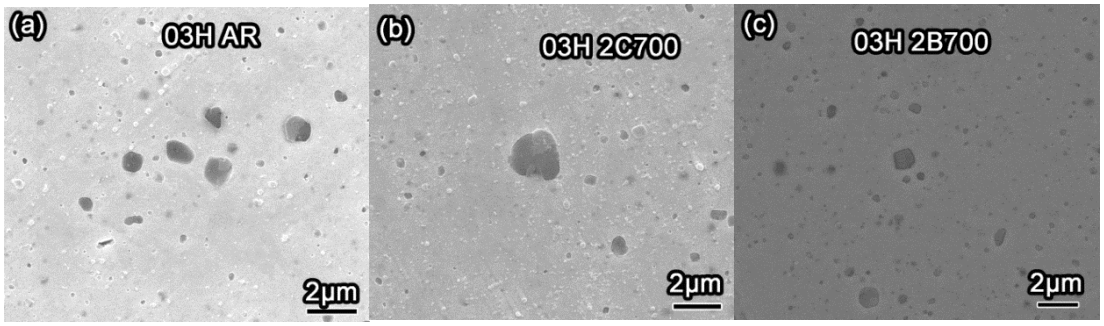

Figure 6.12 SEM micrograph shows that after KOHsolution treatment, Cr rich particles (black dots) are selectively etched in as-received and ECAEed ODS steel (a) AR and (b) 2C700 and (c) 2B700

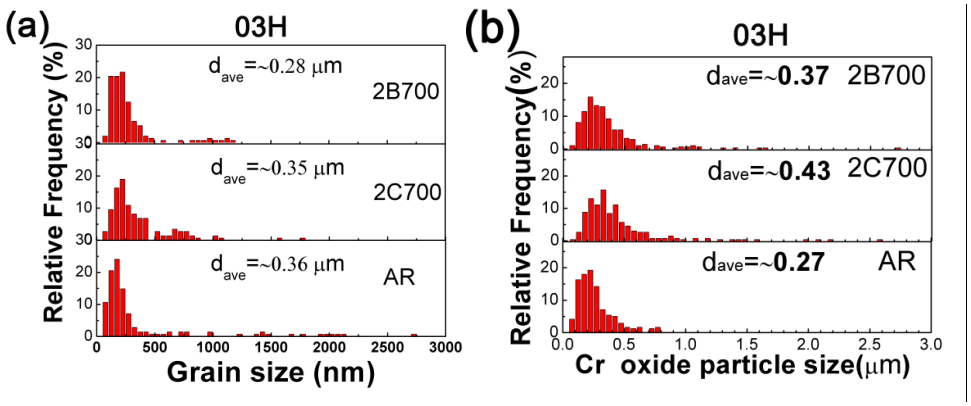

Figure 6.13 (a) Grain size and (b) large oxide particle size distribution before and after ECAE in 03H ODS steel. The grain refinement mainly occurred for larger grain sizes. However, the large oxide particles coarsen during ECAE.

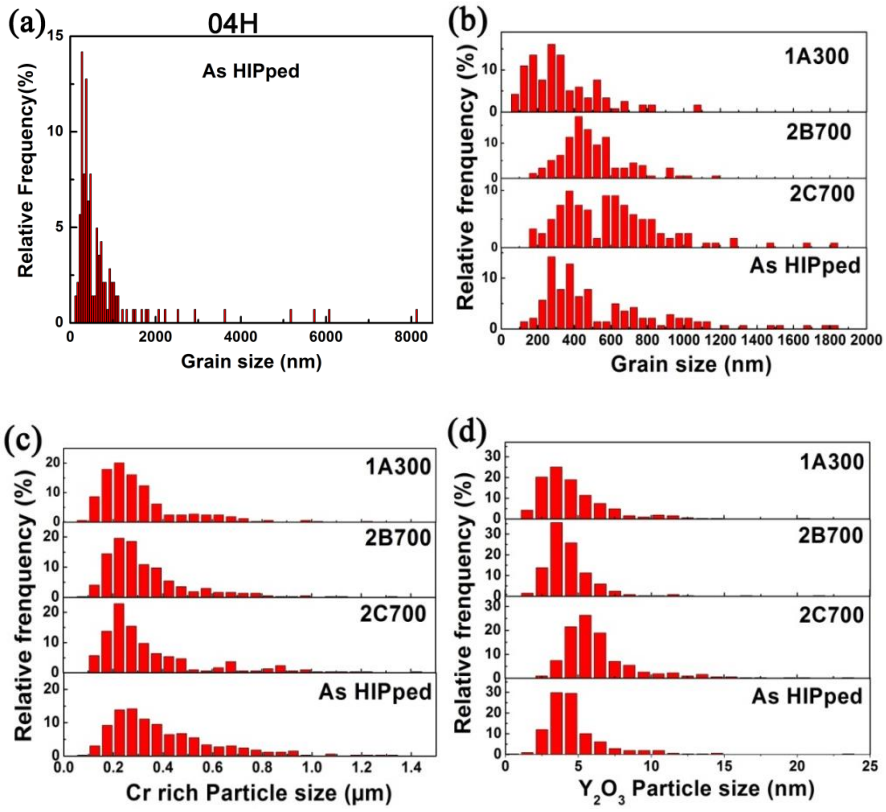

Figure 6.14 Grain and particle distributions in as-HIPped and ECAE processed 04H ODS alloys. (a) Grain size distribution in as-HIPped sample shows that grains as large as 8 μm exist after consolidation. (b) Grain size distributions show grain refinement after ECAE processing. (c) Cr rich particles are also refined after ECAE. (d) Insignificant variation of distribution of Y_2O_3 oxide particles after ECAE except that the average particle size appears to increase slightly in the 2C700 specimen.

6.1.3 Statistic results of the refining effect

Statistical analyses of the microstructure were carried out to determine the size distribution of grains and particles. Fig.6.13 shows the grain size and particle size distribution acquired by TEM and SEM analysis of 03H ODS steel. The grain size is not refined much by the route C at 700°C. However, the grain size was slightly refined after route B processing. Grains as large as 3 μm in the 03H AR specimen are refined to below 2 μm or even smaller. The grain size of small grains was not changed much.

Figs.6.14a and b show grain size distributions determined from TEM micrographs by using the linear intercept method. More than 140 grains were analyzed for each case. Grains as large as 8 μm existed in the as-HIPped alloy. Processing via route 2C700 refined the maximum grain size to less than 2 μm. In the 1A300 specimen, no grains larger than 1.2 μm were observed. The refinement of larger Cr rich particles by ECAE was also noticed from Fig.6.14c which shows the statistical distribution of ~ 360 Cr rich particles based on SEM studies. Fig.6.14d shows TEM based measurements of the size distribution of ~ 320 Y_2O_3 nanoparticles in specimens processed under different conditions. The 2C700 specimen had slightly greater Y_2O_3 particles. Details of microstructural features are given in Table 6.1. These dispersion factors are given to enable calculation the dispersion strengthening in a later section. The average grain size of the matrix was reduced by a factor of two after processing via 1A300. In addition, both the size and volume fraction of Cr rich oxide particles are reduced by ECAE processing. The density of oxide particles was little affected, and is on the order of $10^{22}/m^3$.

Table 6.1 Evolution of microstructural features of 04H ODS steel after ECAE.

Alloy ID	Grain		Cr rich phase ($M_{23}C_6$ and Cr oxides)			Y_2O_3 nanoparticles	
	Average size(μm)	Maximum size(μm)	Average size (μm)	Volume fraction (%)	Density (m^{-3})	Average size(nm)	Density(m^{-3})
As-HIPed	0.77±1.09	≥8	0.40±0.22	2.31±1.31	2.8×10^{16}	4.7±2.3	3×10^{22}
2C700	0.60±0.29	2	0.35±0.23	1.53±0.68	2.5×10^{16}	6.5±2.9	
2B700	0.50±0.17	1.2	0.33±0.18	1.47±0.51	3.4×10^{16}	4.4±2.0	
1A300	0.33±0.19	1.2	0.30±0.17	1.25±0.31	3.8×10^{16}	4.6±2.4	

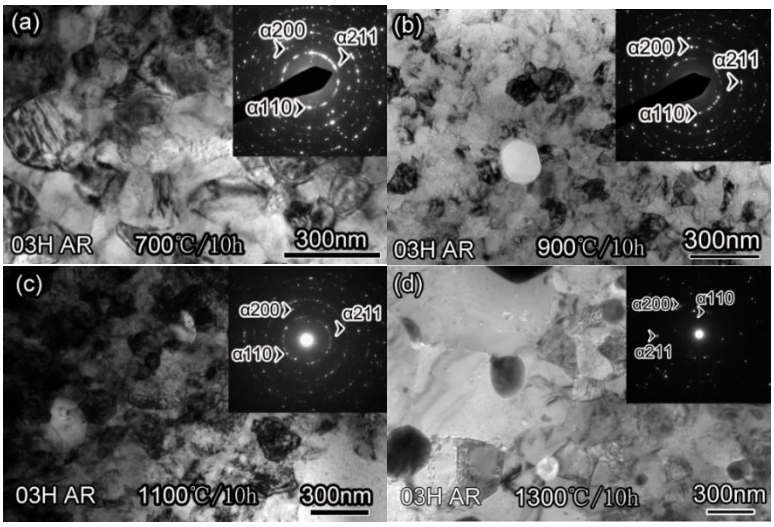

Figure 6.15 TEM micrograph shows the thermal stability of the UFG region in 03H AR ODS steel. (a)700℃/10h (b) 900℃/10h (c)1100℃/10hand (d)1300℃/10h. Significant coarsening occurs above 1100℃.

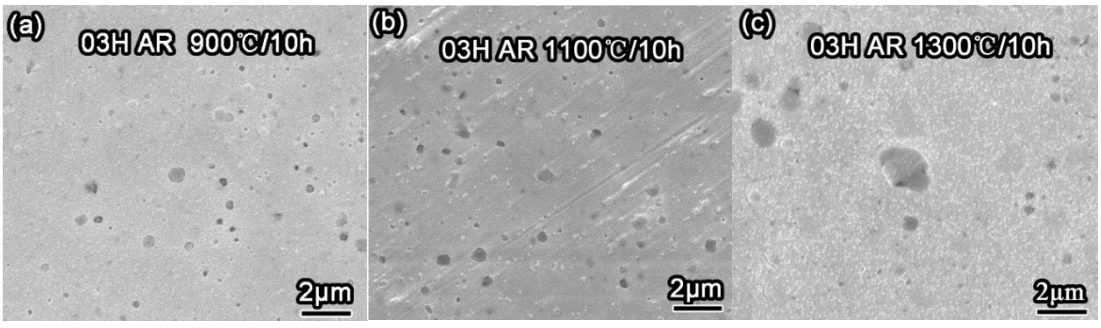

Figure 6.16 SEM micrograph shows that Cr rich particles (black dots) are selectively etched in AR samples after annealing (a) 900℃/10h (b)1100℃/10h and (c)1300℃/10h

6.2 Thermal stability of ODS steels

Fig.6.15 shows TEM images of 03H AR ODS steel subjected to high temperature annealing for 10 hours. The image is focused on the UFG region. Grains coarsen at 1300°C during 10h annealing. Large black particles show up, which are presumably Cr oxides that nucleated at the tiny yttrium oxide particles. The large Cr oxide particles also coarsened at the 1300°C as shown in Fig.6.16.The boundaries of the particles show a feature indicating dissolution. Statistical results show that the particles increase in size by around 50% at 1300°C as shown in Fig.6.17.

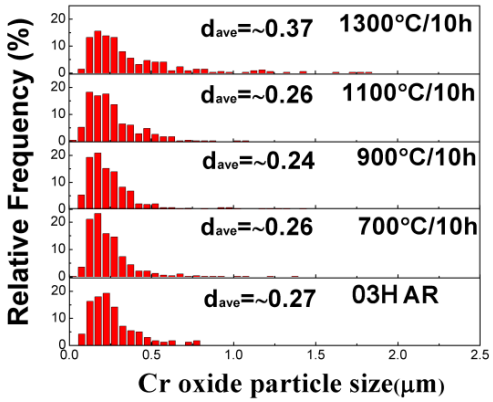

Figure 6.17 Large oxide particle distribution after annealing at elevated temperatures.

Fig.6.18 shows small oxide particles. In the as-HIPped state, as shown in Fig.6.18a, few Janus particles were observed. A core-shell structure of these oxide particles is frequently observed in the ECAEed ODS steel shown in Fig.6.18b-c. HRTEM images in Fig.6d show that these two particles form a straight coherent boundary. The upper part is a $YCrO_3$ complex oxide with a tetragonal structure. Indexing of the lower part reveal a structure is close to that of Cr_8O_{21}.

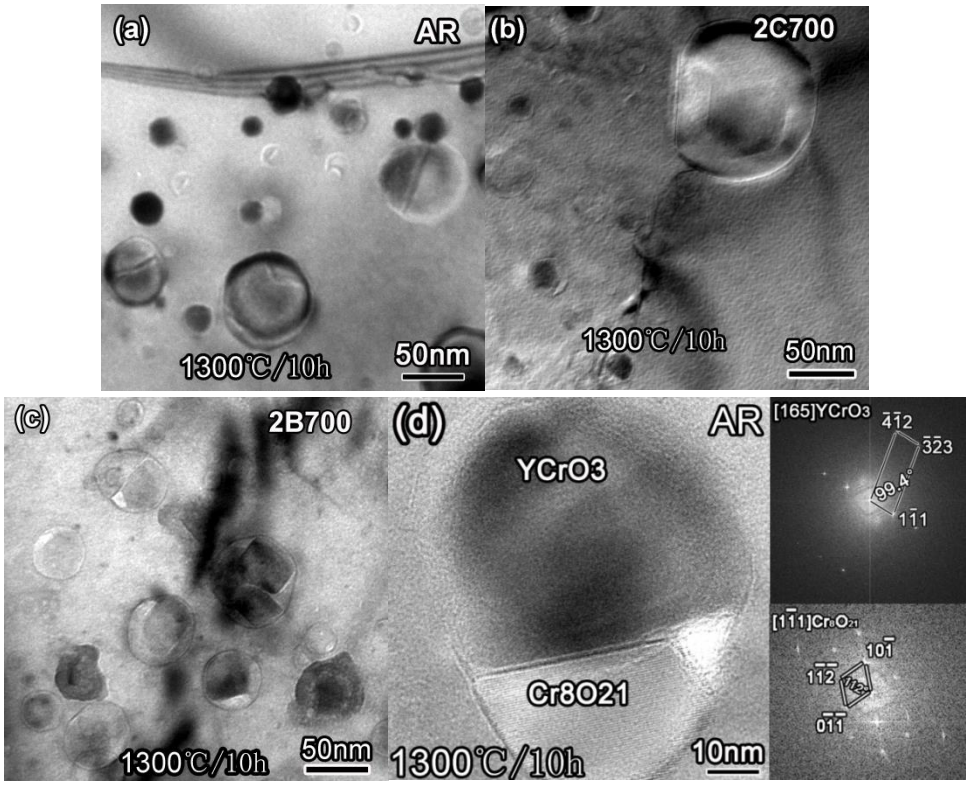

Figure 6.18 The formation of complex particles after annealing at 1300℃/10h under various processing conditions (a) More bi-phase particles are observed in the AR specimen.(b) 2C700 showsa core-shell structure.(c) A core-shell structure and other forms of complex particles were identified in the 2B700 ODS steel.(d) HRTEM image of AR with corresponding FFT. The upper particle is indexed a $YCrO_3$ [165] axis, which indicate an orthorhombic structure; the lower particle can be indexed as Cr_8O_{21} [111] axis, which is a triclinic structure.

Statistical results in Fig.6.19 show that the tiny oxide particles start to coarsen at 1100℃ after 10 hours annealing. Significant coarsening was observed after 1300℃annealing. The tiny oxide particles in the ECAEed 03H ODS steels seem to coarsen faster than the AR ODS steels.

Fig.6.20 shows that thermal stability of the ODS steels. The 03H ODS steels start to recrystallize at around 1100°C. After ECAE, the recrystallization temperature starts at ~900 °C in 03H 2B700 specimen. 04H ODS steel tends to recrystallize earlier than 03H

ODS steel. Especially, the 04H 1A300 starts to recrystallize at a temperature of 700°C. The general hardness of 03H is higher than that of 04H steels.

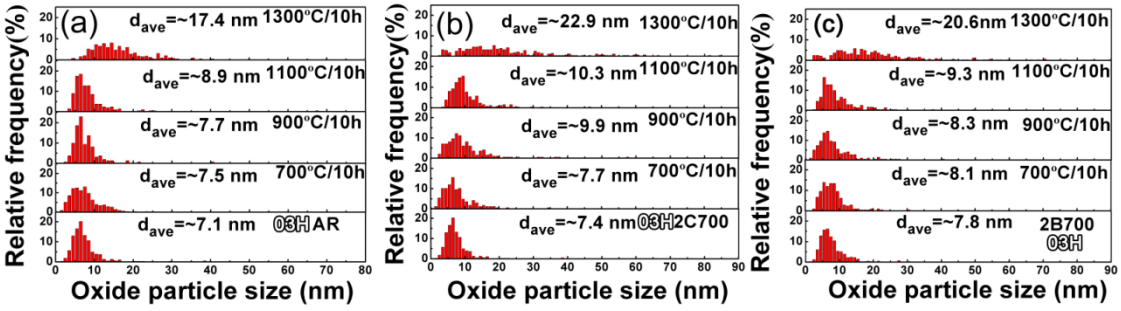

Figure 6.19 Oxide size distribution in 03H ODS (a) AR and (b, c) ECAEed ODS steels after post annealing at elevated temperature. Significant coarsening occurs after 1100°C. The oxide particles in ECAEed materials coarsen faster than the AR condition.

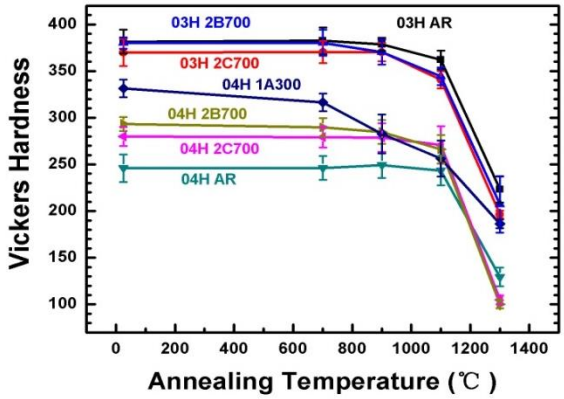

Figure 6.20 Evolution of Vickers hardness of processed ODS steels after annealing for 10h. The hardness of ECAE processed samples remains unchanged up to 900°C/10h, followed by significant softening at higher annealing temperatures.

6.3 Related mechanisms

6.3.1 Microstructure and Multi-scale refinement achieved by ECAE

Bulk materials with bimodal grain sizes can be produced by recrystallization of

cold worked metallic materials, or consolidation of powders with a mixture of large and small grain size [204]. Zhao *et al* successfully fabricated bimodal ODS steel by using blended powder of different sizes [205]. In the present study, large grains were observed probably because of abnormal grain growth during HIPping at 1150 °C. No bimodal structure was observed in EUROFER ODS steel by Lindau *et al*[36]. This is likely because their alloy was prepared from gas atomized master alloy, a process that may give less phase segregation. The consolidation temperature is greater than the recrystallization temperature and thus lead to the bimodal structure.

The average diameter of Y_2O_3 particles in the 04H ODS material in this study (~ 4.5 nm) is slightly greater than what was observed in previous work (≤ 3 nm) [40, 206, 207]. The average particles size in 03H ODS is even larger. This may be related to the absence of Ti in the current ODS steel. Titanium is apparently beneficial to the formation of smaller oxide nanoparticles [48]. The orientation relationship between the matrix and Y_2O_3 particles in the present study is $(020)_{\alpha}$ // $(00\bar{4})_{Y2O3}$ and $[001]_{\alpha}$ // $[110]_{Y2O3}$. This is similar to previous studies on an FeAl based ODS alloy although the matrix (FeAl) in that system had a CsCl structure, which is different from the present BCC structure [208]. Klimiankou *et al* showed a somewhat different orientation relationship in EUROFER97 ODS, that is $[111]_{FeCr}$//$[110]_{Y2O3}$ and $(1\bar{1}0)_{FeCr}$//$(1\bar{1}\bar{1})_{Y2O3}$ [52]. These orientation relationships were developed during the HIPping process as a means to minimize the interface energy between the oxide particles and matrix [52].

The formation of $M_{23}C_6$ is inevitable because of the contamination of carbon from the balls and vials used in the MA process. The $M_{23}C_6$ phase was also observed by

Klimiankou *et al.*[209] after heat treatment of a similar alloy. $(Fe, Cr)_{23}C_6$ can lower the ductile-to-brittle-transition-temperature (DBTT) of the alloys.

The effect of ECAE on microstructural refinement of the present ODS steels is summarized as follows. First, the maximum grain size was successfully reduced from several microns to ~ 1 μm, and a smaller average grain size with a more uniform distribution was achieved in 04H 2B700 or 04H 1A300 specimens. The grain refinement in the 03H ODS steel is not significant, which will be discussed later in this chapter. The low temperature extrusion (04H 1A300) was more effective in grain refinement than the high temperature (04H 2C700 and 04H 2B700) process, even though less strain was applied. ECAE at 700 °C might have triggered dynamic recrystallization that led to concurrent grain growth during extrusion. There are two peaks in the grain size distribution chart of the 2C700 samples (Fig.6.14b). The first peak, ~ 375 nm in average grain size, may arise from the original ultrafine grains in the as-HIPped material. The second peak, ~ 600 nm in average grain size, may originate from refinement of the larger grains in the as HIPped materials.

Second, the average dimension of Cr rich precipitates ($M_{23}C$ and Cr oxides) was refined and their volume fraction was significantly reduced by ECAE. The refinement of precipitates strongly suggests that ECAE is an effective route to redistribute solute, remove precipitates to some extent, and achieve a more homogeneous microstructure. No fractured particles were observed in the 04H ODS study. In fact fractured particles induced by ECAE were rarely observed except for particular shaped particles which had a large stress concentration factor [79].

Third, ECAE appears to change the distribution and geometry of small Y_2O_3 nanoparticles. The oxide nanoparticles were not uniformly distributed in the as-HIPped material. Numerous oxide nanoparticles were found surrounding ultra-fine grains. This is because the oxide nanoparticles were mechanically mixed with larger metal powders during milling, and hence were not fully incorporated uniformly throughout the metal grains even after long duration mechanical alloying. After ECAE, however, most of the oxide particles were found to be distributed uniformly throughout the matrix. Furthermore, the shape of numerous oxide particles in the 04H 1A300 samples was found to be ellipsoidal, implying that large shear stress induced by ECAE may lead to morphology changes of tiny oxide nanoparticles. Although the average particle size appeared intact in 04H 1A300 specimens, in numerous cases, oxide nanoparticles appeared to be "decomposed" into smaller particles (Fig. 6.8b). The tiny oxide particles were sheared open in 03H 2B700 specimens. This phenomenon was not observed everywhere, which may imply that the shear of the particles requires some special conditions. Factors that may influence this phenomenon include the size of the particles and the direction of the grain. In some case, the grain requires a much higher stress tp shear between its orientations. Particles within these grains may be sheared and fractured.

6.3.2 Hardening mechanism

Here, the 04H ODS steels is used as an example to show the strengthening mechanism operated in the ODS steel. Fig.6.21 shows a Hall-Petch plot, i.e. the

dependence of hardness on $d^{-1/2}$, where d is the average grain size. The hardness increased from 2.4 (as-HIPped) to 3.2 GPa (~35%) after ECAE, and followed a linear relationship with $d^{-1/2}$.

The hardness of ODS steel may be affected by three factors: dispersion strengthening from Y_2O_3 particles, the presence of the Cr rich phase, and dislocation pile-ups due to grain refinement (Hall-Petch relationship [210]). The yield strength σ_y of ODS steel can be estimated by:

$$\sigma_y = \sigma_0 + \sigma_p + kd^{-1/2} \qquad \text{Eq.6.1}$$

where σ_0 is the lattice friction strength (also the yield strength of coarse grained material), and σ_p is the dispersion strengthening contribution. The last term arises from Hall-Petch dislocation pile-ups, wherein, k is the resistance of grain boundaries to dislocation propagation, and d is grain size.

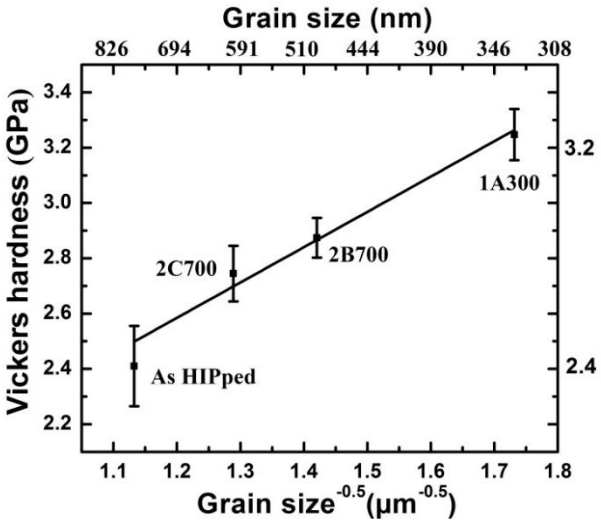

Figure 6.21 Hall-Petch plot of ODS steel with an average grain size varying from 300 to 800 nm. Grain refinement through ECAE leadsto strengthening of the ODS steel.

First, we will estimate dispersion strengthening based on the Orowan bowing mechanism. For simplicity we assume the system is a simplified Fe-Y_2O_3 alloy in which Y_2O_3 nanoparticles are uniformly distributed and the solid solution has negligible effect on hardening.

Dispersion hardening is then calculated by [211]:

$$\sigma_p = M\tau = (MGAb/2\pi\lambda)[\ln(D/r_0) + B] \quad \text{Eq.6.2}$$

where σ_p is the additional stress induced by dispersion hardening; M is the Taylor factor (=2.733 for BCC iron) [196]; τ is the shear stress for bowing of dislocations; b is the magnitude of the Burgers vector of a full dislocation, and which in BCC Fe can be written as 1/2<111>a (where a is the lattice parameter); A=1 and B=0.7 for an edge dislocation; A=1/(1- ν) and B=0.6 for a screw dislocation. In BCC Fe, b = 0.274 nm, G = 59.7 GPa, and ν = 0.159. G and ν are the shear modulus and Poisson's ratio for the {110}<111> slip system, and are calculated to be $3/[4(S_{11}-S_{12})+ S_{44}]$ and $(2S_{44}-4S_{11}-8S_{12})/(6S_{11}+6S_{12}+3S_{44})$, respectively, where S_{11}, S_{22} and S_{44} are the compliance factors for iron. r_0 is the inner cut-off radius of the dislocation core and is typically in the range of 1~3 b. λ is the inter particle distance on a slip plane, which is given by [191],

$$\lambda = 1.25l_s - 2r_s \quad \text{Eq.6.3}$$

where l_s is the equivalent center to center distance of particles, and r_s is the equivalent average radius of oxide particles. The factor of 1.25 is a conservation coefficient arising from the assumption that the Y_2O_3 particle is a strong barrier, and the dislocation segment would be unstable when interacting with pairs of obstacles with a separation distance above 1.25 l_s [191].

Table 6.2 Parameters for Orowan strengthening by Y_2O_3 nanoparticles

Processing condition	$\bar{r}$(10^{-9} m)	$\overline{r^2}$(10^{-18} m^2)	$\overline{r^3}$ (10^{-27} m^3)	l_s(10^{-9} m)	r_s(10^{-9} m)	f (vol.%)	λ(10^{-9} m)	σ(MPa)	H(GPa)
As-HIPped	4.7	27.7	221	145	4.6	0.47	172	118～184	0.35～0.55
2C700	6.5	50.3	494	183	6.1	0.47	218	101～155	0.30～0.46
2B700	4.4	23.1	163	128	4.1	0.47	152	128～202	0.38～0.61
1A300	4.6	27.6	217	148	4.7	0.47	172	118～185	0.35～0.56

Table 6.3 Parameters for Orowan strengthening by Cr rich phases

Processing condition	$\bar{r}$(10^{-6} m)	$\overline{r^2}$ ($10^{-12}$$m^2$)	$\overline{r^3}$ (10^{-18} m^3)	l_s(10^{-6} m)	r_s(10^{-6} m)	f (vol.%)	λ(10^{-6} m)	σ(MPa)	H(MPa)
As-HIPped	0.40	0.21	0.13	5.43	0.41	2.31	5.96	8～11	24～33
2C700	0.35	0.17	0.12	6.85	0.38	1.53	7.80	6～8	18～24
2B700	0.33	0.14	0.08	5.88	0.33	1.47	6.68	7～10	21～30
1A300	0.30	0.12	0.06	5.79	0.31	1.25	6.61	7～10	21～30

The parameter D is given by equation [211]:

$$D = \frac{2r_s l_s}{2r_s + l_s} \qquad \text{Eq.6.4}$$

where l_s and r_s are estimated by using the following stereological equations [212],

$$l_s = \sqrt{\frac{2\pi\overline{r^3}}{3f\bar{r}}} \qquad \text{Eq.6.4}$$

and

$$r_s = \frac{\pi\overline{r^2}}{4\bar{r}} \qquad \text{Eq.6.5}$$

where $\bar{r}$, $\overline{r^2}$, $\overline{r^3}$ are the average value of r, r^2, r^3, where r is the radius of a particle. f is the volume fraction of particles. For Y_2O_3, the volume fraction of particles was

estimated from the weight fraction given a material density of 5.01 g/cm^3.

The hardness is estimated by [185],

$$H = 3\sigma_y \qquad \text{Eq.6.6}$$

where H is the Vickers hardness and σ_y is the yield strength of the material. A similar estimate of strengthening was carried out for the Cr rich precipitates. Results are given in Tables6.2 and 6.3.

The magnitude of dispersion strengthening arising from Cr rich precipitates is small, and varies from 21 to 33 MPa. The precipitation hardening from oxide particles is substantial, ~ 0.45 GPa. A linear relationship between hardness and the square root of the grain size was observed (Fig.6.21), implying that dislocation pile-up against high angle grain boundaries is the predominant hardening mechanism.

The interception of the hardness plot with the y axis is ~ 1.05 GPa, which is $3(\sigma_0 + \sigma_p)$. The slope is ~ 1.28 GPa·μm$^{1/2}$ with an R square value of 0.97. When multiplied by 1/3 to obtain the approximate equivalent yield strength, k is calculated to be ~ 426 MPa·μm$^{1/2}$, which is comparable to that of iron or steel reported previously [188, 213]. Subtracting the average dispersion strengthening $3\sigma_p$ by oxide particles (~0.45GPa) from the intercept value, we arrive at a hardness of ~ 0.6 GPa, 1/3 of which is the yield strength $\sigma_0$of coarse grained alloy without dispersion strengthening, ~ 200MPa. The Hall-Petch type of hardening mechanism is frequently observed in metallic materials subjected to sever plastic deformation [213, 214]. The smallest average grain size in ECAE processed material is ~330 nm, a range in which abundant pile-up of dislocations remains available for strengthening.

6.3.3 The role of oxygen in ODS steels

The major difference between 03H and 04H is that the oxygen content is higher in 03H than that of 04H ODS steel. The UFG region is less in volume fraction in the 04H than that of 03H AR ODS steel, which may hint that the 03H ODS steel suffers less from recrystallization during the HIP processes. The excess oxygen can react with the Cr within the matrix, form more Cr oxides, and thus increase the volume fraction of oxide particles, which is an inside oxygenation process. This could also explain the high thermal stability after extrusion of 03H ODS steel. Actually, the refining effect of 03H ODS is not significant due to the fact that there is a very small volume fraction of large grains and the ultrafine grains are around the refining limits. Although the grain distribution of 04H ODS steel is also bimodal, the volume fraction of large grains is high. So significant refining occurred in the 04H ODS steel. However, the refinement is a dislocation process, which pumped in a high density of dislocations in both steels. The dislocations within the ODS steel are hard to move because of the pinning effect of the tiny particles. The dislocation around the oxide particles is like “an artery around tumor”, which can assist the growth of the oxide particle upon heating. This analogy can help explain why the thermal stability of deformed ODS steel is commonly worse than that of the AR ODS steels.

6.4 Summary

In this chapter, several important observations related to the ECAEed ODS steel were made. ECAE can effectively refine the grain size, especially large grains. The size of the small grain is around the refining limit so no significant refinement of these was

observed. Oxide particles can be effectively redistributed by ECAE during the ECAE process. Excess oxygen seems to play a key role in the strength and thermal stability of ODS steels, which can retard the recrystallization process. The hardening is calculated to be mainly from the refinement of the grain size in ODS steels.

CHAPTER VII

HEAVY ION IRRADIATION OF UFG T91 STEEL*

In this chapter, we use heavy ion irradiation to simulate neutron irradiation on UFG T91 steel. The UFG T91 steel processed by ECAE was irradiated to a dose of 150dpa, a dose level that will take decades to reach for neutrons irradiation in an operating reactor. The pros and cons of such a method are discussed. The radiation effectson UFG T91 compared to its coarse grained counterpart.

7.1 Basic observation of heavy ion irradiated CG and UFG T91 steels

The CG and UFG materials are denoted as AA and 2B300 specimens, respectively. Fe ions accelerated to 3.5 MeV were implanted into these steels at 450°C. The recrystallization temperature of UFG T91 is ~ 500°C. 450°C was selected for the radiation studies to avoid the complexity caused by grain growth. This particular temperature is also targeted for conditions in current pressurized water reactors (~280-~350°C), and relevant for sodium cooled fast reactors [3]. A defocused ion beam (without rastering) was used during the whole implantation process. Irradiation damage profiles were estimated using SRIM (stopping ranges of ions in matter) by selecting the Kinchin-Pease (K-P) model option, as suggested by Stoller *at al.*[174]. A fluence of 9×10^{20} ions/m^2 was achieved, corresponding to a peak damage of 150 displacements per

*Reprint with the permission from "Response of equal channel angular extrusion processed ultrafine-grained T91 steel subjected to high temperature heavy ion irradiation" by M. Song *et al*, 2014. Acta Materialia, 74, 285-295, Copyright [2014] by Elsevier.

atom (dpa). A 50 nm thick Nb cap layer was sputtered onto the irradiated T91 steels as a marker of the specimen surface.

The CG T91 material shows a typical tempered martensitic lath structure. Carbides are normally positioned predominately along lath boundaries and prior austenite grain boundaries (PAGBs) in the CG T91 as shown in Fig.7.1a. The tempered martensitic lath was refined after the ECAE deformation as shown in Fig.7.1b. During the deformation, the tempered martensitic lath was broken into pieces and became an integral component of the newly formed GBs of UFG grains. The refinement of carbides is insignificant; no broken carbides particles were observed. The CG T91 has dimensions about ~ 0.63 and 3.4 μm along the thickness and length directions, respectively. The UFG T91 contains grains of ~ 154 and 480 nm along the thickness and length directions. Thus, the average grain sizes were estimated as ~ 2 μm and ~ 320 nm for CG and UFG T91.

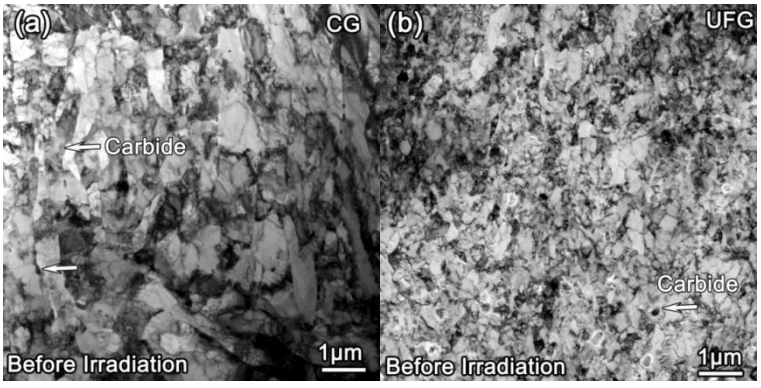

Figure 7.1 Panoramic TEM micrographs comparing the microstructure of CG and UFG T91 steel before irradiation. (a) The CG material exhibits a tempered martensitic lath structure with carbides located at lath boundaries. The average grain size is ~ 2 μm. (b) After ECAP extrusion (2 passes at 300°C following route B), the average grain size is significantly refined to ~ 320 nm. The tempered martensitic laths were also refined and become part of high angle grain boundaries. Carbides are observed sporadically.

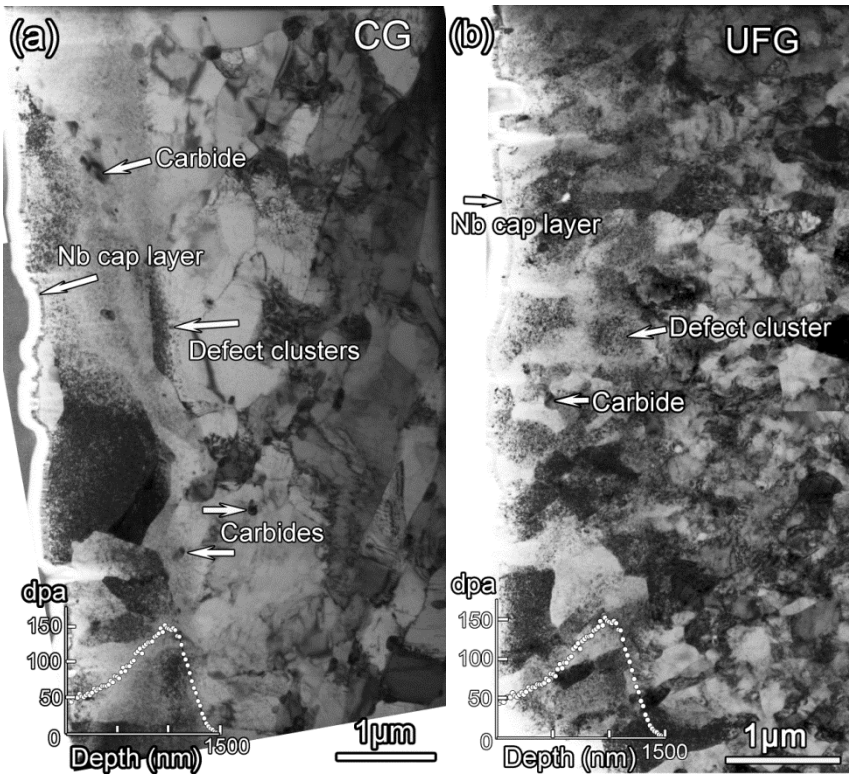

Figure 7.2 Cross-section TEM micrographs that show panoramic views of the microstructures of coarsen-grained (CG) and ultra-fine grained (UFG) T91 steel after Fe ion irradiation up to a maximum of 150 dpa at 450 °C. Depth dependent SRIM simulation of dpa is superimposed on both micrographs. (a) CG T91 is fully tempered and had an average grain size of 2μm with an inherently low dislocation density.(b) UFG T91 steel prepared by equal channel angular pressing has an average grain size of ~ 320 nm with a greater dislocation density. Black dots are defect clusters generated by heavy ion irradiation. The apparent density of defect clusters is dependent on grain orientation. The Nb cap layers were magnetron sputtered onto the irradiated T91 steels as a marker and protection for the specimen surface during the FIB process.

The TEM micrographs shown in Fig.7.2 compare the overall microstructure of CG and UFG T91 after irradiation. The surfaces of specimens were well protected by Nb cap layers. No significant grain growth is noticed after irradiation. Abundant irradiation-induced defect clusters (black dots) are observed in both specimens throughout the irradiation region. The apparent density of "black dots" appears to vary from one grain to the other. This defect density variation arises from different imaging conditions for each grain. These grains have to be tilted to the correct zone axes to reveal the small

black dots in various grains along the projected ion path. We have performed extensive tilting experiments to obtain reliable statistics of defect density in a large number of grains in irradiated T91. Compared to non-irradiated regions, large intragranular carbide particles are noticed after irradiation.

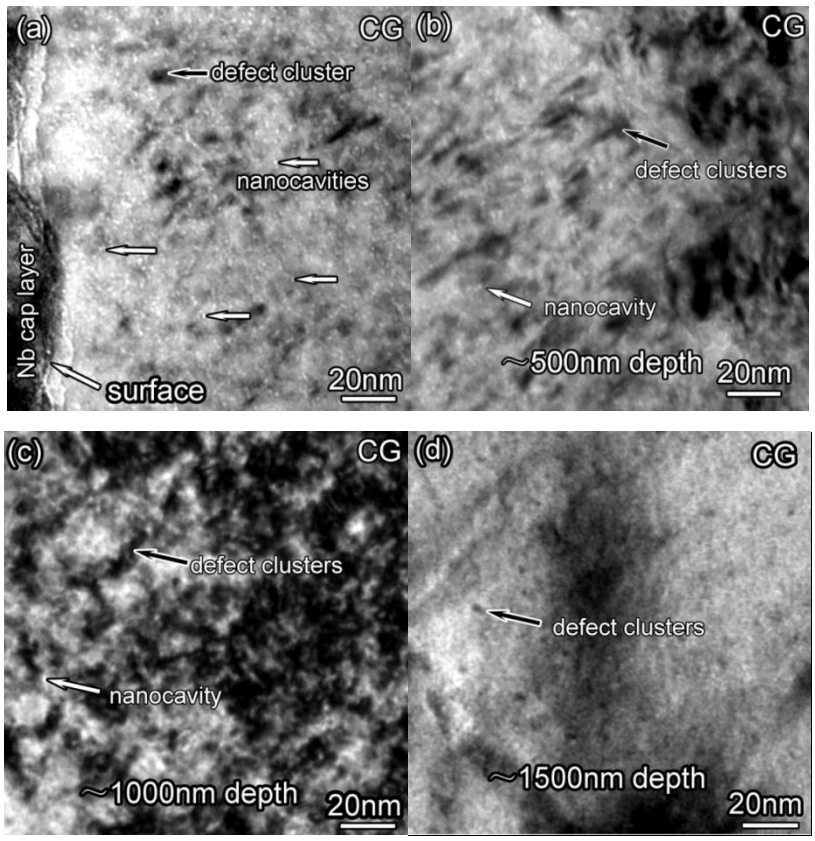

Figure 7.3 Depth dependent distribution of irradiation induced nanovavities in CG T91 steel. (a) In a region close to the surface, abundant nanocaviteis are observed.(b) At ~500 nm from the surface, the density of nanocavities is dramatically lower, but the density of defect clusters (dislocation loops) appears to increase.(c) Within the peak damage zone, ~1000 nm underneath the surface, a high-density of nanocavities and dislocation loops are observed. (d) At the end of the Fe ion projected range, ~1500 nm, the density of both nanocavities and dislocations loops declines. All the images were recorded at an under focus distance of –500 nm.

Nanocavities with an average diameter of 1-2 nm are revealed by the through-focus imaging method. Fig. 7.3 and 7.4 compare the evolution of microstructure at

various similar ion penetration depths in the CG and UFG T91 materials by using TEM micrographs captured at identical under focus distances (-500 nm). In general, the density of nanocavities is high within the surface region and decreases rapidly with an increase of implantation depth. The CG specimen has more nanocavities than that in UFG T91 steel. No defect denuded zone is observed in the vicinity of GBs or the surface.

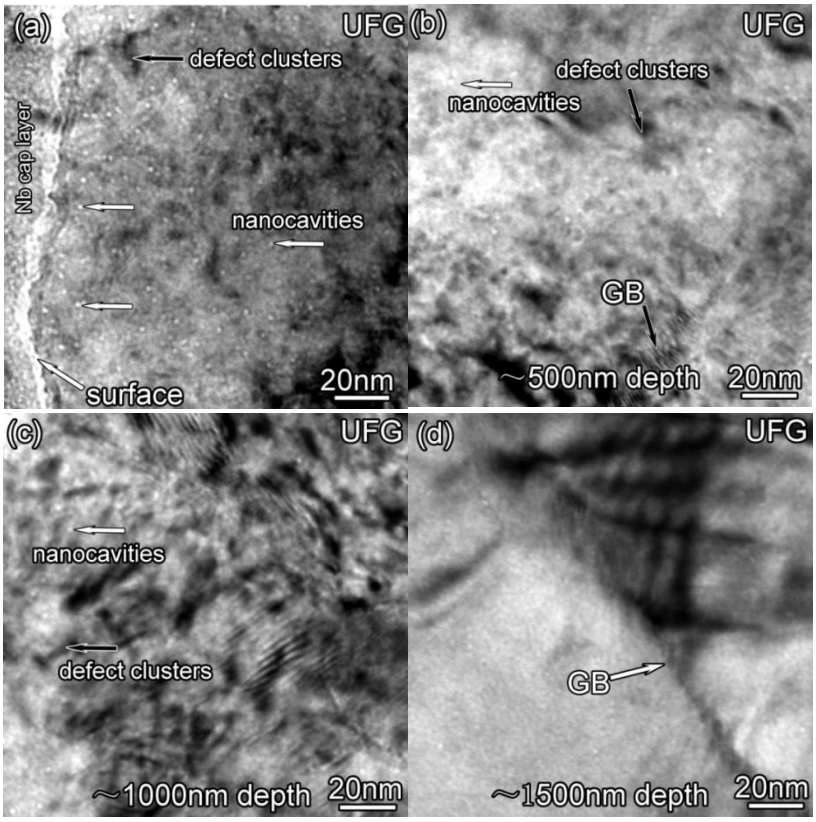

Figure 7.4 XTEM micrographs (captured at an under focus distance of -500 nm) display the depth dependent distribution of radiation induced nanocavites in UFG T91 steel.(a) Numerous nanocavites are observed close to the surface.(b) At ~500 nm below the surface, only sporadic nanocavities are detected.(c) The peak damage zone, ~1000 nm from surface, contains nanocavites and scattered dislocation loops.(d) At the end of the projected range, ~1500 nm, the density of the nanocavites and dislocation loops decreases sharply.

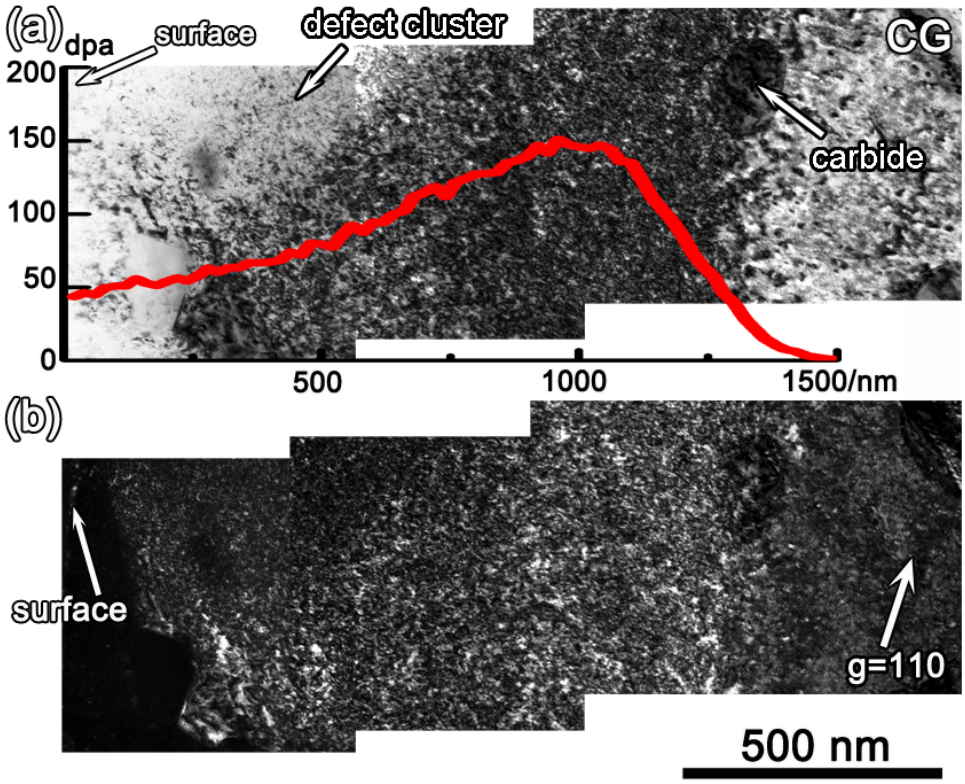

Figure 7.5 Cross-sectional overview of defect clusters of CG T91 steel irradiated up to a maximum of 150 dpa at 450 °C under (a) a dynamic two beam condition (g = 110), and (b) a corresponding weak beam dark field (WBDF) imaging condition. An SRIM simulation of depth dependent dpa plot is superimposed on the image (a). Close to the peak damage region, a high density of black dots (part of dislocation loops) are observed in (a), and the contrast reverses to be white spots in the WBDF diffraction condition in (b).

In addition to nanocavities, dislocation loops are also present in irradiated CG and UFG specimens as shown in bright and dark field TEM micrographs (Fig. 7.5 and 7.6) captured under dynamic two beam (TB) or weak beam dark field (WBDF) conditions using a g vector of <110>. In CG T91, the irradiated zone is filled with a high density of black defect clusters. The maximum defect density (Fig. 7.5a) occurs at ~ 1000 nm underneath surface, consistent with the superimposed SRIM simulated depth dependent DPA profile. Black dots in large carbide particles are also visible. The weak beam dark field (WBDF) TEM micrograph (Fig.7.5b) reveals a similar trend of variation

of defect density with inverse contrast, where defect clusters exhibit bright contrast. In parallel, a similar depth dependent evolution of dislocation loops is observed in the panoramic view of irradiated UFG T91 (Fig. 7.6a) and corresponding snap shots recorded at various depth in the two beam (BF) TEM micrographs obtained at two-beam conditions (Fig. 7.6b-e) and in corresponding TEM micrographs WBDF (Fig. 7.6b'-e'). A g vector of <110> is maintained to avoid orientation influence on the density and size of the defect clusters. Dislocation entanglement is noticed at the end of the damage zone (Fig.7.6e'). In both CG and UFG T91 materials, the density of defect clusters decreases significantly at depths greater than about 1250 nm.

Quantitative estimations of depth dependent defect density and size were performed, given that the average TEM foil thickness across the irradiation zone were measured to be 98 and 96 nm for CG and UFG T91 by using Kossel-Möllesnstedt fringes. A comparison of the density of nanocavities is shown in Fig.7.7a. The density of nanocavities in CG T91 was the highest at the surface, followed by a rapid decrease within 250 nm from the surface, reaching a plateau over a range of 400-1000 nm, and then continuing to drop to a non-detectable level at a depth of 1500 nm. The density of nanocavities in irradiated UFG T91 followed similar depth dependence, but was at least 50% lower than that of CG T91 at an identical depth. The density of dislocation loops in CG T91 (Fig.7.7b) increased monotonically with depth and reaches a maximum at 1200 nm from the surface. In comparison, the dislocation loop density in UFG T91 reached its peak value at 700 nm underneath surface and is lower than that of CG counterparts. The nature of the loops was identified to be predominately of the interstitial type. There is no

statistically significant difference on nanocavity size (Fig.7.7c) and loop size (Fig.7.7d) between irradiated UFG and CG T91, although the dimensions of both types of defects appear to increase slightly with depth.

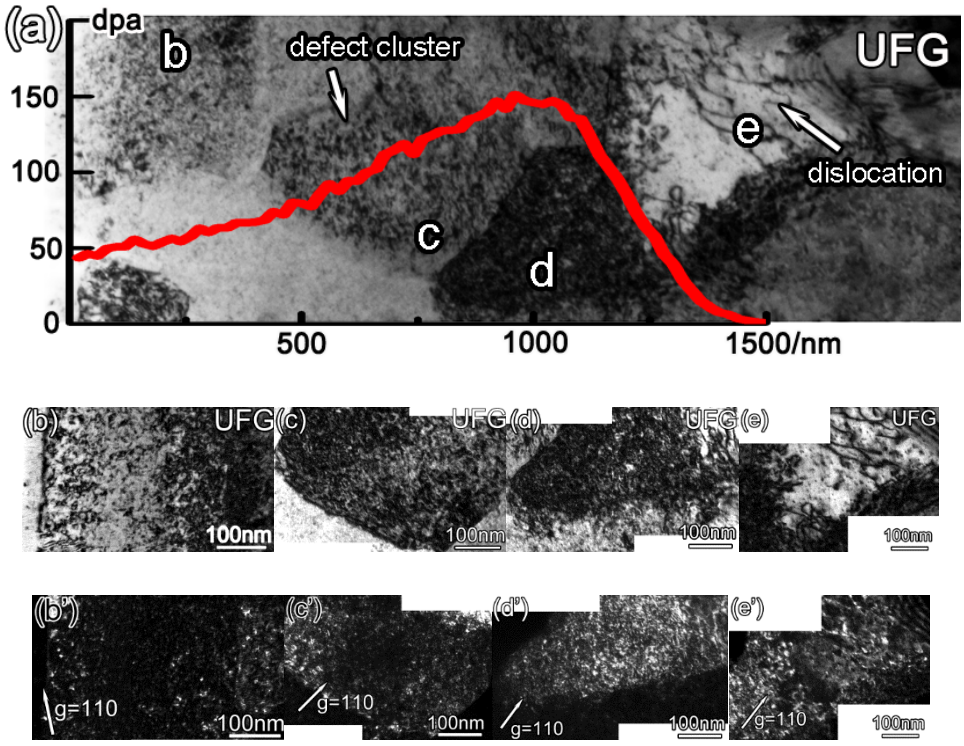

Figure 7.6 (a) Cross-sectional bright field (BF) TEM micrograph of UFG T91 irradiated at the same condition (150 dpa at 450 °C) shows the depth dependent evolution of dislocation loops. (b-e) BF TEM micrographs of various locations (labeled in (a)) examined under a dynamic two beam condition. As there are multiple ultra-fine grains in the projected radiation range, each region was oriented separately to optimize the view of dislocation loops. (b'-e') Corresponding WBDF micrographs display the dislocation loops (bright spots) captured at various depths.

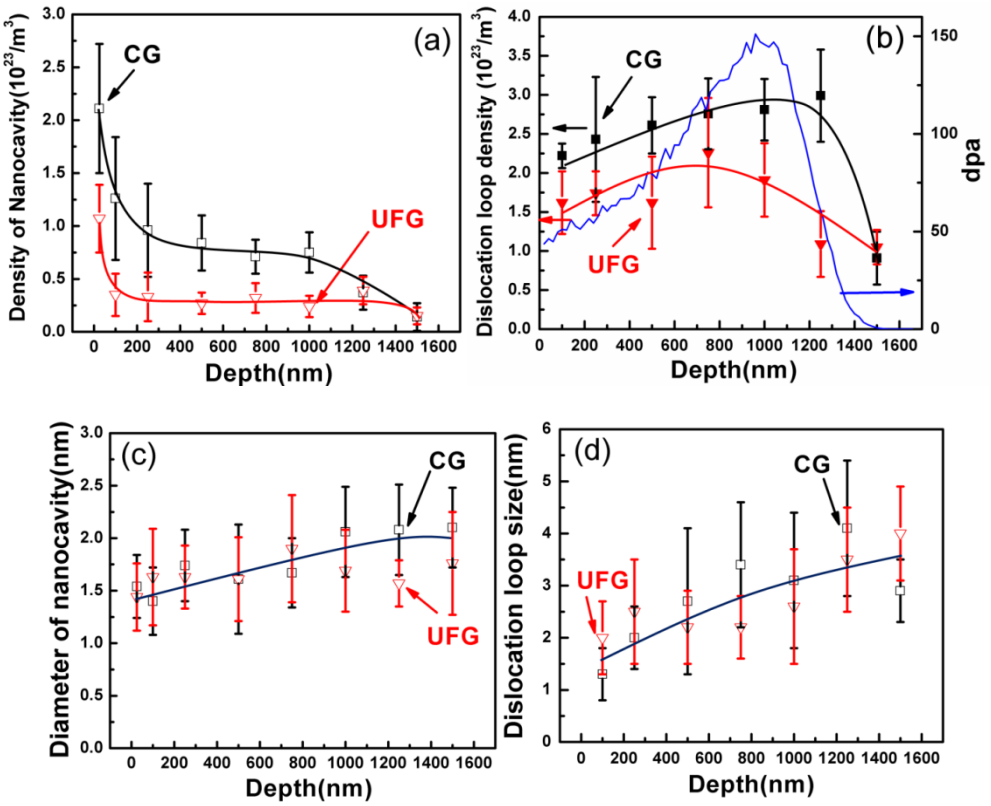

Figure 7.7 Comparison of depth dependent distributions of density and size of nanocavities and dislocation loops in irradiated CG and UFG T91 steel.(a) The density of nanocavities is the greatest at the surface and decreases rapidly with depth. UFG T91 has a noticeable lower cavity density across the entire irradiated range. (b) The density of dislocation loops increases gradually with depth and reaches a maximum at the peak damage location (as indicated by superimposed SRIM simulation of dpa). The maximum loop density occurs at 750 nm for UFG T91, compared to 1250 nm observed in CG T91. (c) In both CG and UFG T91 steels, the average diameter of nanocavities increases slowly with depth from 1.5 to 2 nm. (d) The average dimension of dislocation loops, similar for both UFG and CG T91, is estimated to increase from 1.5 to 3.5 nm with depth. There is no statistically significant difference between the dimension of nanocavities and dislocation loops in the CG and UFG T91 steels.

Depth dependent swelling profiles shown in Fig. 7.8a, calculated from nanocavity size and density measurements, show the magnitude of swelling in CG (UFG) decreased to a minimum at 700 nm (300nm) from the surface, and then reached a peak value at 1000 nm (700 nm) thereafter. Evidently, irradiated CG T91 exhibits more swelling than UFG T91 at the same depth, across the irradiated region. According to the relationship between dpa and depth, we are able to correlate dpa and swelling data. The

dpa values are estimated using interpolation by the nearest two values from the SRIM calculated depth and dpa curve. Swelling rates UFG T91, determined by linear fitting of swelling vs dpa values (Fig. 7.8b) is about one-third that of irradiated CG T91, at a value around 1×10^{-4}%/ dpa.

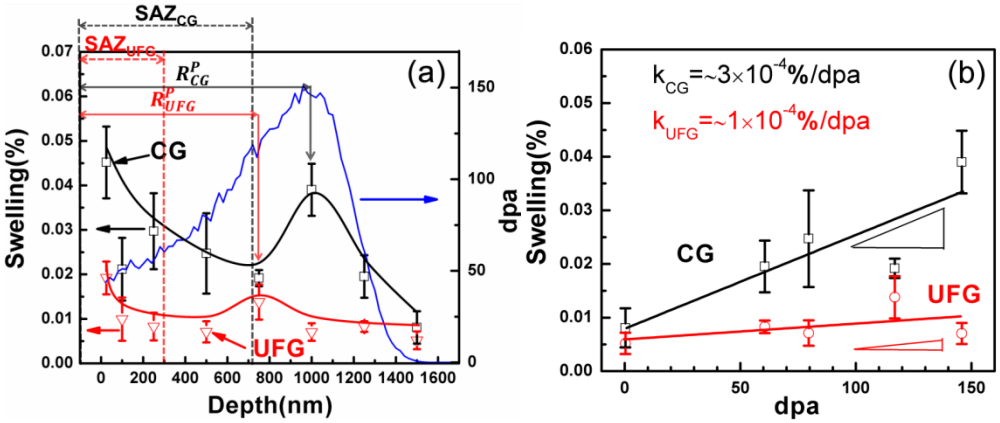

Figure 7.8 (a) Comparison of depth dependent evolution of swelling of CG and UFG T91 steel. The SRIM simulated dpa plot is shown as a reference. Both specimens have maximum swelling close to surface. The surface affected zone (SAZ) of UFG is ~ 300 nm shallower than that of the CG material ~700 nm. Above these values, the surface effect approximately ceases to operate. Swelling increases thereafter and reaches a peak at 1000 nm R^P_{CG} for CG T91 and at 750 nm R^P_{UFG} for UFG T91. (b) Excluding surface effects, the swelling increases more rapidly in CG T91 than that in UFG T91. The swelling rate of CG T91 is calculated to be ~0.03%/100 dpa, compared to ~ 0.01%/100 dpa in UFG T91.

7.2 Prominent size effects on enhanced radiation tolerance

Compared with their CG counterparts, UFG T91 steel contains a lower density of nanocavities and dislocation loops (Fig.7.7) and shows reduced swelling and swelling rate (Fig. 7.8), implying the significance of defect sinks on defect mitigation. Although dislocations can also alleviate radiation damage, they are typically considered as biased defect sinks that absorb interstitials preferentially. GBs, on the other hand are a type of neutral defect sink, and may dominate the enhanced radiation tolerance observed in UFG

T91 steel. Thus, we estimate the GB sink strength while considering the internal defect sinks (within grains) are mostly dislocations.

The dislocation sink strength k_{disl}^2 ,in units of cm^{-2} is given by [89]:

$$k_{disl}^2 = z_d \rho_d \qquad \text{Eq.7.1}$$

where z_d is the number of capture sites per dislocation line intercepted with a crystal plane. ρ_d is the dislocation density. As the dislocation core size is typically 1-3b (where b is the magnitude of Burgers vector), the value of z_d is ~2-10.

The sink strength for grain boundaries, k_{gb}^2, in units of cm^{-2}, is given by [106, 112]:

$$k_{gb}^2 = 6k / d \text{ when } kd \to \infty \qquad \text{Eq.7.2}$$

and

$$k_{gb}^2 = 60 / d^2 \text{ when } kd \to 0 \qquad \text{Eq.7.3}$$

where d is the diameter of grains, and k^2 is the sink strength of internal defect sinks within the grains.

The dislocation density of annealed metals is typically on the order of 10^7~$10^{10}/cm^2$ [215, 216], which fits well for the mechanical properties of annealed T91 steel [217]. Assuming the internal defect sinks are primarily dislocations, k_{disl}^2 will be of a similar order of magnitude with a dislocation density, ~$10^{10}/cm^2$ (taking an upper bound value). Considering the grain size of UFG (320 nm) and CG (2000 nm) T91, the value of $k_{disl}d$ is 3.2-20. Thus k_{gb}^2 , estimated by using Eq.7.3, is $5.8\times10^{10}/cm^2$ for UFG

T91 and 1.5×10^9/cm^2 for the CG T91. It is evident that k_{gb}^2 of UFG T91 is ~40 times greater than that of the CG T91, in qualitative agreement with experimental observations.

Although the foregoing theory developed by Bullough *et al.*[112] can qualitatively predict grain size effect on the sink strength, it cannot be applied without limitation, especially for quantitative calculations. These equations are derived from the continuity equation, where grains are assumed to be spherical, which cannot fill all of space. Bulk recombination is assumed to be a minor effect, which may not be true in reality. Material properties and the grain boundary character are not accounted for in deriving in these equations. Defects properties are also not considered. Although other attempts have been tried [218], a detailed quantitative relation for sink strength that includes grain boundary character is still open to question.

7.3 Depth dependent swelling in irradiated T91 steel

The much greater magnitude of cavity density and swelling close to the surface in both specimens may be due to the existence of strong surface sinks. Free surfaces are known to be highly effective sinks for point defects [98, 219, 220]. Mobile defects, such as interstitials and their clusters, can exit a free surface rapidly during radiation, leaving less mobile defects, such as vacancies behind, and consequently vacancy clusters grow into nanocavities.

Next we use thin foil surface sink strength to crudely estimate the surface sink strength in an attempt to qualitatively understand free surface effects on defect formation

in heavy ion irradiated T91 steel. The sink strength of a thin foil surface is generally written as [112]:

$$k_s^2 = k_a / l \text{ when } k_a l \to \infty \qquad \text{Eq.7.4}$$

and

$$k_s^2 = 3 / l^2 \text{ when } k_a l \to 0 \qquad \text{Eq.7.5}$$

where k_s^2 is the sink strength of the free surface, l is the half foil thickness, and k_a^2 is the sink strength of all other microstructural defect sinks within the foil, or the internal sink strength (mainly dislocations and GBs).

Evidently as l increases the sink strength of the free surface quickly decreases and hence the density of nanocavities close to the free surface declines, consistent with experimental observations in the CG specimens (Fig.7.8a). The lower values of surface swelling in UFG T91 can be interpreted from the following perspectives. First, high angle GBs in close proximity to a free surfaces are competing defect sinks that absorb vacancies and interstitials, and thus reduce the clustering of vacancies. Second, as mentioned earlier, enhanced swelling close to a free surface is directly related to disparate mobility of vacancies and interstitials. The existence of abundant high angle GBs may restrain the rapid migration of interstitials (away from vacancies). Such GB induced geometric confinement (as shown in Fig.7.9a') may promote recombination of vacancy-interstitial complexes and alleviate surface swelling.

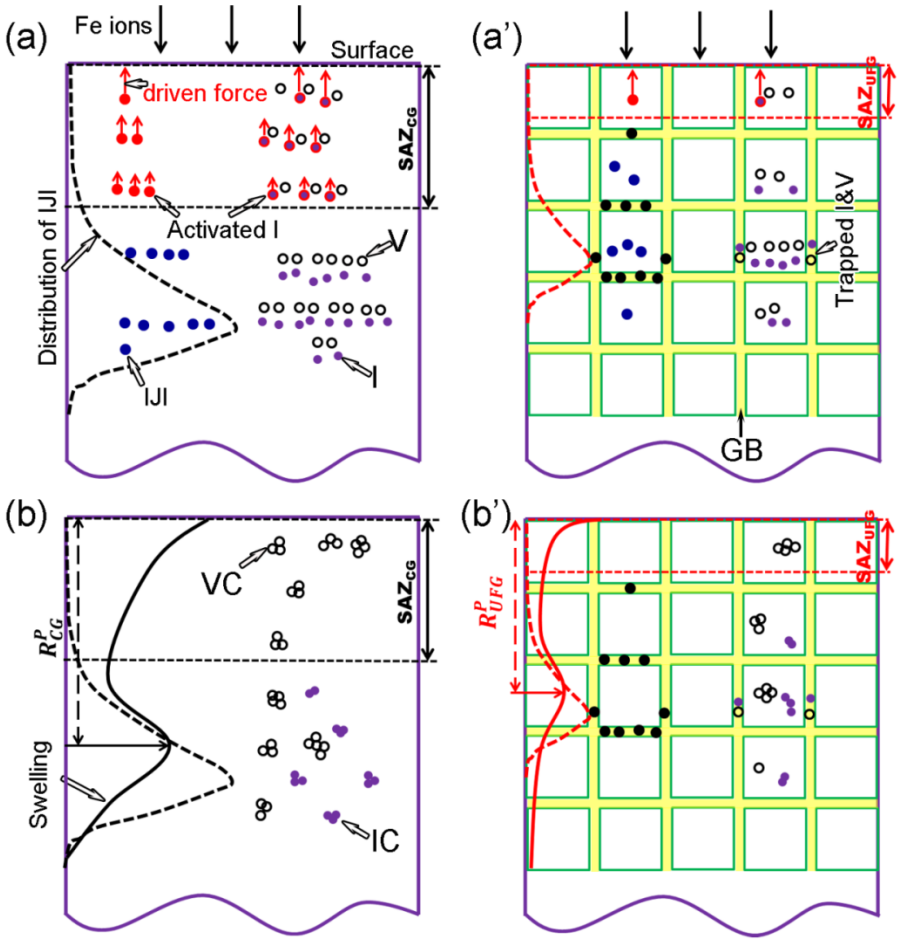

Figure 7.9 Schematic of GB effects on the distribution of injected interstitials and consequence of injected interstitial and multiple sinks on the evolution of defect clusters in CG (a-b) and UFG (a'-b') T91 steels. (i) For defect evolution in CG material (a-b), (a) interstitials within the SAZ are considered as activated interstitials which tend to be absorbed by the free surface if not annihilated. (b) Due to the effect of injected interstitials, vacancies get more chance to recombine with interstitials. Thus, the nucleation of voids is suppressed by injected interstitials. The material ends up with a high density of vacancy clusters near the surface due to surface sinks. Peak swelling also occurs at a certain depth. (ii) In comparison in UFG materials, (a') GBs can serve as a barrier to block injected interstitials. The injected interstitial may be forced to rest at a shallower depth. At the same time, due to GB sinks, normal vacancies and interstitials can be absorbed, resulting in a lower defect density in UFG material. (b') The peak swelling could occur at a shallower depth due to the shift and weakened injected interstitial effect. The peak damage depth is shallower in UFG material compared to CG material. Note: I: interstitial; V: vacancy; IJI: injected interstitial; VC: vacancy clusters or nanocavities; IC: interstitial cluster; R^P: range to peak damage; SAZ: surface affected zone.

We also notice that the maximum swelling in the UFG material occurs at a shallower depth than that of CG T91 material (Fig. 7.8a), a phenomenon that could be

related to the "injected interstitial" concept. Here, injected ions come to rest within the crystal lattice and become an interstitial without a vacancy partner. These deposited interstitials can suppress the nucleation rate of voids by orders of magnitude. This so-called "injected interstitial effect" can be enhanced whenever defect recombination is predominant or vacancies have low mobility [221, 222]. This concept was first proposed by *Mansur at al.* to explain the atypical-neutron process of ion irradiation [103, 114]. Similar phenomena were observed in Ni ion irradiated 304 stainless steel, Fe-Cr-Ni alloys and pure Ni [104, 223]. *Garner* proposed that the combination of surface and injected interstitial effects can explain atypical- neuron processes in ion irradiated material[104]. Due to the injected interstitial effect, a depth dependent swelling curve, which is supposed to follow the predicted dpa values, can be changed significantly. Any factor that perturb the distribution of injected interstitials will affect the depth dependent void swelling.

In the vicinity of the free surface, the effect of injected interstitials is weak, thus the surface effect plays a dominant role on swelling. As ions penetrate deeper, the injected interstitial effect takes over, and consequently the nucleation of voids is significantly suppressed. In the peak damage region, as interstitials migrate faster than vacancies, the nucleation of vacancy clusters cannot be fully suppressed, and the density of nanocavites goes up. The above explanation describes the depth dependent swelling in CG T91 reasonably well. In UFG T91, GBs serve as barriers to limit the rapid migration of interstitials, and thus peak swelling occurs at a shallower depth compared to CG materials (Fig.7.9b').

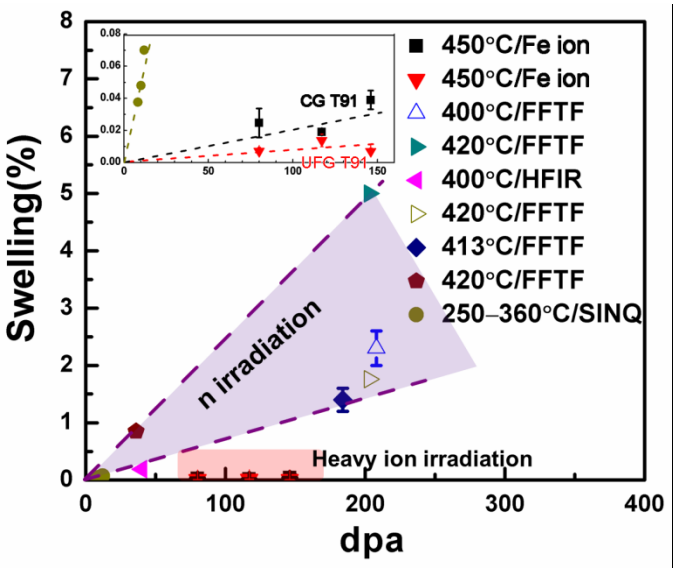

Figure 7.10 Comparison of several T91 steel heats irradiated by neutron and heavy ions between 400 ~ 450 °C at different dose levels in different radiation facilities [21, 27, 225-227]. Swelling is measured, in two ways, from quantitative microscopy data (represented by solid symbols), and from macroscopic immersion density measurements (shown as open symbols). The helium generation rate is about 0.3 ~ 0.5 appm He/dpa in the Fast Flux Test Facility (FFTF) [228], 0.8 appm He/dpa in the High Flux Isotope Reactor (HFIR) [229], and 100 appm He/dpa at 360 °C in the Swiss Spallation Neutron Source (SINQ)[230]. The average swelling rate of neutron irradiated T91 is on the order of ~ 1%/100 dpa (0.5~2.5%/100 dpa). For instance, the swelling rate is around 0.7%/100 dpa in SINQ. In comparison, heavy ion irradiated CG T91 has a swelling rate of 0.03%/100 dpa, and UFG T91 has a three times lower swelling rate, 0.01%/100 dpa. The inserted plot shows a magnified view of results of swelling in heavy ion irradiated CG and UFG and neutron irradiated T91 via SINQ at 360°C.

7.4. Comparison of swelling with other irradiated T91 steels

Voids as large as 10 nm in diameter were observed in heavy ion irradiated CG T91 up to a fluence of 6.7×10^{20} ions/m^2 with a rastering beam [224]. No swelling was expected due to a low void density. Except for a slightly different tempering history, previous studies have used an irradiation condition similar to this study. The effect of beam rastering may be inferred as promoting the formation of large voids. More experimental evidence with better controlled specimens is needed to prove this point.

Our study also shows a very low swelling rate, two orders of magnitude lower, compared to published neutron irradiated data (Fig.7.10). Although a different

calculation mode by SRIM simulation can result in dissimilar dpa values for a given dose, this difference is commonly within a factor of two. This cannot account for the large disparity with the current work. Especially, because the calculation method we used is relatively conservative. Heavy ion irradiations are neutron-atypical processes, as manifested by the lack of transmutation products, such as helium and hydrogen, intrinsic differences in dose rate, and surface influences. Helium gas is insoluble in steel and can influence the onset of swelling significantly in several ways [115]. It can pressurize cavities, change existing sink strength, and alter atomic transport. Cavity pressurization, the most straightforward way to affect swelling, can decrease the critical radius of cavities for bias driven growth. The transient region can be significantly reduced by this process. Swelling is then inevitable during the subsequent radiation. Dose rate is another factor that can influence swelling rate, which shall be put into special consideration when using heavy ion irradiation to simulate neutron damage [105]. However, this problem is solved to some extent by an internal temperature shift method. If the swelling rate is kept invariant, different dose rates can be converted by a temperature shift, described as [106],

$$T_2 - T_1 = \frac{[kT_1^2 / (E_v^m + 2E_v^f)]\ln(G_2 / G_1)}{1 - [kT_1 / (E_v^m + 2E_v^f)]\ln(G_2 / G_1)} \qquad \text{Equ.7.6}$$

where k is Boltzmann's constant, T is temperature, E_v^f and E_v^m denote the vacancy formation energy and migration energy, and G is the dose rate.

We use Fe to estimate the temperature shift induced by different dose rates. E_v^f and E_v^m are ~ 2 eV and 0.55 eV for Fe [231]. The dose G_1 at the surface and peak

damage zone is 3.3×10^{-3} and 1×10^{-2} dpa/s for the present heavy ion irradiation study, and G_2 is 1×10^{-6} dpa/s for Fast Flux Test Facility (FFTF) neutron radiation experiments. The temperature shift is in the range of -70 ~ -80°C from surface to peak damage zone, and is nearly constant through such irradiated zone. The accelerated dose rate during heavy ion irradiation at 450 °C in this study is thus comparable to neutron studies at around ~370 °C. *Jia at al.* reported a batch of T91 steel irradiated in the Swiss spallation neutron source (SINQ) over the range 110 ~ 360 °C with a maximum dose of about 11.8 dpa [230]. The bubble size and density following irradiation at 360 °C was similar to that of nanocavities in the present study (shown in Fig.9). Vitek *et al.* reported that a few small cavities around 4 ~ 6 nm were homogenously distributed within the matrix after neutron irradiation at 300 °C in the High Flux Isotope Reactor (HFIR) [226], which is still larger than those of our observation. Hence, the effect of dose rate alone cannot explain atypical-neutron processes in heavy ion irradiated specimens. The effect of helium discussed previously must therefore be considered.

The existence of tiny nanocavities in high dose heavy ion irradiated T91 is unexpected but rational, because these nanocavities might imply the nucleation process of voids. Similar observations (formation of very tiny voids without the present of inert gases) have been rarely reported. Kirk *et al.* observed small voids (1 ~ 2 nm) during an in situ Kr ion irradiation to 200 dpa at 500 °C of MA957 ODS steel (a commercialized oxide dispersion strengthened ferritic steel) [232].

7.5 Summary

In this chapter, several grain size effects were noticed after heavy ion irradiation experiments. The UFG T91 shows a lower defect density compared to CG T91. The swelling rate of UFG steel is three times lower than CG T91 steel. The peak damage (void swelling) range of UFG T91 is shallower than CG T91. A strong surface effect accompanied by size effect was noticed. A GB modified injected interstitial concept was proposed. A large deviation in void swelling data between heavy ion and neutron irradiated T91 is noticed, and explained by the disparity of helium and dose rate induced temperature shift, which suggests that proper care should be applied when using the heavy ion radiation technique to simulate neutron radiation damage.

CHAPTER VIII

CONCLUSIONS AND FUTURE WORK

In this chapter, the conclusions of the thesis are drawn from each study. Future work is suggested in light of current studies.

8.1 Conclusions

(1) The dynamic products of γ→α phase transition are investigated in this thesis. The transferred martensite is always accompanied by an auto-tempered behavior which yields ductile martensite. Bainitic ferrite can be formed during the transformation. ε-Carbides were, for the first time, observed in T91 steel. The orientation relationship of ε-Carbides is the same as the classic Jack's relationship $\alpha[1\bar{1}1]//\varepsilon\text{-C}\ [1\bar{2}10]$, $\alpha(011)//\varepsilon\text{-C}\ (000\bar{2})$. The combination of multi scale characterization techniques is better than anyone alone to understand the microstructure of F/M steels.

(2) The ECAE enabled TMT process of T91 is systematically studied in this thesis. A road map for strengthening T91 steel was developed. Thus, T91 steel can be processed to gain multi strength levels, which the single material can satisfy for high or low strength applications. The hardness of ECAEed billets can be characterized by indentation of any plane, if there is no plastic shear localization.

(3) ECAE processing can be divided into cold-ECAE and hot-ECAE related to the recrystallization temperature. Cold-ECAE is more effective in grain refinement of heavy-tempered T91 steel, while hot-ECAE can refine carbide particles to a much

smaller length scale than cold-ECAE or the combination of cold-ECAE. Thus hot-ECAE is recommended for achieving a high density of carbide nanoprecipitates. The refinement mechanism of precipitates via hot-ECAE is tied to the elimination of prior austenite GBs, a preferred nucleation site for coarse carbides. Furthermore, nanoscale carbides obtained by hot-ECAE are more stable against coarsening at elevated temperatures compared to those prepared by cold-ECAE.

(4) The enhanced mechanical strength in ECAEed heavily tempered T91 steel arises primarily from grain refinement and precipitation hardening. The martensite phase can increase the strength of T91 significantly. The tempered martensite is formed by joining thinner laths. 500°C is a maximum temperature for ECAE or water quenched T91,above which either recrystallization of ferrite or decompositon of martensite will occur.

(5) 12 Cr ODS steel was processed by ECAE at 300 and 700 °C. The 03H ODS shear localized during extrusion. The as-HIPped material had a coarse grain and fine grain bimodal distribution. The coarse grains, up to several microns in diameter in as-HIPped ODS steels, were successfully refined to ～500 nm in the 04H ODS steel. In addition, Cr rich particles including $M_{23}C_6$, Cr oxide were effectively refined as well and their volume fraction reduced. The Y_2O_3 particle distribution was improved after ECAE, and the particle geometry was also changed and some even fractured. No significant hardening was observed in the 03H ODS steel. Hardening up to 35 % after ECAE in 04H ODS steel was observed and is attributed to grain refinement with a minor contribution from precipitates. The 03H ODS steel exhibited better thermal stability due to the high oxygen content.

(6)Comparison the CG and UFG steels after heavy ion irradiation, lead to the finding that the UFG T91 exhibits better radiation tolerance compared to its CG counterpart. High density nanocavities with sizes 1 ~ 2 nm were observed in both CG and UFG T91 steels. UFG T91 shows a lower defect density compared to CG T91. The swelling rate of UFG steel is three times lower than CG T91 steel. The peak damage (void swelling) range of UFG T91 is shallower than CG T91. A strong surface effect accompanied by size effect was noticed. These observations are explained through competition of point defects between GBs and free surfaces, and a GB modified injected interstitial concept. A large deviation in void swelling data between heavy ion and neutron irradiated T91 is noticed, and explained by the disparity of helium and dose rate induced temperature shift. Proper care should be applied when using the heavy ion radiation technique to simulate neutron radiation damage.

Overall, these studies suggest that ECAE has great potential to tailor the microstructure of reactor steels such as T91 or ODS steels for their structural application in advanced nuclear reactors or other system. The strength and radiation performance can be enhanced by deformation. But ductility is usually sacrificed, which it can be regained through heat treatment. Thermal stability is a major concern for these deformation strengthening steels. The more beneficent is gainedin a material from deformation, the more vulnerable to recrystallization it becomes. The maximum temperature must be determined before any real application.

8.2 Future work

Although intensive work had been done here or by other researchers, some problems related to T91 or ODS steel are still open to question. The basic TTT curves including all dynamic phase boundaries(bainitic ferrite) should be generated. The basic idea behind the TTT curves is to determine how different cooling rates can influence the phase transition of T91 steel. It is very interesting that some batches of T91 steel are very brittle after water quenching (unpublished data). The T91 here is very ductile. The effect of alloying element control should be addressed, especially the carbon contents, which can play a big role in the T91 microstrucutre.

A combination of cold and hot ECAE should be used to refine both grain size and the carbides. The detailed refining mechanism related to how the tempered martensite evolved into the elongated lamellar structure is not clear. Hot ECAE can destroy PAGBs, however, a process is desirable that can destroy the PAGBs while maintaining the tempered martensitic lath structure. PAGBs are proved to be important for irradiation induced segregation, while the refined structure is poor in thermal stability. Modification of T91 steel by addition of other elements is another possibility for increasing the thermal stability of UFG T91 steel. Long term thermal stability and good high temperature tensile properties of the TMT processed T91 are still lacking. Without such an evaluation, TMT processed T91 steel is unlikely to be applied with confidence.

ODS steel is clearly much more complicated than T91. The blending of elemental powders clearly needs to be improved. The structure of some oxide particles is

not clear. The effect of oxygen in the ODS steels is an important factor worth detailed evaluation. Direct consolidation of ODS powder by ECAE could be done for comparison to the process used in this thesis. Other problems related to ODS are welding and DBTT. These are both practical limits for ODS steels. ODS steels also provide a chance for direct test of the Orowan' mechanism. In situ nano indentation or tensile test can provide a unique understanding of the role of oxide particles in mechanical performance.

Radiation is another issue that demands future work. The TMT processed T91 has been seldom evaluated after irradiation. No attempt was tried to understand irradiation induced precipitates and segregation effects in TMT processed T91 steel. The nanocavities observed here are likely to stay within the transient region of swelling. Concurrent irradiation with helium and heavy ions is worth initiated to give more confidence to the TMT processed T91 steel. Then, selected samples from heavy ion irradiation experiments can be further irradiation by neutrons from operating reactors. That would be the ultimate evaluation for TMT processed T91 steel.

REFERENCES

[1] R. Klueh, International Materials Reviews, 50 (2005) 287-310.

[2] R.L. Klueh, J.P. Shingledecker, R.W. Swindeman, D.T. Hoelzer, J. Nucl. Mater., 341 (2005) 103-114.

[3] S.J. Zinkle, J.T. Busby, Mater.Today, 12 (2009) 12-19.

[4] H. Bhadeshia, R. Honeycombe, Steels: Microstructure and Properties: Microstructure and Properties, Butterworth-Heinemann, Linacre House, Jordan Hill, Oxford OX2 8DP, UK, 2011.

[5] R. Swindeman, M. Santella, P. Maziasz, B. Roberts, K. Coleman, International Journal of Pressure Vessels and Piping, 81 (2004) 507-512.

[6] R. Klueh, K. Ehrlich, F. Abe, J. Nucl. Mater., 191 (1992) 116-124.

[7] R. Klueh, A. Nelson, J. Nucl. Mater., 371 (2007) 37-52.

[8] M.J. Cohn, J.F. Henry, D. Nass, Journal of Pressure Vessel Technology, 127 (2005) 197-203.

[9] R.L. Klueh, Reduced activation materials for fusion reactors, ASTM International,1916 Race Street, Philadelphia, PA 19103, 1990.

[10] A. Kohyama, A. Hishinuma, D. Gelles, R. Klueh, W. Dietz, K. Ehrlich, J. Nucl. Mater., 233 (1996) 138-147.

[11] V. de Castro, E.A. Marquis, S. Lozano-Perez, R. Pareja, M.L. Jenkins, Acta Mater., 59 (2011) 3927-3936.

[12] H.R.Z. Sandim, R.A. Renzetti, A.F. Padilha, D. Raabe, M. Klimenkov, R. Lindau, A. Möslang, Mater. Sci. Eng. A, 527 (2010) 3602-3608.

[13] B. van der Schaaf, F. Tavassoli, C. Fazio, E. Rigal, E. Diegele, R. Lindau, G. LeMarois, Fusion Eng. Des., 69 (2003) 197-203.

[14] R. Lindau, A. Möslang, M. Rieth, M. Klimiankou, E. Materna-Morris, A. Alamo, A.A.F. Tavassoli, C. Cayron, A.M. Lancha, P. Fernandez, N. Baluc, R. Schäublin, E. Diegele, G. Filacchioni, J.W. Rensman, B.v.d. Schaaf, E. Lucon, W. Dietz, Fusion Eng. Des., 75-79 (2005) 989-996.

[15] R. Klueh, D. Gelles, S. Jitsukawa, A. Kimura, G. Odette, B. Van der Schaaf, M. Victoria, J. Nucl. Mater., 307 (2002) 455-465.

[16] N. Baluc, D.S. Gelles, S. Jitsukawa, A. Kimura, R.L. Klueh, G.R. Odette, B. van der Schaaf, J. Yu, J. Nucl. Mater., 367-370 (2007) 33-41.

[17] R. Lindau, A. Möslang, M. Rieth, M. Klimiankou, E. Materna-Morris, A. Alamo, A.-A. Tavassoli, C. Cayron, A.-M. Lancha, P. Fernandez, Fusion Eng. Des., 75 (2005) 989-996.

[18] W. Bendick, L. Cipolla, J. Gabrel, J. Hald, International Journal of Pressure Vessels and Piping, 87 (2010) 304-309.

[19] M.J. Cohn, J.F. Henry, D. Nass, Journal of Pressure Vessel Technology, 127 (2005) 197.

[20] H. Fan-Hsiung, M.L. Hamilton, J. Nucl. Mater., 187 (1992) 278-293.

[21] M. Toloczko, F. Garner, C. Eiholzer, J. Nucl. Mater., 212 (1994) 604-607.

[22] Y. Chen, K. Sridharan, T. Allen, Corrosion Science, 48 (2006) 2843-2854.

[23] D. Sapundjiev, S. Van Dyck, W. Bogaerts, Corrosion Science, 48 (2006) 577-594.

[24] Y. Dai, P. Marmy, J. Nucl. Mater., 343 (2005) 247-252.

[25] G. Gupta, Z. Jiao, A. Ham, J. Busby, G. Was, J. Nucl. Mater., 351 (2006) 162-173.

[26] Z. Tong, Y. Dai, J. Nucl. Mater., 398 (2010) 43-48.

[27] J. Van den Bosch, O. Anderoglu, R. Dickerson, M. Hartl, P. Dickerson, J. Aguiar, P. Hosemann, M. Toloczko, S. Maloy, J. Nucl. Mater., 440 (2013) 91-97.

[28] R. Kishore, R. Singh, T. Sinha, B. Kashyap, J. Nucl. Mater., 195 (1992) 198-204.

[29] K. Chandravathi, K. Laha, K. Bhanu Sankara Rao, S. Mannan, Materials science and technology, 17 (2001) 559-565.

[30] S. Kobayashi, K. Sawada, T. Hara, H. Kushima, K. Kimura, Mater. Sci. Eng. A, 592 (2014) 241-248.

[31] C. Liu, D. Zhang, Y. Liu, Q. Wang, Z. Yan, Nuclear Engineering and Design, 241 (2011) 2411-2415.

[32] W.B. Jones, C. Hills, D. Polonis, Metallurgical Transactions A, 22 (1991) 1049-1058.

[33] K. Kaneko, S. Matsumura, A. Sadakata, K. Fujita, W.-J. Moon, S. Ozaki, N. Nishimura, Y. Tomokiyo, Mater. Sci. Eng. A, 374 (2004) 82-89.

[34] K. Sawada, K. Suzuki, H. Kushima, M. Tabuchi, K. Kimura, Mater. Sci. Eng. A, 480 (2008) 558-563.

[35] S. Ukai, M. Harada, H. Okada, M. Inoue, S. Nomura, S. Shikakura, K. Asabe, T. Nishida, M. Fujiwara, J. Nucl. Mater., 204 (1993) 65-73.

[36] R. Lindau, A. Möslang, M. Schirra, P. Schlossmacher, M. Klimenkov, J. Nucl. Mater., 307 (2002) 769-772.

[37] N. Baluc, K. Abe, J.L. Boutard, V.M. Chernov, E. Diegele, S. Jitsukawa, A. Kimura, R.L. Klueh, A. Kohyama, R.J. Kurtz, R. Lässer, H. Matsui, A. Möslang, T. Muroga, G.R. Odette, M.Q. Tran, B. van der Schaaf, Y. Wu, J. Yu, S.J. Zinkle, Nucl. Fusion, 47 (2007) S696-S717.

[38] V. de Castro, T. Leguey, M.A. Monge, A. Muñoz, R. Pareja, D.R. Amador, J.M. Torralba, M. Victoria, J. Nucl. Mater., 322 (2003) 228-234.

[39] D. Hoelzer, B. Pint, I. Wright, J. Nucl. Mater., 283 (2000) 1306-1310.

[40] G.R. Odette, M.J. Alinger, B.D. Wirth, Annu. Rev. Mater. Res., 38 (2008) 471-503.

[41] D. Nobili, F. Mezzetti, E.S. De Maria, J. Mater. Sci., 3 (1968) 282-287.

[42] L. De Wilde, H. Massaux, J. Noels, Powder Technology, 4 (1971) 173-179.

[43] J.J. Fischer, Google Patents, 1978.

[44] M. Inoue, T. Kaito, S. Ohtsuka, Research and development of oxide dispersion strengthened ferritic steels for sodium cooled fast breeder reactor fuels, Materials Issues for Generation IV Systems, Springer, 2008, pp. 311-325.

[45] T. Okuda, S. Nomura, S. Shikakura, Solid State Powder Processing, (1989) 195-202.

[46] S. Ukai, M. Harada, H. Okada, M. Inoue, S. Nomura, S. Shikakura, T. Nishida, M. Fujiwara, K. Asabe, J. Nucl. Mater., 204 (1993) 74-80.

[47] H. Okada, S. Ukai, M. Inoue, J. Nucl. Sci. Technol., 33 (1996) 936-943.

[48] S. Ukai, M. Fujiwara, J. Nucl. Mater., 307 (2002) 749-757.

[49] M.K. Miller, E.A. Kenik, K.F. Russell, L. Heatherly, D.T. Hoelzer, P.J. Maziasz, Mater. Sci. Eng. A, 353 (2003) 140-145.

[50] D. Larson, P. Maziasz, I. Kim, K. Miyahara, Scripta Mater., 44 (2001) 359-364.

[51] A. Hirata, T. Fujita, Y. Wen, J. Schneibel, C. Liu, M. Chen, Nat Mater, (2011).

[52] M. Klimiankou, R. Lindau, A. Möslang, J. Cryst. Growth, 249 (2003) 381-387.

[53] E.A. Marquis, Appl. Phys. Lett., 93 (2008) 181904.

[54] M. Klimenkov, R. Lindau, A. Möslang, J. Nucl. Mater., 386-388 (2009) 553-556.

[55] C.A. Williams, E.A. Marquis, A. Cerezo, G.D.W. Smith, J. Nucl. Mater., 400 (2010) 37-45.

[56] R.Z. Valiev, T.G. Langdon, Prog. Mater Sci., 51 (2006) 881-981.

[57] R.Z. Valiev, R. Islamgaliev, I. Alexandrov,Prog. Mater. Sci. 45(2000)103-189.

[58] V. Segal, Mater. Sci. Eng. A, 271 (1999) 322-333.

[59] A. Gholinia, P. Prangnell, M. Markushev, Acta Mater., 48 (2000) 1115-1130.

[60] M. Furukawa, Z. Horita, M. Nemoto, T. Langdon, J. Mater. Sci., 36 (2001) 2835-2843.

[61] Y. Estrin, A. Vinogradov, Acta Mater., 61 (2013) 782-817.

[62] V. Segal, Mater. Sci. Eng. A, 197 (1995) 157-164.

[63] K. Nakashima, Z. Horita, M. Nemoto, T.G. Langdon, Mater. Sci. Eng. A, 281 (2000) 82-87.

[64] S. Ferrasse, K.T. Hartwig, R.E. Goforth, V.M. Segal, Metall. Mater. Trans. A, 28 (1997) 1047-1057.

[65] Y. Iwahashi, Z. Horita, M. Nemoto, T.G. Langdon, Acta Mater., 46 (1998) 3317-3331.

[66] Z. Horita, M. Furukawa, M. Nemoto, T. Langdon, Materials science and technology, 16 (2000) 1239-1245.

[67] R. Valiev, Nat Mater, 3 (2004) 511-516.

[68] Q. Xue, I. Beyerlein, D. Alexander, G. Gray Iii, Acta Mater., 55 (2007) 655-668.

[69] C. Huang, G. Yang, B. Deng, S. Wu, S. Li, Z. Zhang, Philos. Mag., 87 (2007) 4949-4971.

[70] D. Shin, I. Kim, J. Kim, Y. Kim, S. Semiatin, Acta Mater., 51 (2003) 983-996.

[71] I. Karaman, G. Yapici, Y. Chumlyakov, I. Kireeva, Mater. Sci. Eng. A, 410 (2005) 243-247.

[72] M. Mabuchi, K. Ameyama, H. Iwasaki, K. Higashi, Acta Mater., 47 (1999) 2047-2057.

[73] T. Liu, W. Zhang, S. Wu, C. Jiang, S. Li, Y. Xu, Mater. Sci. Eng. A, 360 (2003) 345-349.

[74] D. Foley, M. Al-Maharbi, K. Hartwig, I. Karaman, L. Kecskes, S. Mathaudhu, Scripta Mater., 64 (2011) 193-196.

[75] K.-T. Park, Y.-S. Kim, J.G. Lee, D.H. Shin, Mater. Sci. Eng. A, 293 (2000) 165-172.

[76] Z. Horita, K. Ohashi, T. Fujita, K. Kaneko, T.G. Langdon, Advanced Materials, 17 (2005) 1599-1602.

[77] C. Xu, M. Furukawa, Z. Horita, T.G. Langdon, Acta Mater., 51 (2003) 6139-6149.

[78] M. Eddahbi, M. Monge, T. Leguey, P. Fernández, R. Pareja, Mater. Sci. Eng. A, 528 (2011) 5927-5934.

[79] C. Xu, M. Furukawa, Z. Horita, T.G. Langdon, Acta Mater., 53 (2005) 749-758.

[80] S.R. Kumar, K. Gudimetla, P. Venketachalam, B. Ravisankar, K. Jayasankar, Mater. Sci. Eng. A, (2011).

[81] Y. Li, T.G. Langdon, J. Mater. Sci., 35 (2000) 1201-1204.

[82] O. Saray, G. Purcek, I. Karaman, T. Neindorf, H. Maier, Mater. Sci. Eng. A, 528 (2011) 6573-6583.

[83] R. Valiev, I. Alexandrov, Y. Zhu, T. Lowe, J Mater.Res. 17 (2002) 5-8.

[84] Y.H. Zhao, X.Z. Liao, S. Cheng, E. Ma, Y.T. Zhu, Adv.Mater., 18 (2006) 2280-2283.

[85] K.T. Park, Y.S. Kim, J.G. Lee, D.H. Shin, Mater. Sci. Eng. A, 293 (2000) 165-172.

[86] Y. Wang, M. Chen, F. Zhou, E. Ma, Nature, 419 (2002) 912-915.

[87] M. Hockauf, L. Meyer, B. Zillmann, M. Hietschold, S. Schulze, L. Krüger, Mater. Sci. Eng. A, 503 (2009) 167-171.

[88] S. Cheng, Y. Zhao, Y. Zhu, E. Ma, Acta Mater., 55 (2007) 5822-5832.

[89] G.S. Was, Fundamentals of radiation materials science: metals and alloys, Springer, New York, 2007.

[90] J. Silcox, P. Hirsch, Philos. Mag., 4 (1959) 72-89.

[91] M. Kiritani, Journal of the Physical Society of Japan, 19 (1964) 618-631.

[92] M. Kiritani, S. Yoshida, Journal of the Physical Society of Japan, 18 (1963) 915.

[93] C. Cawthorne, E. Fulton, Nature, 216(1967)575-576.

[94] J. Brimhall, B. Mastel, J. Nucl. Mater., 33 (1969) 186-194.

[95] R. Rau, R. Ladd, J. Moteff, J. Nucl. Mater., 33 (1969) 324-327.

[96] F. Wiffen, J. Stiegler, Transactions of the American Nuclear Society, Karger allschwilerstrasse 10, CH-4009 Basel, Switzerland, 1969, pp. 119.

[97] R. Nelson, D. Mazey, J. Hudson, J. Nucl. Mater., 37 (1970) 1-12.

[98] D. Norris, J. Nucl. Mater., 40 (1971) 66-76.

[99] H. Brager, J. Straalsund, J. Nucl. Mater., 46 (1973) 134-158.

[100] J. Leitnaker, E. Bloom, J. Stiegler, J. Nucl. Mater., 49 (1973) 57-66.

[101] N. Yoshida, M. Kiritani, Journal of the Physical Society of Japan, 35 (1973) 1418-1429.

[102] W. Johnston, J. Rosolowski, A. Turkalo, T. Lauritzen, J. Nucl. Mater., 54 (1974) 24-40.

[103] E. Lee, L. Mansur, M. Yoo, J. Nucl. Mater., 85 (1979) 577-581.

[104] F. Garner, J. Nucl. Mater., 117 (1983) 177-197.

[105] N. Packan, K. Farrell, J. Stiegler, J. Nucl. Mater., 78 (1978) 143-155.

[106] L. Mansur, J. Nucl. Mater., 216 (1994) 97-123.

[107] B. Singh, A. Foreman, Philos. Mag., 29 (1974) 847-858.

[108] E. Little, D. Stow, J. Nucl. Mater., 87 (1979) 25-39.

[109] F. Garner, M. Toloczko, B. Sencer, J. Nucl. Mater., 276 (2000) 123-142.

[110] R. Bullough, B. Eyre, R. Perrin, NUCL APPL TECHNOL, 9 (1970) 346-355.

[111] A. Brailsford, R. Bullough, J. Nucl. Mater., 44 (1972) 121-135.

[112] R. Bullough, M. Hayns, M. Wood, J. Nucl. Mater., 90 (1980) 44-59.

[113] R. Sizmann, J. Nucl. Mater., 69 (1978) 386-412.

[114] A. Brailsford, L. Mansur, J. Nucl. Mater., 71 (1977) 110-116.

[115] L. Mansur, M. Yoo, J. Nucl. Mater., 85 (1979) 523-532.

[116] L. Mansur, E. Lee, J. Nucl. Mater., 179 (1991) 105-110.

[117] K. Russell, Acta Metall., 19 (1971) 753-758.

[118] D. Porter, F. Garner, J. Nucl. Mater., 159 (1988) 114-121.

[119] D. Harries, J. Nucl. Mater., 82 (1979) 2-21.

[120] T. Lechtenberg, J. Nucl. Mater., 133 (1985) 149-155.

[121] S. Brenner, R. Wagner, J. Spitznagel, Metal. Trans.A, 9 (1978) 1761-1764.

[122] G. Odette, Scripta metallurgica, 17 (1983) 1183-1188.

[123] P. Othen, M. Jenkins, G. Smith, Philos.l Mag A, 70 (1994) 1-24.

[124] P. Othen, M. Jenkins, G. Smith, W. Phythian, Philos. Mag. Lett., 64 (1991) 383-391.

[125] Y.-U. Heo, Y.-K. Kim, J.-S. Kim, J.-K. Kim, Acta Mater., 61 (2013) 519-528.

[126] O. Anderoglu, T.S. Byun, M. Toloczko, S.A. Maloy, Metall. Mater. Trans. A, 44 (2013) 70-83.

[127] J. Vitek, W. Corwin, R. Klueh, J. Hawthorne, J. Nucl. Mater., 141 (1986) 948-953.

[128] M. Makin, J. Sharp, physica status solidi (b), 9 (1965) 109-118.

[129] B. Singh, A. Foreman, H. Trinkaus, J. Nucl. Mater., 249 (1997) 103-115.

[130] Z. Jiao, G. Was, Acta Mater., 59 (2011) 4467-4481.

[131] G.S. Was, J.P. Wharry, B. Frisbie, B.D. Wirth, D. Morgan, J.D. Tucker, T.R. Allen, J. Nucl. Mater., 411 (2011) 41-50.

[132] T. Anthony, J. Corbett, L. Ianniello, National Technical Information Service, CONF-710601, 1972.

[133] P. Okamoto, S. Harkness, J. Laidler, Argonne National Lab., IL, 1973.

[134] P. Okamoto, H. Wiedersich, J. Nucl. Mater., 53 (1974) 336-345.

[135] A. Marwick, Journal of Physics F: Metal Physics, 8 (1978) 1849.

[136] T.R. Allen, G. Was, Acta Mater., 46 (1998) 3679-3691.

[137] Z. Lu, R. Faulkner, G. Was, B. Wirth, Scripta Mater., 58 (2008) 878-881.

[138] J.P. Wharry, G.S. Was, Acta Mater., 65 (2014) 42-55.

[139] G. Odette, M. Alinger, B. Wirth, Annu. Rev. Mater. Res., 38 (2008) 471-503.

[140] M.J. Demkowicz, P. Bellon, B. Wirth, MRS bulletin, 35 (2010) 992-998.

[141] X. Zhang, E. Fu, L. Nan, A. Misra, Y. Wang, L. Shao, H. Wang, J.Eng.Mater.Technol., 134 (2012) 041010.

[142] A. Misra, M. Demkowicz, X. Zhang, R. Hoagland, Jom, 59 (2007) 62-65.

[143] M. Demkowicz, R. Hoagland, J. Hirth, Phys. Rev. Lett., 100 (2008) 136102.

[144] X. Zhang, N. Li, O. Anderoglu, H. Wang, J.G. Swadener, T. Höchbauer, A. Misra, R.G. Hoagland, Nucl. Instrum. Methods Phys. Res., Sect. B, 261 (2007) 1129-1132.

[145] T. Höchbauer, A. Misra, K. Hattar, R. Hoagland, J. Appl. Phys., 98 (2005) 123516.

[146] N. Li, J. Carter, A. Misra, L. Shao, H. Wang, X. Zhang, Philos. Mag. Lett., 91 (2011) 18-28.

[147] E.G. Fu, J. Carter, G. Swadener, A. Misra, L. Shao, H. Wang, X. Zhang, J. Nucl. Mater., 385 (2009) 629-632.

[148] E. Fu, A. Misra, H. Wang, L. Shao, X. Zhang, J. Nucl. Mater., 407 (2010) 178-188.

[149] N. Li, E.G. Fu, H. Wang, J.J. Carter, L. Shao, S.A. Maloy, A. Misra, X. Zhang, J. Nucl. Mater., 389 (2009) 233-238.

[150] Q. Wei, N. Li, N. Mara, M. Nastasi, A. Misra, Acta Mater., 59 (2011) 6331-6340.

[151] K. Yu, C. Sun, Y. Chen, Y. Liu, H. Wang, M. Kirk, M. Li, X. Zhang, Philos. Mag., 93 (2013) 3547-3562.

[152] K. Yu, Y. Liu, E. Fu, Y. Wang, M. Myers, H. Wang, L. Shao, X. Zhang, J. Nucl. Mater., 440 (2013) 310-318.

[153] C. Sun, M. Song, K. Yu, Y. Chen, M. Kirk, M. Li, H. Wang, X. Zhang, Metall. Mater. Trans. A, 44 (2013) 1-9.

[154] W. Han, M. Demkowicz, E. Fu, Y. Wang, A. Misra, Acta Mater., 60 (2012) 6341-6351.

[155] S.J. Zinkle, K. Farrell, J. Nucl. Mater., 168 (1989) 262-267.

[156] M. Dollar, H. Gleiter, Scripta Metall, 19 (1985) 481-484.

[157] M.A. Tschopp, K. Solanki, F. Gao, X. Sun, M.A. Khaleel, M. Horstemeyer, Phys. Rev. B, 85 (2012) 064108.

[158] M. Samaras, P. Derlet, H. Van Swygenhoven, M. Victoria, Phys. Rev. Lett., 88 (2002) 125505.

[159] X. Bai, A.F. Voter, R.G. Hoagland, M. Nastasi, B.P. Uberuaga, Science, 327 (2010) 1631-1634.

[160] D. Chen, J. Wang, T. Chen, L. Shao, Sci.Rep., 3 (2013).

[161] S. Wurster, R. Pippan, Scripta Mater., 60 (2009) 1083-1087.

[162] Y. Chimi, A. Iwase, N. Ishikawa, M. Kobiyama, T. Inami, S. Okuda, J. Nucl. Mater., 297 (2001) 355-357.

[163] M. Rose, A. Balogh, H. Hahn, Nucl. Instrum. Methods Phys. Res., Sect. B, 127 (1997) 119-122.

[164] K. Yu, Y. Liu, C. Sun, H. Wang, L. Shao, E. Fu, X. Zhang, J. Nucl. Mater., 425 (2011) 140-146.

[165] H. Wang, R. Araujo, J. Swadener, Y. Wang, X. Zhang, E. Fu, T. Cagin, Nucl. Instrum. Methods Phys. Res., Sect. B, 261 (2007) 1162-1166.

[166] T.D. Shen, S. Feng, M. Tang, J.A. Valdez, Y. Wang, K.E. Sickafus, Appl. Phys. Lett., 90 (2007) 263115-263113.

[167] A. Kilmametov, D. Gunderov, R. Valiev, A. Balogh, H. Hahn, Scripta Mater., 59 (2008) 1027-1030.

[168] A. Meldrum, L.A. Boatner, R.C. Ewing, Nucl. Instrum. Methods Phys. Res., Sect. B, 207 (2003) 28-35.

[169] T. Shen, Nucl. Instrum. Methods Phys. Res., Sect. B, 266 (2008) 921-925.

[170] D. Kaoumi, A. Motta, R. Birtcher, J. Appl. Phys., 104 (2008) 073525-073513.

[171] H.A. Atwater, C.V. Thompson, H.I. Smith, J. Appl. Phys., 64 (1988) 2337-2353.

[172] D.E. Alexander, G.S. Was, Phys. Rev. B, 47 (1993) 2983.

[173] T. Chen, J. Yang, Mater. Sci. Eng. A, 311 (2001) 28-41.

[174] R.E. Stoller, M. Toloczko, G. Was, A. Certain, S. Dwaraknath, F. Garner, Nucl. Instrum. Methods Phys. Res., Sect. B, 310 (2013) 75-80.

[175] Q. Gao, Y. Liu, X. Di, L. Yu, Z. Yan, J Mater Res., 27 (2012) 2779.

[176] M. Jenkins, J. Nucl. Mater., 216 (1994) 124-156.

[177] E. Wilson, Metal science, 18 (1984) 471-484.

[178] L. Fielding, Mater Sci. Technol., 29 (2013) 383-399.

[179] P. Yan, H. Bhadeshia, Metall. Mater. Trans. A, 44 (2013) 5468-5477.

[180] K. Jack, Iron and Steel Institute, 169 (1951) 26.

[181] S. Spigarelli, E. Cerri, P. Bianchi, E. Evangelista, Mater.Sci. technol., 15 (1999) 1433-1440.

[182] V.T. Paul, S. Saroja, P. Hariharan, A. Rajadurai, M. Vijayalakshmi, J. Mater. Sci., 42 (2007) 5700-5713.

[183] Y. Wang, E. Ma, Acta Mater., 52 (2004) 1699-1709.

[184] G. Sevillano, Prog. Mater Sci., 25 (1980) 69-412.

[185] M.A. e Meyers, K.K. Chawla, Mechanical behavior of materials, Cambridge University Press, The Edinburg Building, Cambridge CB2 8RU, UK, 2009.

[186] J. Sanchez-Hanton, R. Thomson, Mater. Sci. Eng. A, 460 (2007) 261-267.

[187] H. Sakasegawa, T. Hirose, A. Kohyama, Y. Katoh, T. Harada, K. Asakura, T. Kumagai, J. Nucl. Mater., 307 (2002) 490-494.

[188] B.Q. Han, F.A. Mohamed, E.J. Lavernia, Metall. Mater. Trans. A, 34 (2003) 71-83.

[189] H.K.D.H. Bhadeshia, R.W.K. Honeycombe, Steels: microstructure and properties, Butterworth-Heinemann, Linacre House, Jordan Hill, Oxford OX2 8DP, UK, 2006.

[190] T. Gladman, Mater.Sci.Technol., 15 (1999) 30-36.

[191] A. Foreman, M. Makin, Philos. Mag., 14 (1966) 911-924.

[192] A. Ardell, Metall. Mater. Trans. A, 16 (1985) 2131-2165.

[193] N. Hansen, Scripta Mater., 51 (2004) 801-806.

[194] D.A. Hughes, N. Hansen, Acta Mater., 48 (2000) 2985-3004.

[195] N. Kamikawa, X. Huang, N. Tsuji, N. Hansen, Acta Mater., 57 (2009) 4198-4208.

[196] J. Rosenberg, H. Piehler, Metall. Mater. Trans. B, 2 (1971) 257-259.

[197] L. Kubin, B. Devincre, T. Hoc, Acta Mater., 56 (2008) 6040-6049.

[198] S. Cheng, E. Ma, Y. Wang, L. Kecskes, K. Youssef, C. Koch, U. Trociewitz, K. Han, Acta Mater., 53 (2005) 1521-1533.

[199] N. Hansen, Mater. Sci. Eng. A, 409 (2005) 39-45.

[200] Z. Shan, R.K. Mishra, S.A.S. Asif, O.L. Warren, A.M. Minor, Nat.Mater., 7 (2007) 115-119.

[201] J.R. Greer, W.C. Oliver, W.D. Nix, Acta Mater., 53 (2005) 1821-1830.

[202] M. Lowry, D. Kiener, M. LeBlanc, C. Chisholm, J. Florando, J. Morris, A. Minor, Acta Mater., 58 (2010) 5160-5167.

[203] X. Huang, N. Hansen, N. Tsuji, Science, 312 (2006) 249-251.

[204] G. Fan, H. Choo, P. Liaw, E. Lavernia, Acta Mater., 54 (2006) 1759-1766.

[205] Z. Dapeng, L. Yong, L. Feng, W. Yuren, Z. Liujie, D. Yuhai, Mater. Lett., (2011).

[206] M.K. Miller, K.F. Russell, D.T. Hoelzer, J. Nucl. Mater., 351 (2006) 261-268.

[207] M.K. Miller, D.T. Hoelzer, E.A. Kenik, K.F. Russell, Intermetallics, 13 (2005) 387-392.

[208] B. Inkson, P. Threadgill, High temperature ordered intermetallic alloys VII, (1997) 767-772.

[209] M. Klimiankou, R. Lindau, A. Möslang, J. Nucl. Mater., 367-370 (2007) 173-178.

[210] E. Hall, Proc.Phys. Soc. Ser. B, 64 (1951) 747.

[211] R.O. Scattergood, D.J. Bacon, Philos. Mag., 31 (1975) 179-198.

[212] S. Ukai S. Mizuta, M. Fujiwara, T. Okuda, T. Kobayashik, J. Nucl.Sci. Technol., 39 (2002) 778-788.

[213] D.C. Foley, K.T. Hartwig, S.A. Maloy, P. Hosemann, X. Zhang, J. Nucl. Mater., 389 (2009) 221-224.

[214] M. Murayama, Z. Horita, K. Hono, Acta Mater., 49 (2001) 21-29.

[215] P. Gay, P. Hirsch, A. Kelly, Acta Metall., 1 (1953) 315-319.

[216] G. Williamson, R. Smallman, Philos. Mag., 1 (1956) 34-46.

[217] M. Song, R. Zhu, D. Foley, C. Sun, Y. Chen, K. Hartwig, X. Zhang, J. Mater. Sci., 48 (2013) 7360-7373.

[218] B. Singh, M. Eldrup, S. Zinkle, S. Golubov, Philos. Mag. A, 82 (2002) 1137-1158.

[219] C. Sun, D. Bufford, Y. Chen, M. Kirk, Y. Wang, M. Li, H. Wang, S. Maloy, X. Zhang, Sci. Rep., 4 (2014).

[220] M. Ghaly, K. Nordlund, R. Averback, Philos.Mag. A, 79 (1999) 795-820.

[221] D. Plumton, W. Wolfer, J. Nucl. Mater., 120 (1984) 245-253.

[222] D. Plumton, G. Kulcinski, J. Nucl. Mater., 133 (1985) 444-447.

[223] W. Johnston, J. Rosolowski, A. Turkalo, T. Lauritzen, J. Nucl. Mater., 62 (1976) 167-180.

[224] C. Wei, A. Aitkaliyeva, M. Martin, D. Chen, L. Shao, Nucl. Instrum. Methods Phys. Res., Sect. B, 307 (2013) 181-184.

[225] D. Gelles, J. Nucl. Mater., 233 (1996) 293-298.

[226] J. Vitek, R. Klueh, J. Nucl. Mater., 122 (1984) 254-259.

[227] J. Kai, R. Klueh, J. Nucl. Mater., 230 (1996) 116-123.

[228] R.E. Stoller, J. Nucl. Mater., 174 (1990) 289-310.

[229] P. Maziasz, R. Klueh, J. Vitek, J. Nucl. Mater., 141 (1986) 929-937.

[230] X. Jia, Y. Dai, J. Nucl. Mater., 318 (2003) 207-214.

[231] C. Fu, F. Willaime, P. Ordejón, Phys. Rev. Lett., 92 (2004) 175503.

[232] M.A. Kirk, P.M. Baldo, A.C. Liu, E.A. Ryan, R.C. Birtcher, Z. Yao, S. Xu, M.L. Jenkins, M. Hernandez-Mayoral, D. Kaoumi, Microsc. Res. Tech., 72 (2009) 182-186.